Dynamic Behavior of Healthy and Malaria Infected Human Red Blood Cells

by

David John Quinn

B.S. Mechanical Engineering, Villanova University (2002)
M.Phil. Engineering by Research, University of Cambridge (2003)
S.M. Mechanical Engineering, Massachusetts Institute of Technology (2006)

Submitted to the Department of Mechanical Engineering
in partial fulfillment of the requirements for the degree of

Doctor of Science in Mechanical Engineering

at the

MASSACHUSETTS INSTITUTE OF TECHNOLOGY

June 2010

Author ....
Department of Mechanical Engineering
May 18, 2010

Certified by ....
Subra Suresh
Vannevar Bush Professor of Engineering
Professor of Mechanical Engineering
Chairman of the Committee
Thesis Supervisor

Accepted by ....
David E. Hardt
Chairman, Department Committee on Graduate Theses

Dynamic Behavior of Healthy and Malaria Infected Human Red Blood Cells

by

David John Quinn

Submitted to the Department of Mechanical Engineering
on May 18, 2010, in partial fulfillment of the
requirements for the degree of
Doctor of Science in Mechanical Engineering

Abstract

Hereditary hematological disorders and foreign organisms often introduce changes to the spectrin molecular network and membrane of human red blood cells (RBCs). These structural changes lead to altered cell shape, deformability, cytoadherence and rheology which may in turn, promote the onset of vaso-occlusive events and crises that may ultimately cause pain, stroke, organ damage and possibly death. Previous work by our group and others has shown that the RBC membrane exhibits reduced deformability as a manifestation of diseases such as malaria, spherocytosis, elliptocytosis and sickle cell anemia. However, much of this previous work has modeled the RBC membrane as a purely elastic material and experiments are typically performed within the quasistatic deformation regime. This work investigates the connection between disease, structure and function in a more physiologically relevant, dynamic context using two *in-vitro* experimental approaches: (1) dynamic force-displacement characterizations using advanced optical trapping techniques and (2) microfluidic flow experiments. A new set of dynamic optical trapping experiments are developed using an alternate loading configuration and a broader range of deformation rates (up to $100\mu m/s$) and forcing frequencies (up to 100Hz) than previously reported with optical trapping systems. Results from these experiments provide further support to recent suggestions that traditional constitutive descriptions of the viscoelastic behavior of the RBC membrane are not applicable to this wide range of deformation rates and frequencies. Initial results on RBCs infected with *Plasmodium falciparum* malaria suggest that the parasite and its related exported proteins act to increase the effective viscosity of the RBC membrane. The role of the temperature-dependent, viscous behavior of the RBC membrane is further explored in microfluidic flow experiments, where the flow behavior of RBCs is quantified in fluidic structures with length scales approaching the smallest relevant dimensions of the microvasculature (approximately $3\mu m$ in characteristic diameter). In particular, the role of a parasitic protein, the ring infected erythrocyte surface antigen (RESA), is investigated and determined to have a rate-dependent effect on microvascular flow behavior that has not previously been identified. Results from optical trapping and microfluidic flow experiments are used to inform and validate a collaborative effort aimed at developing a meso-scale, three-dimensional model of microvascular flow using dissipative particle dynamics (DPD). This combination of modeling and experiments give new insight into the relative roles of fluid and membrane viscosity in microvascular flow. The results of this work may be used in the development of new constitutive behaviors to describe the deformation of the RBC membrane and to inform the design and optimization of microfluidic tools for blood separation and point-of-care diagnostic platforms. In addition, using the techniques developed here in further investigation of the roles of particular parasitic proteins may yield additional insight into the pathology of *P.f.* malaria that may, in turn, provide new avenues and approaches for treatment.

Thesis Supervisor: Subra Suresh
Title: Vannevar Bush Professor of Engineering
Professor of Mechanical Engineering
Chairman of the Committee

Acknowledgments

I am grateful to too many people to try to name them all individually. However, professionally, I would like to thank my supervisor, Prof. Subra Suresh, for allowing me the opportunity to work in his lab and providing me with all of the financial and personal support necessary to perform this work. Similarly, I would like to acknowledge the NSF and NDSEG graduate research fellowships for their support throughout my graduate studies.

Personally, the list of people to whom I am indebted could go on for several chapters. So, rather than risk forgetting to include anyone, I will acknowledge the most significant one: my wife Molly. I cannot imagine my life without her and do not think this body of work would have ever been completed without her love and support. I am more proud of my relationship with her than anything I have ever done.

Contents

List of Figures

List of Tables

Chapter 1

Introduction

The flow of red blood cells (RBC) through the microvasculature is critical to human health. During its typical life-span of 120 days upon egress from the bone marrow, the human RBC circulates through the body approximately 500,000 times, delivering oxygen to tissue and vital organs. As it repeatedly traverses capillaries and microvascular passages, the RBC undergoes severe deformation with strains in excess of 100% [14, 21, 70]. Such deformation levels are typical, for example, in the spleen, where the RBC squeezes through splenic sinus and inter-endothelial slits with diameters estimated to be approximately 3 μm [18, 42]. Large deformation can also occur in capillaries and artioles, where RBCs do not travel in isolation and their interactions with one another and the vascular wall cause them to stretch by up to 150%. As a result, the role of deformability in influencing RBC function has been studied extensively [14, 21, 70]. Furthermore, compromised RBC deformability contributing to human disease pathologies has also been a topic of growing research interest. For example, hereditary blood disorders such as spherocytosis, ellipocytosis and ovalocytosis, as well as diseases such as diabetes, sickle cell anemia, and malaria all exhibit characteristic losses in RBC deformability with the onset and progression of the pathological state. For the case of *Plasmodium falciparum (P.f.)* malaria, recent experiments showed that the membrane stiffness of the parasitized RBC can increase more than 20-fold during intra-erythrocytic parasite maturation [102, 67]. Such changes act in concert with enhanced cytoadherence to other RBCs and the vascular endothelium to facilitate vaso-occlusive events such as stroke or other ischemias. In addition to its impact on disease pathologies, the deformability of the RBC is also of interest for the development of advanced *in-vitro* tools for the purposes of drug efficacy studies and the development of diagnostic platforms. Furthermore, RBC deformability and its impact on blood-flow and the development of vaso-occlusions is of direct importance in the performance more traditional implantable devices, such as heart valves and stents [95].

Despite such broad and growing interest in RBC deformability, much of the quantitative understanding of single-cell deformability characteristics has been limited to quasi-static experiments, where only a limited range of deformation rates are examined. While such single-cell, quasi-static assays have helped establish connections between the biophysical characteristics of RBC and disease states [102], they do not adequately capture the reality of various biorheological events associated with the flow of a population of RBCs through the microvasculature. Where more physiologically relevant, dynamic or flow characteristics of RBCs have been presented, they are often times limited in their quantitative nature and/or do not consider physiologically relevant temperature conditions. Furthermore, very little quantitative information exists on the dynamic and flow behaviors of diseased RBCs, such as those parasitized with *P.f.* malaria at relevant length scales and temperature.

In this thesis work, two experimental approaches were used in order to satisfy the need for additional quantitative insight into the dynamic behavior of healthy and diseased RBCs. First, an advanced optical tweezers system was implemented to examine the dynamic response of human RBCs over the broadest range of time-scales, frequencies and largest deformations reported to date with optical trapping techniques. In addition, this trapping system was used by collaborators to study the mechanical response of the human RBC as a function of temperature and disease progression in *P.f.* malaria. The effect of a specific parasitic protein (ring-infected erythrocyte surface antigen, RESA) on the mechanical behavior of the RBC membrane was also examined. Second, a microfluidic system was employed in order to quantify the flow dynamics of healthy and diseased RBCs at the smallest relevant length scales, as well as physiological temperatures.

An important aspect of these optical trapping and microfluidic characterizations is their ability to be utilized in the development and validation of advanced computational models of microvascular flow. Therefore, where applicable, the results of a collaborative effort in computational modeling using dissipative particle dynamics (DPD) are presented in conjunction with experimental results in order to highlight the utility of such a combined experimental and modeling approach. This framework may be accessed to develop robust models that can be used for *in vivo* predictions. The insight gained from a systematic combination of simulations and experiments could also be used in the design and optimization of novel microfluidic systems for disease diagnostics and drug efficacy assays and in the interpretation of the role of mechanical and rheological cell properties in disease pathologies. Such insight may, in turn, lead to new therapeutic approaches for treatment.

Chapter 2

Background

2.1 Red Blood Cell Deformability

Red blood cells (RBCs) comprise 40-50% of human blood volume and are the primary vehicle for oxygen delivery to the tissue and vital organs of the body [11]. A mature RBC does not contain a nucleus and is comprised of a membrane structure and an internal fluid environment. The RBC membrane is comprised of a lipid bilayer and an underlying spectrin network. This general structure is depicted in Figure 2-1. The phospholipid bilayer contains cholesterol molecules with polar, hydrophilic head groups and a hydrophobic core, as shown in Figure 2-2, as well as integral/transmembrane proteins that form the attachment sites for the spectrin network. The detailed structure of the spectrin network is shown in Figure 2-3. The primary subunit of the spectrin network is a spectrin tetramer, which is composed of two head-to-head aligned heterodimers, themselves made up of intertwined alpha and beta spectrins. The end of each spctrin tetramer is linked to a junction complex of f-actin and band 4.1 proteins, which is in turn anchored to the bilayer via glocophorin. In addition, band 3 and ankyrin also form a complex that is anchored to the bilayer at intermediate points along the spectrin tetramer. Topologically, the spectrin network is a triangulated network, as shown in Figures 2-3 and 2-4 [2, 61].

The typical, at-rest, shape of the RBC is that of a biconcave disc with an average major diameter of approximately 7-8 μm and thickness of approximately 2.5 μm [43].

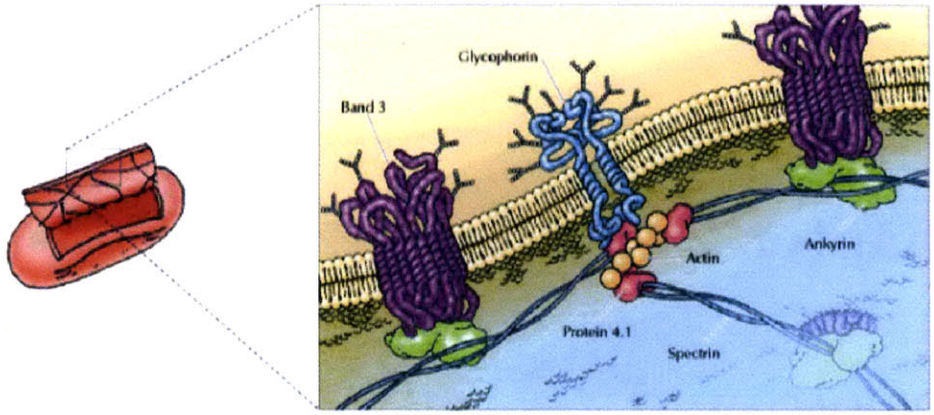

Figure 2-1: General structure of the Red Blood Cell (RBC). (Taken from Alberts et al. [2])

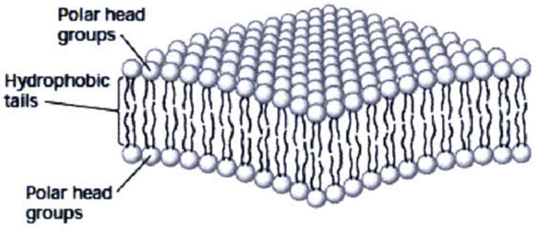

Figure 2-2: Structure of a phospholipid bilayer. (Taken from Lodish et al. [61])

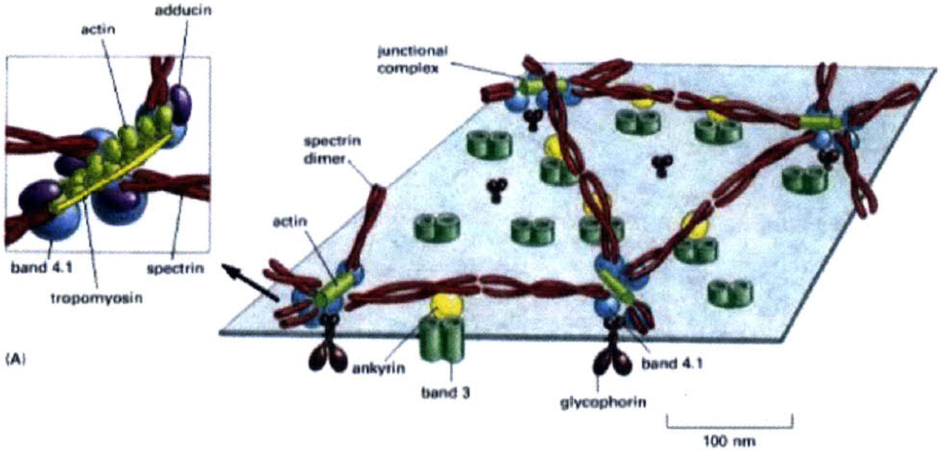

Figure 2-3: Graphical depiction of the structure of the RBC spectrin network. (Taken from Alberts et. al. [2])

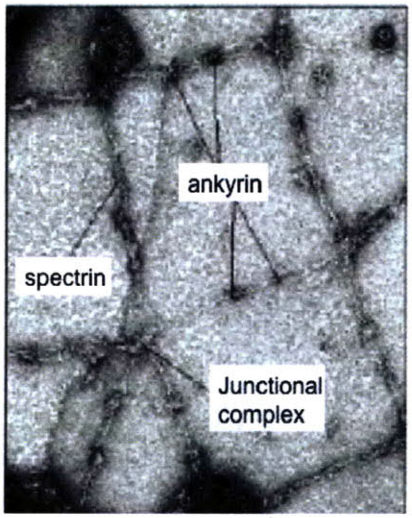

Figure 2-4: Electron micrograph of the RBC spectrin network. (Taken from Alberts et. al. [2])

This characteristic shape is shown in Figure 2-5. As discussed in Chapter 1, as part of its normal physiological function, this shape is required to deform severely as it undergoes nearly 500,000 cycles of deformation through its 120-day lifetime, often times being required to pass pores or slits with characteristic lengths and diameters down to $2-3\mu m$. Several examples of such deformation levels are shown in Figure 2-6.

With such severe mechanical deformations required for the human RBC to perform its primary function, it is no surprise that reduced RBC deformability plays a role in the pathology of several diseases and disorders. These include hereditary disorders such as spherocytosis, elliptocytosis, ovalocytosis and sickle cell anemia, where genetic mutations cause deficiencies in either the spectrin network or the hemoglobin that lead to reduced deformability. Alteration of RBC membrane properties is also a part of the pathology of infectious diseases such as malaria, where structural modifications made by parasitic proteins lead to significantly reduced deformability and increased cytoadherence. The role of RBC deformability in blood flow and its manifestation in haemotological disorders is well-reviewed by several authors, including Mohandas [69], Chien [21], Hochmuth and Waugh [51], and Mohandas and Evans [70]. Generally speaking, it is widely accepted that in many diseases and disorders,

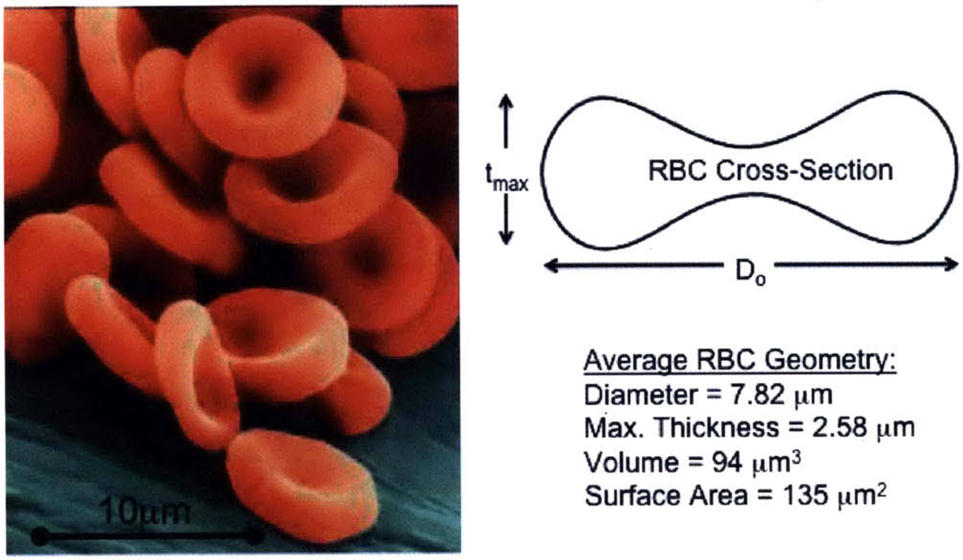

(a) (b)

Figure 2-5: (a) Colorized electron micrograph illustrating the typical biconcave shape of human RBC. (Taken from Lodish et. al.[61]), (b) Average geometric cross-section and corresponding surface area and volume (Adapted from Fung [43])

reduced deformability acts in concert with other factors, such as cytoadherence, to facilitate the occurrence of vaso-occlusive events that may lead to ischemia and/or, in the extreme case, stroke and death.

2.1.1 RBC membrane elasticity

The elastic properties of the RBC have most frequently been characterized using micropipette aspiration, whereby a portion of the RBC membrane is drawn into a glass micropipette using suction pressure [88, 37, 51, 21, 109]. Measuring the geometry changes of the cell into the pipette, such as the projected length of the membrane in the glass tube combined with predictions from numerical and analytical models, allows one to determine the mechanical properties of the membrane, such as the membrane shear modulus (μ_o) and the area expansion modulus (K). In addition, other techniques, such as buckling instability measurements and thermal fluctuation measurements, allow for an estimate of the bending modulus of the membrane (B_o) [38, 40]. The typical range of elastic properties of the RBC membrane are summarized

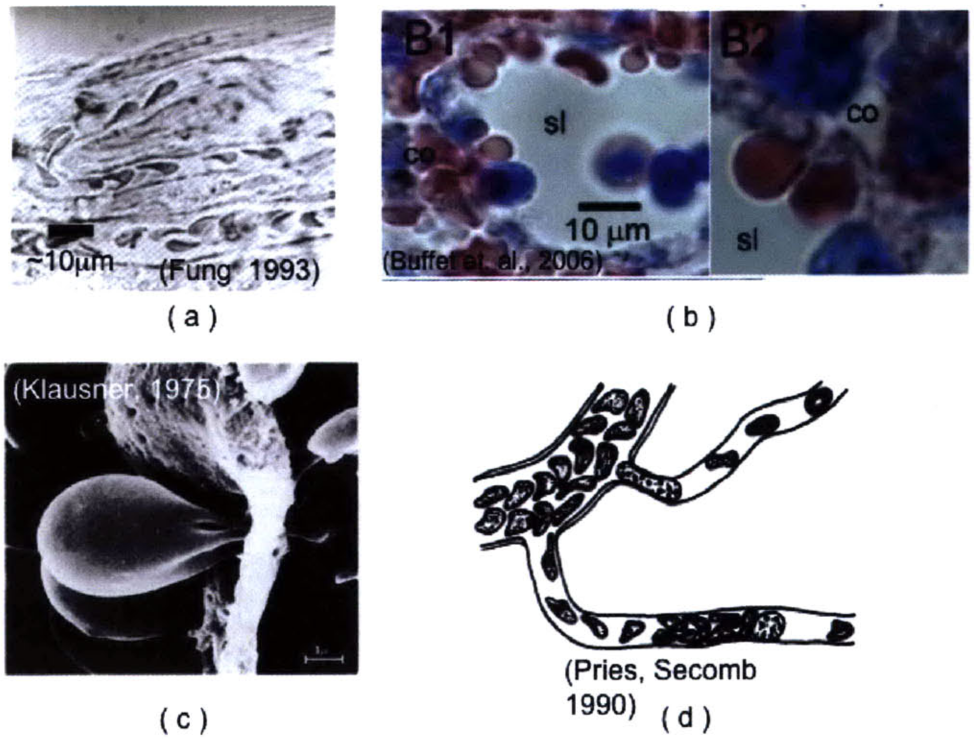

(a) (b) (c) (d)

Figure 2-6: Examples of large deformations of RBCs in the microvasculature: (a) Bright field, phase image of RBC flow in the canine microvasculature. (Taken from Fung. [43]), (b) Histological stain of ex-vivo spleen perfusion experiment showing the passage of red cells (stained red) across the splenic sinus wall from the cords (co) to the sinus lumen (sl). (Taken from Buffet et. al [18]), (c) SEM image of mouse RBC passage across circular pores in the spleen (Taken from Klausner [56]), (d) graphical depiction of RBC flow in the microvasculature in the presence of white cells. (Taken from Pries and Secomb, [85]) in Table 2.1. It has been shown that these values do not vary significantly between room and physiological temperatures (22-41°C) [109].

Area Expansion Modulus (K)	$300 - 500mN/m$ [37, 51, 21, 109]
Membrane Shear Modulus (μ_o)	$4 - 10\mu N/m$ [37, 51, 21, 109]
Bending Modulus (B_o)	$(1.7 - 9) \cdot 10^{-9}Nm$ [38, 40]

Table 2.1: Elastic properties of the healthy human RBC

At the molecular level, the lipid bilayer is responsible for the strong resistance to area changes in the RBC membrane. The bilayer is also responsible for the relatively small amount of bending resistance. However, the bilayer is not capable of resisting shear deformations. Thus, the underlying, two-dimensional spectrin network is responsible for the shear resistance of the RBC membrane. It is this shear resistance that is considered to be the major property of interest when considering the overall RBC deformability [37].

Other techniques have been employed to measure the quasistatic, elastic properties of the RBC membrane. These include laminar shear flow experiments [104], spectroscopic techniques measuring thermal fluctuations [75] and, most notably for this work, optical tweezers [47, 101, 30, 29, 28]. The first experiments utilizing an optically trapped bead to impart tensile forces to an RBC and attempt to extract mechanical properties were reported by Henon et al. [47]. This work reported an RBC membrane shear modulus of $2.5 \pm 0.4\mu N/m$, which is significantly lower than the typically measured range of $4 - 10\mu N/m$. This discrepancy may be attributed to the fact that, in their analysis of the measured force-displacement response of the cell, Henon et al only considered a linear-elastic, small deformation constitutive model of the RBC membrane and did not consider the effects of contact area between the bead and cell. A subsequent study by Sleep et. al. [101] over-estimated the membrane shear modulus by at least one order of magnitude compared to the typically accepted values. This is also likely due to incorrect assumptions about the RBC shape as either a planar disc or a sphere and failure to account for the large contact area between the trapped beads and cells. More recently, Mills et. al. and Dao et. al. combined optical tweezers with a finite element study to determine the elastic properties of the RBC membrane [30, 29, 28]. This combined experimental and modeling approach accurately accounted for the RBC shape and contact areas during an experiment. As a result, their results were in much better agreement with other traditionally-accepted techniques such as micropipette aspiration.

2.1.2 RBC membrane viscosity

Much of the current understanding of the RBC membrane viscosity is built upon the work of Evans and Hochmuth [39, 49], who described the stress in an RBC membrane undergoing finite deformations as the superposition of elastic and dissipative or viscous components:

$$T_{ij} = T_{ij}^e + T_{ij}^v \tag{2.1}$$

Where the elastic component of stress

$$T_{ij}^e = K\alpha\delta_{ij} + \mu\epsilon_{ij} \tag{2.2}$$

Where K is the area expansion modulus, $\alpha = \lambda_1\lambda_2 - 1$ is the area expansion, and μ is the shear modulus. The viscous stresses are expressed as a constant (η_e, the membrane viscosity) times the rate of deformation (V_{ij}):

$$T_{ij}^v = 2\eta_e V_{ij} \tag{2.3}$$

For the case of an incompressible material ($\lambda_1\lambda_2 = 1$) in uniaxial tension,

$$T_{11} = (\mu/2)(\lambda_1^2 - \lambda_1^{-2}) + 4\eta_e(d\lambda_1/dt)(1/\lambda_1) \tag{2.4}$$

Under conditions when external forces such as fluid shear are small compared to the internal membrane forces, the elastic stresses must balance the viscous stresses:

$$T_{ij}^e + T_{ij}^v = 0 \tag{2.5}$$

Under uniaxial tension, Equation 2.5 reduces to:

$$(\mu/2)(\lambda_1^2 - \lambda_1^{-2}) + 4\eta_e(d\lambda_1/dt)(1/\lambda_1) = 0 \tag{2.6}$$

For a given set of initial stretch values (λ_{1o}), Equation 2.6 has the solution:

$$((\lambda_1^2 - 1)/(\lambda_1^2 + 1)) = ((\lambda_{1o}^2 - 1)/(\lambda_{1o}^2 + 1))e^{-t/t_c} \tag{2.7}$$

Where $t_c = 2\eta_e/\mu$ is the characteristic time constant for the membrane material. This relationship has been applied to experiments measuring the relaxation characteristics of RBCs upon release from micropipette aspiration to determine $t_c = 0.3s$. With the range of shear modulus in Table 2.1, the membrane viscosity is in the range: $\eta_e = 0.6 - 1.5\mu Ns/m$ [39]. Further experiments measuring the relaxation time of an RBC deformed at diametrically opposite ends using a dual micropipette aspiration configuration estimated the characteristic time to be approximately 0.2-0.26s [49]. Similar relaxation measurements made by Mills et. al [68] using optical tweezers yielded similar results as the dual micropipette configuration used by Hochmuth et. al. [49].

Subsequent to the work done by Hochmuth and Evans, Engelhardt et. al. measured the time-dependent extension and relaxation characteristics of the RBC under forces resulting from a high-frequency electric field [35, 36]. This work suggested two time-scales present in the response of the RBC: a short time scale ($t_{c1} = 0.1s$) and a long time-scale ($t_{c2} = 1.0s$) governing the initial and long-term response of the RBC, respectively. More recently, Puig-De-Morales-Marinkivic et. al have examined the viscoelastic response of the RBC membrane using magnetic twisting cytometry (MTC) [86]. This work suggests that the single or two time-scale descriptions of the RBC membrane viscosity are not sufficient to describe the RBC membrane behavior. Instead, considering the RBC membrane as a viscoelastic material with a complex modulus ($G^* = G' + iG''$), this work found a strong dependence of the loss modulus (G") of the membrane with frequencies from 0.1-100Hz. This dependence is best described by a power-law where $G'' \sim f^\alpha$ and $\alpha = 0.64$. However, this work was done under very low levels of applied force/deformation, with applied strain energies on the order of $0.1\mu J/m^2$, compared to $1 - 10\mu J/m^2$ in the work of Mills and in this thesis work [30, 29, 28]. The implications of larger deformation levels on the apparent rate and/or frequency-dependent response of the RBC membrane, as well as the appropriate scaling to describe the dissipative nature of the RBC membrane are subjects of this thesis work.

2.1.3 RBC flow in the microvasculature

There is a large body of classical work that has characterized the effective viscosity of whole blood as a function of vessel diameter and hematocrit. This work is well-reviewed in the texts by Fung [43, 44]. Generally speaking, in vessels on the order of 100 μm in diameter or larger, such as major arteries, blood can be described as a thixotropic fluid with a constant viscosity of $3.5cP$ (3-4 times that of water) under shear rates above $200s^{-1}$. However, as length scales approach the smallest regions of the microvasculature (less than $10\mu m$ diameters), an effective viscosity description is insufficient and contributions of the properties of individual cells must be considered. Such length scales and flow behaviors are a focus of this thesis work.

The biophysical factors affecting blood flow in the microcirculation are well-reviewed in the literature (e.g. Pries et. al. [84], Skalak et. al. [100], Schmid-Schonbein [90], Popel and Johnson [81]). Specifically, there exists a large body of work analyzing the flow of RBCs in vessels comparable to or smaller than the cell diameter. Much of this work builds upon the analysis presented by Lighthill of the flow of deformable pellets through narrow tubes [60]. Secomb et. al. [94] applied lubrication theory when considering the flow of an axisymmetric cell with shear and bending properties of the healthy RBC and determined, amongst other things, the equilibrium shapes of the RBC as a function of vessel diameter and flow velocity. Theses shapes are reproduced in Figure 2-7. Subsequently, Secomb and Hsu extended this analysis to consider the transit of red blood cells across pores comparable to the microvasculature [92]. In this analysis, the effects of membrane viscosity and external fluid viscosity were included and it was determined that the role of these

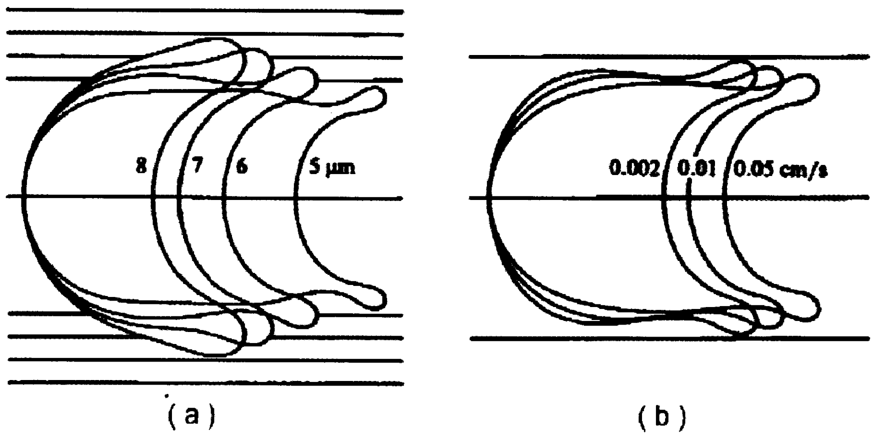

Figure 2-7: Steady-state shapes of axisymmetric cells flowing through cylindrical tubes. (a) Cell shapes in varying diameter tubes with a cell velocity of 0.01cm/s, (b) Cell shapes in a vessel diameter of $6\mu m$ subjected to varying flow velocities. (Taken from Secomb et. al. [94])

viscous components on flow inhibition (i.e. increased transit time) is more significant than membrane elasticity at diameters below $6\mu m$. However, like the previous work, this analysis had limited experimental validation and was restricted to the axisymmetric flow case. More recently, several groups have attempted much more advanced computations and simulations of RBC biorheology and microvascular flow [94, 92, 34, 27, 10, 74, 22, 82]. However, these computational approaches typically lack rigorous validation by either *in-vivo* or *in-vitro* experiments. This thesis work will present a framework allowing for experimental validation of modeling approaches attempting to describe the full three-dimensional flow behavior of the RBC.

In-vivo characterizations of microvascular flow in animal models have been presented by several groups (e.g. [85, 21, 33, 54]). Much of this work is well-reviewed by Fung [44]. These *in-vivo* experiments have provided important validation of the role of RBC deformability in microvascular flow. For example, RBCs stiffened by incubation with diamide or gluteraldehyde have shown decreased cell survival, increased splenic sequestration and increased filtration resistance in perfusion studies using canine and rat mesentary models [21, 33, 54]. In addition, perfusion studies of rat skeletal muscle have been coupled with insights from computational models to suggest that the RBC membrane viscosity has a significant role in increasing flow resistance in the microvasculature [91].

More recently, Jeong et. al. [53] were able to use a high speed imaging technique to measure microvascular flow in the microcirculation of anesthetized rats whose natural heartbeat is maintained through a life support system. Typical RBC velocities measured were approximately 2mm/s in vessels of approx. 6 μm diameter. This work provides some of the most quantitative measurements of individual cell velocities in the smallest regions of the microvasculature to date. However, in this work, like many others, significant uncertainties exist in the vessel geometry and there are no concurrent measurements of the pressure profile along the vessel of interest. Generally speaking, due to imaging and other experimental constraints (i.e. size constraints complicating the integration of local pressure probes), there have been few attempts at simultaneously characterizing flow velocities, pressure differentials and geometry *in-vivo*. Furthermore, there are no such studies at the length scales of interest in this thesis work (down to approx. $3\mu m$ diameter), such as those present in the spleen (see Figure 2-6).

In order to overcome this limitation, *in-vitro* assays of RBC flow through glass tubes [14, 50] and microfabricated fluidic structures made of glass, silicon or polydimethylsiloxane (PDMS) have been developed [3, 48, 97, 99, 107, 17]. These *in-vitro* experiments have suggested an increased role of the dynamic properties of the RBC under flow conditions. For example, Brody et. al. [17] have suggested that the time-scales of the RBC cytoskeleton's active reorganization is a significant factor of the ability of the RBC to traverse narrow pore-like structures. *In-vitro* flow studies have also established semi-quantitative links between decreased RBC deformability and inhibitied flow [99, 97]. However, there still remain a few short-comings of this body of work. Most notably, like *in-vivo* experiments, there is virtually no experimental quantification of flow characteristics (e.g., pressure difference versus cell velocity) of RBCs through constrictions of well-known geometry of the smallest relevant length scales (approx. 3 μm in diameter) whereby the dynamics of RBC deformation characteristic of the conditions in the microvasculature can be simulated and visualized. In a few isolated studies where RBC flow has been studied through such small channels [97, 99, 98], the dynamics of flow has not been quantified or analyzed so as to facilitate broad conclusions or to help facilitate the development of general computational models. Furthermore, when attempts to quantify such RBC dynamics have been made, they often do not take into account the effects of physiological temperature conditions [1, 41]. Providing such a fully quantitative study of RBC flow in the smallest length scales of the microvasculature at physiologically relevant temperatures is an important contribution of this thesis.

As a final note regarding microvascular flow, there exist a growing body of recent work examining the role of the microvascular glycocalyx, or endothelial surface layer (ESL) (e.g. [93, 83, 27], and the reviews of Kamm [55], Popel and Johnson [81], and Weinbaum et. al. [112]). This network of polysaccharides and glycoproteins on the surface of endothelial cells lining much of the microvasculature is approximately 0.5 μm thick and is an additional source of hydrodynamic resistance in microvascuature. As such, the glycocalyx is often hypothesized to be the source of discrepancies between *in-vitro* and *in-vivo* flow experiments. In addition, the glycocalyx is also thought be an integral part of the transduction pathway between fluid shear and the motility of the vascular endothelium [114]. The experimental results presented in this work do not explicitly account for the interaction of the RBC with the glycocalyx. However, where applicable, the extension of these results into future studies and simulations involving the glycocalyx will be discussed.

2.1.4 Deformability of *Plasmodium falciparum* malaria parasitized RBCs

P. falciparum malaria is the most severe of the four different plasmodium species capable of parasitizing human RBCs. The annual infection rate of *P.f. malaria* is on the order of several hundred million people and it is estimated to be responsible for several million deaths [65, 110]. The highest percentage of fatal cases of *P.f. malaria* occur in children, pregnant women and the elderly. A graphical description of the

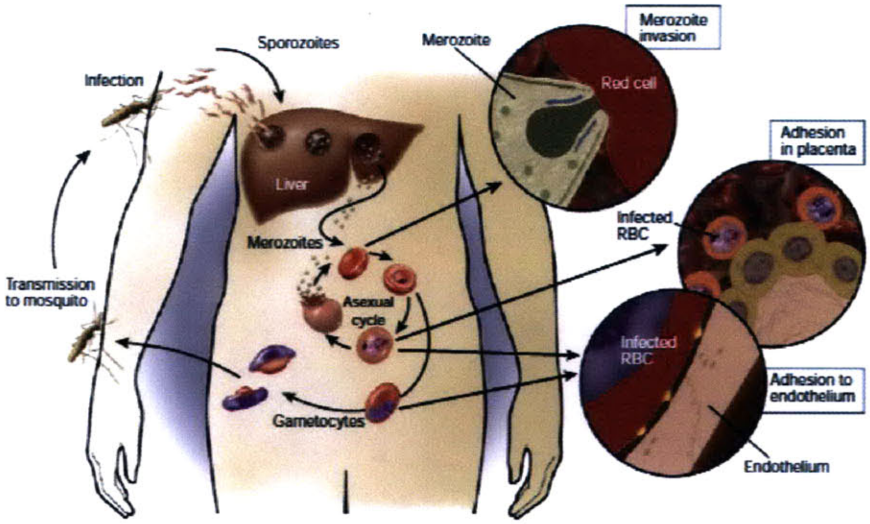

Figure 2-8: Life cycle and pathogenesis of *P.falciparum* malaria (Taken from Miller et. al. [65])

life cycle and pathogenesis of *P.f malaria* is shown in Figure 2-8. Upon transmission through a bite from the female anopheles mosquito, the malaria sporozoites travel to the liver. In the liver, each sporozoite, may develop into tens of thousands of merozoites. Upon release from the liver, merozoites invade red blood cells and begin the asexual life cycle of the parasite. This intra-erythrocytic life cycle is approximately 48 hrs and is broken down according to three characteristic stages (see Figure 2-9):

- Ring Stage (0-24hrs): The parasite resides as a thin discoid or ring-shaped feature with slightly enhanced size and pigment near the end of the stage. In this stage, the RBC generally retains its biconcave shape.

- Trophozoite Stage (24-36 hrs): The parasite growth accelerates and develops more pigmented regions. The parasite begins to grow rapidly and develop knobs or bulges at its surface.

- Schizont Stage (36-48 hrs): The parasite divides, producing up to 20 new merozoites. Knobs form on the surface of the RBC, which may serve as adhesion sites. The RBC also has a much more spherical shape.

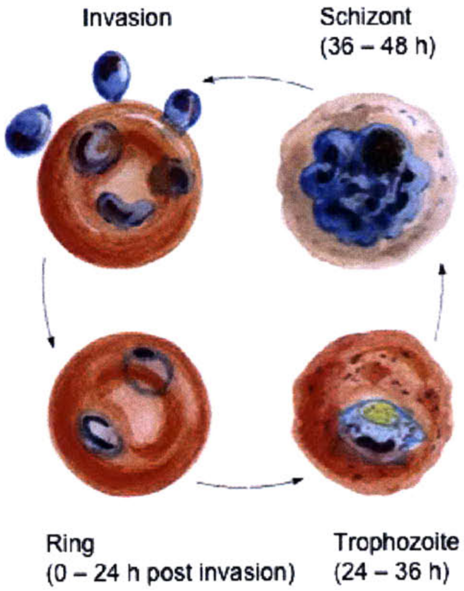

Figure 2-9: Intra-erythrocytic, asexual life-cycle of *P.falciparum* malaria (Taken from Alberts [2])

The body's natural immune response to malaria predominantly involves removal (aka "pitting") of the parasite, followed by phagocytosis by lymphocytes in the spleen. However, as the parasitemia increases, splenic clearance is insufficient. Throughout this entire life cycle, in addition to the severe structural evolution in the RBC, it has been shown that reduced deformability is a characteristic of the parasitized cell [24, 25, 45, 104]. In the trophozoite and schizont stages of parasite development, this decreased deformability is accompanied by increased cytoadhesion of the RBC membrane to other RBCs and vascular endothelium [65, 23]. Thus, it is likely that these factors act together to bring about red cell sequestration in the microvasculature and ischemia of major organs. Such sequestration and occlusive events contribute significantly to the occurrence of cerebral malaraia, hypoglycaemia, metabolic acidosis and respiratory distress [65]. This phenomenon of decreased deformabilty in parasitized RBCs was previously quantified using micropipette aspiration [45, 76] and laminar shear flow [26, 104]. Following that work, Suresh et. al. [102] used an optical trapping technique to demonstrate that the RBC membrane shear modulus may increase by more than a factor of 20 in the latest stages of the parasitic cycle. Those results

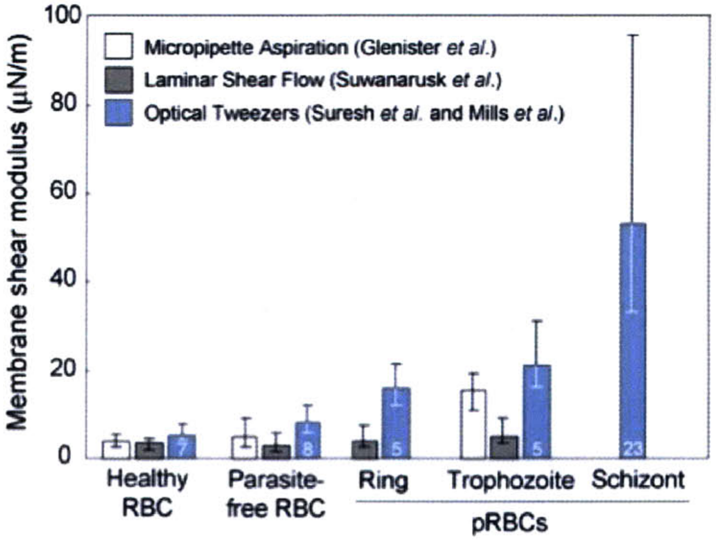

Figure 2-10: Membrane shear modulus of *P.f.* malaria as a function of intra-erythrocytic stage (Taken from Mills [66])

are presented in Figure 2-10. Most recently, Marinkovic et. al. [62] have characterized the complex modulus of parasitized RBCs as a function of temperature using magnetic twisting cyctometry (MTC). This combination of data generally shows that both membrane stiffness and viscosity increase with the development of the parasite. Extending this general result to larger applied forces, as well as looking at the contribution of an individual erythrocytic proteins using an advanced optical trapping method is a major contribution of this thesis work.

In addition to membrane mechanical property measurements, there have also been attempts at characterizing the microvascular flow behavior of parasitized RBCs. Most notably, Shelby et. al. and Handayani et. al. have used simple microfluidic structures to demonstrate that parasitized cells are less capable of traversing channels with smallest dimension ranging 2-8 μm [97, 46]. As with the aforementioned *in-vitro* studies of RBC flow in the microvasculature, these studies did not provide a robust characterization of the hydrodynamic forces (i.e applied pressure-velocity) such that the physiological relevance of the results may be inferred or that they may be applied to the development of analytical and computational models. Such quantitative characterizations of parasitized cells is a part of this thesis work. More recently, Antia et. al. have used microfluidic structures to investigate adhesive interactions of parasitized cells flowing over endothelial-lined surfaces [3]. Such adhesive interactions are not the subject of this thesis work. However, where appropriate, the interplay between adhesion and reduced deformability will be highlighted.

2.2 Background on Optical Trapping

Particle trapping by radiation pressure from a laser was first demonstrated by Ashkin [7] with subsequent development leading to the formation of the first stable, three dimensional optical trap from a single laser beam by Ashkin et. al. [9]. Shortly thereafter, Block et al. demonstrated one of the first applications of single beam optical trapping to biological systems in the measurement of the compliance of bacterial flagella [12]. Since that time, optical traps have been used extensively in the manipulation of biological cells and in the measurement of biological forces at the molecular level. The history of optical traps and their applications in biology is well-reviewed in the literature [8, 72, 96]. The optical trapping configurations used in this thesis work overcome two key disadvantages of the micropipette aspiration technique: (1) the presence of any increased cytoadherence causes friction along the wall of the pipette and complicates the interpretation of results and (2) micropipette aspiration is limited in its dynamic range and resolution (largely due to image processing and pressure control systems employed). With optical trap systems, the effects of adhesion on the interpretation of results is minimal, enabling the investigation of biological systems where both altered cytoadherence and deformability are present. This thesis will also show how the dynamic capabilities of an advanced optical trap allows for a host of new experiments to be performed on the RBC membrane. In addition, optical traps have the general advantage over micropipette and other experimental approaches (laminar shear flow, AFM) in that the applied stress state is more readily reproduced in three-dimensional computational simulations. This allows for a more accurate interpretation of experimental results and the ability to parametrically investigate the effects of experimental uncertainties such as cell shape and contact conditions on the extraction of mechanical properties. The following sections will establish the physical principles behind optical trapping systems and describe the major components and layout of an advanced trap system and the techniques that are commonly used in their calibration.

2.2.1 Principles of optical traping

A laser beam passing through a high numerical aperture microscope objective and focussed onto a dielectric particle, typically a glass or polystyrene bead, will place that particle in a three-dimensional potential well. Within this potential well, the interaction of the laser beam and the particle gives rise to two characteristic forces: the scattering force and the restoring, or gradient, force. The scattering force arises from the momentum transfer of light that is reflected from the particle, tending to push the particle away from the focal plane. The gradient force arises from the refraction of light, whereby the momentum transfer of photons will tend to pull the particle towards the focal point of the laser beam. The magnitude of these two forces vary with a host of factors, including the wavelength of light used and the laser power, the diameter of the particle. The mathematical description of these forces in the ray optics regime (i.e. particle diameter is much larger than the wavelength of light $d_p >> \lambda$) or the Rayleigh / electromagnetic dipole regime (i.e. $d_p >> \lambda$) are presented throughout the literature (e.g. [89, 96]). The gradient and scattering forces are described using ray optics in Figure 2-11.

In stable traps, the gradient force dominates the scattering force, allowing the particle to be maintained near the focal plane of the laser beam. This is achieved through the use of a laser with a TEM_{00} or Gaussian mode. At the center of the trap, a particle has a net force of zero. However, when displaced from the center of the trap by an outside force, the restoring force will act to pull the bead back to the focal point. The magnitude of this force is dependent on the displacement from the center of the trap. However, within a range of displacements, this force varies linearly with radial displacement. The radius of this linear region is typically on the order of $100nm - 1\mu m$, depending on the particle size. Within this linear regime,

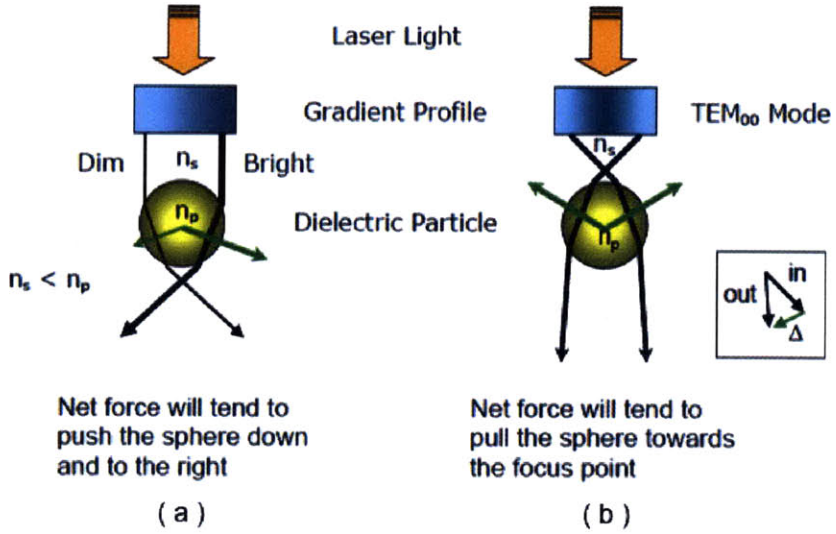

Figure 2-11: Ray optics representation of optical trapping. (a) Unstable trapping with a non-Gaussian beam, (b) Stable trapping with a Gaussian beam. In both cases, the particle is attracted towards the focal point. (inset) Refraction gives rise to the gradient/restoring force. Figure taken with permission from Brau [15]

the trap has a characteristic stiffness(κ) that may be empirically determined using one of the techniques described below. With a known trap stiffness, measuring the displacement of the bead from the center of the trap within this linear regime allows one to determine the force applied to the trapped particle.

2.2.2 Optical trapping system and components

The layout of a high-end optical trapping system employing laser-based detection is shown in Figure 2-12. This system, like most used in biological systems, employs a high-power infrared trapping laser ($\lambda = 1064nm$), colinear with a low-power infrared ($\lambda = 975nm$) detection laser. These wavelengths are used due to the limited absorption of biological molecules in the infrared spectrum, ensuring that the laser does not damage the molecules or cells when trapped particles are brought into contact with them. The lasers are passed through a high N.A. objective of a modified inverted microscope. At the specimen/imaging plane, the specimen is commonly mounted on a manual positioning stage and, as in the case of this thesis work, a high resolution, closed-loop controlled piezo stage capable of sub-micron displacements. An image of the condenser back focal plane formed by the detection laser is monitored on as position sensitive detector (PSD), which produces an X and Y voltage proportional to the position of a spot on is active sensing area (analogous to the quadrant photodiodes commonly used in AFM systems or earlier trapping systems). Alignment of the various optical paths are achieved through the use of three different telescope lens pairs. The trapping laser is steered using acoustic optical deflectors (AOD), which utilize piezo crystals to form diffraction gratings whose position response time is less than 1ms. Further details on the components used in this system are provided later and in the literature [57, 72, 96, 105].

2.2.3 Optical trap calibration

In the most commonly applicable configurations of an optical trap, the beads used have diameters that are comparable to the wavelength of the trapping laser (both approximately 1 μm). Thus, neither the ray optics or Rayleigh analyses can be used to assume a quantitative trap stiffness. Thus, an important aspect of employing optical traps is their bead position measurement and trap stiffness calibrations. The following summarizes the techniques most commonly used for these tasks. For further details on these techniques, the reader is referred to the reviews of Neumann and Block and Svoboda and Block [72, 105].

Bead position measurement system calibration

The typical calibration of the bead position detection system first requires the calibration of the CCD camera image. For this, a ruled or grid slide (i.e. Ronchi Ruling) may be used in order to establish the translation of CCD pixel coordinates to physical length units (nm or μm). Following this calibration, displacements of a trapped bead via changes in frequency of the AOD may be used to establish a correlation of AOD frequency with physical displacement. Using the AOD to move the trapped bead across the stationary detection laser and recording the corresponding signal on the

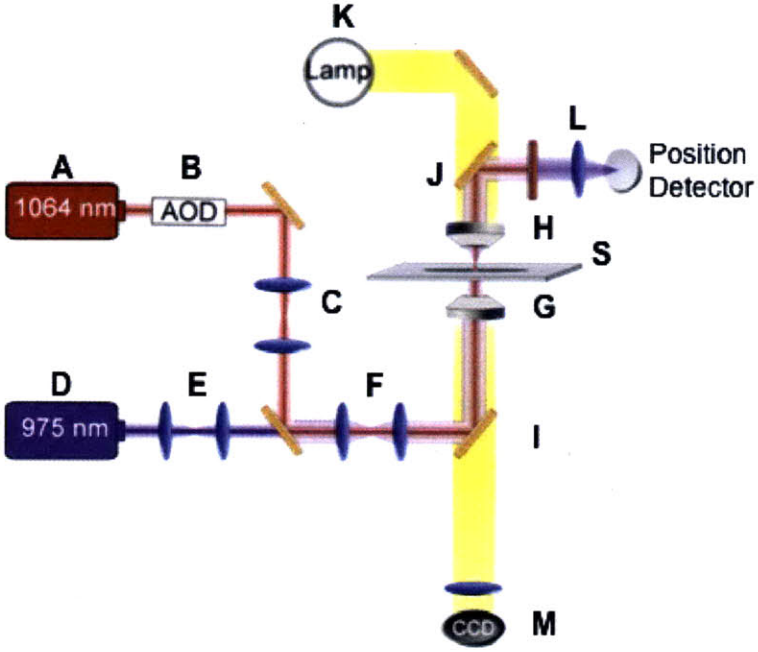

Figure 2-12: Representative layout of a high-end laboratory optical trap: (A) 1064 nm trapping laser, (B) acoustic optic deflector (AOD) for high speed beam steering, (C) telescope lens pair for trap beam alignment and expansion only, (D) 975nm detection laser, (E) telescope lens pair for detection beam alignment and expansion only, (F) telescope lens pair for simultaneous alignment and expansion of trap and detection beams, (G) high numerical aperture objective (60 - 100X, $N.A. > 1.4$), (H) condenser lens, (I) dichroic mirror used to integrate trap and detection beams into microscope optical path, (J) dichroic mirror to direct beams to detection branch, (K) bright field lamp, (L) position detection branch with band pass filter to eliminate 1064 nm wavelength and focus detection beam onto position sensitive detector (PSD), (M) CCD camera for conventional imaging, (S) specimen plane. Figure used with permission from P. Tarsa and caption used with permission from D. Appleyard [4]

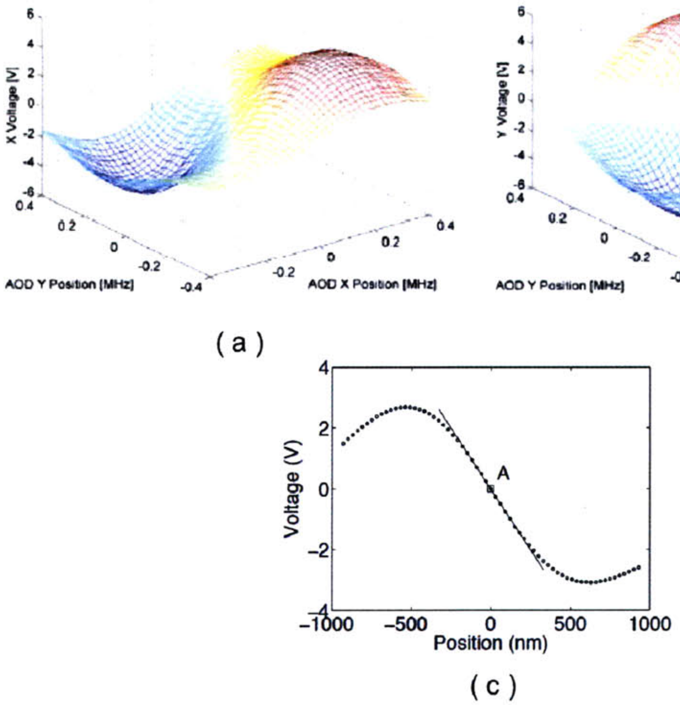

Figure 2-13: Example position calibration of an optically trapped bead. (a) and (b) show the X and Y voltage signals, respectively, from the PSD as the bead is moved across the detection region in both AOD coordinate directions. (c) The PSD signals as the bead is moved in a single direction, highlighting the linear detection region. (Figures (a) and (b) taken from Brau [15] and (c) from Appleyard [4].)

position sensitive detector (PSD) allows allows for the mapping of AOD frequency coordinates to PSD X and Y voltage signals. This mapping is commonly fit using a fifth-order polynomial. With the fifth-order function to map PSD X and Y voltages to AOD frequency coordinates, the previously established conversion from AOD frequency to physical displacement coordinates allows for a complete mapping of the PSD signal to the bead position relative to the center of the trap position. This mapping process is shown in Figure 2-13.

Trap Stiffness Calibration

Stokes drag technique: This technique employs the flow of fluid around a trapped bead and the corresponding measured displacement to determine the trap stiffness.

Fluid of a known viscosity (η) flowing past a bead with a known diameter (D_b) at a known velocity (V_f) will impart a steady-state drag force (F_D) of:

$$F_D = 3\pi\eta V_f D_b f_c \tag{2.8}$$

The Faxen's correction factor (f_c) is employed to correct for boundary effects when the bead is near a fixed surface.

$$f_c = \frac{1}{(1-(9/16)(a/h)+(1/8)(a/h)^3-(45/256)(a/h)^4-(1/16)(a/h)^5)} \tag{2.9}$$

Where a is the bead radius ($a = D_b/2$) and h is the height of the center of the bead above the surface. In most common trap configurations, the fluid velocity is applied via relative motions between the piezo stage and the trapped bead. This drag force will be countered by the trap restoring force ($F_{trap} = \kappa_x \Delta x$). Measuring the steady-state bead displacement during the fluid flow allows the determination of the trap stiffness (κ_x) using Equation 2.8.

Equipartition or Variance technique: This technique relies on the recognition that the trapped bead may be treated as a harmonic oscillator, at the center of a potential well. The equipartition theorem states that every degree of freedom of a harmonic potential contains $1/2k_BT$ of energy (where k_B is Boltzmann's constant and T is the absolute temperature). This thermal energy is related to the variance in mean squared displacement of the trapped particle as:

$$1/2k_BT = 1/2\kappa_x var(x - x_{mean})^2 \tag{2.10}$$

Thus, measuring the mean squared displacement of the bead under thermal/brownian motion for an appreciable time and knowing the absolute temperature of the medium allows for a direct inference of the trap stiffness. Note that this method does not require any knowledge of the medium viscosity, particle size, or distance off the coverslip.

Power spectrum calibration technique: The power spectrum of the thermal motion of a trapped bead has been shown to follow a Lorentzian profile [72]. This gives the following relationship:

$$S_{vv}(f) = \rho^2(k_B T)/(\pi^2\beta(f_o^2 + f^2)) \tag{2.11}$$

Where S_{vv} has units of V^2/Hz, T is the absolute temperature, f_o is the corner frequency and β is the drag coefficient $\beta = 3\pi\eta D_b f_o$ and ρ is a detector voltage to displacement calibration factor. Fitting the form of Equation 2.11 to a measured power spectrum of the bead allows for the extraction of the corner frequency f_c. This corner frequency is related to the trap stiffness as:

$$\kappa_x = f_o 2\pi\beta \tag{2.12}$$

Thus, while the magnitude of the power spectrum does rely on the detector position calibration, the determination of trap stiffness does not. Therefore, the trap stiffness may be calibrated with no knowledge of the detector voltage to displacement calibration and, for these purposes, ρ may be considered and arbitrary constant. However, for typical trap and stiffness configurations, the cut-off frequency is on the order of a few kHz. Therefore, a fast acquisition rate (typically 10kHz or greater) is required.

Chapter 3

Dynamic Characterization of Healthy and Malaria Infected Human Red Blood Cells Using Advanced Optical Trapping Techniques

3.1 Introduction

As discussed in Chapters 1 and 2, most quantitative measurements of RBC deformability characteristics (i.e. mechanical properties and time-dependent, viscous behaviors) have traditionally been limited to quasistatic measurements or measurements with limited temporal resolution (minimum time-scales and maximum frequencies of 0.1s or 10Hz, respectively). Typical transit times across entire microvascular regions of the body occur on the order of 1 second where transient deformations may occur over a much smaller fraction of that time [11]. Furthermore, *in-vitro* laboratory assays and diagnostic systems, in the interest of increased throughput, may operate using hydrodynamic conditions that are more severe than that seen physiologically.

Thus, there is an interest in examining the dynamic response of the human RBC both within and outside of physiological time-scales. This chapter describes the implementation and application of an optical trapping system aimed at measuring the response of the RBC over a large range of deformation rates and frequencies. In this work, a new loading configuration is developed and employed in order to measure the force-displacement response of healthy and parasitized RBCs. These results are presented along with the results of a parametric finite element study used to infer the elastic properties of the RBC under this new loading configuration.

3.2 Materials and Methods

3.2.1 Buffer, bead coating and cell solution procedures

Whole blood from healthy donors was obtained from an outside supplier (Research Blood Components, Brighton, MA). Blood was collected in plastic tubing with an acid-citrate-dextrose (ACD) solution. ACD serves as an anti-coagulant and glucose preservative solution. Upon reception, blood was stored at 4°C. All experiments on healthy cells were performed within 24 hours of acquiring blood samples.

The primary buffer used in all cell solution preparations and experiments was PBS(1X) with 0.1 %wt of Bovine Serum Albumin (BSA) (pH=7.4). 50 μL of whole blood is suspended in 0.5 mL of this buffer and centrifuged three times for 5 min. at 1000rpm. After each centrifugation, the supernatant is removed and replaced with fresh PBS/BSA(0.1%) buffer. 20 μL of this cell solution is added to 0.5 mL of PBS/BSA (0.1%wt) buffer, resulting in a final hematocrit level of 0.0002%.

Streptavidin-coated, polystyrene beads with diameters of 1.87μm (Bangs Laboratories) were used in this work due to their high refractive index. 50μL of this 1% wt. bead solution was incubated with 50μL of biotin-conjugated Conconavalin-A (ConA, Sigma C2272) at 4°C for a minimum of 30min. ConA binds to the RBC transmembrane protein, Band 3, allowing direct attachment to the RBC cytoskeleton. The membrane forces are fully transmitted to the trapped bead during experiments through the even stronger biotin-strepatavidin interaction. Following incubation with ConA, the bead solution was suspended in 0.5mL of PBS/BSA buffer and centrifuged three times for 6-8 min. each at 10,000rpm. After each centrifugation, the supernatant is removed and the bead pellet is re-suspended in 0.5mL of PBS/BSA. $20\mu L$ of the final bead solution is added to the 0.0002% cell solution to form the final bead/cell suspension.

Experiments on *P.f.* parasitized cells were done using the same cell and bead concentrations and the same final buffer suspensions as healthy cells. Parasite cultures were maintained by a collaborator within this thesis author's research group (Dr. M. Diez-Silva). The details of the culture protocol as well as the genetic modification routines are found in [67].

3.2.2 Optical trapping techniques

Instrumentation design and position calibration

The optical trapping instrument used in this work is shown in Figure 3-1. The general design of the system is similar to designs of advanced optical trapping systems found in the literature [12, 57, 72, 105]. The specific system in this work was implemented largely as a collaborative effort between the author and Dr. John Mills [66]. Additional significant contributions to the design and implementation were also made by Dr. Matt Lang, Dr. Jorge Ferrer, Dr. Ricardo Brau and Dr. Kevin Turner. The optical layout and a detailed overview of the design and features of the trap was presented in Section 2.2.2. In Figure 3-1, several key components are highlighted: the trapping laser (IPG Photonics Fiber Laser YLD, 1064 nm wavelength, 10W maximum power), dual-axis acousto-optical defelctors (Intra-Action Corp., DTD-276HD6), position detection laser (Thorlabs 975nm diode laser), and position sensitive detector (PSD) (Pacific Silicon, DL100-7PCBA3) and closed-loop controlled piezoelectric positioning stage (Physik Instrumente P-527 stage with E517.3CD controller). Temperatures up to $45°C$ are controlled using a combination of a custom-made microscope objective heater and resistive heaters mounted to the top of a sample chamber. Heater set-

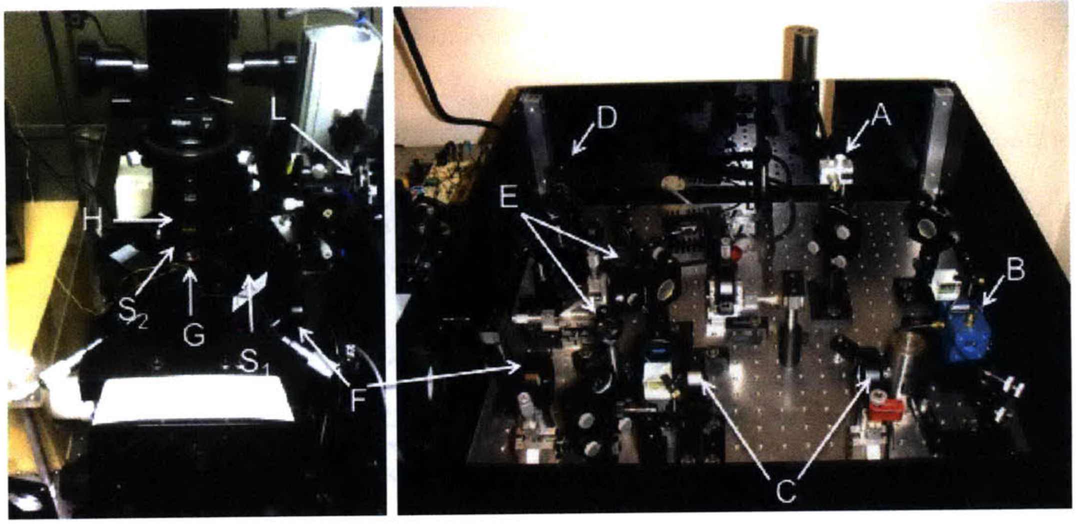

(a) **(b)**

Figure 3-1: Optical trapping system implemented and used in this work, separated by (a) the specimen plane, condenser and position sensing branch and (b) the trap, detection laser and supporting alignment and beam steering optics. Labels correspond to schematic view of the system given in Figure 2-12, where the specimen plane is comprised of the piezoelectric stage and the sample chamber, S_1 and S_2 respectively. The 100X microscope objective used (G) is shown with the objective heater used in physiological temperature experiments.

points required to achieve a desired temperature in the sample chamber are calibrated using a K-type thermocouple embedded in a representative sample chamber. Bright field optical images and videos are taken using a Dage CCD100 camera.

In the configuration shown, the trapping laser is split into two separate paths using a polarizing beam splitter. The second trapping branch (not shown in Figure 2-12) is not used in this work. However, as a result of this split and additional power losses through the AODs, typical laser output powers (1-3W) result in much lower powers into the microscope objective (200-700mW). A neutral density filter is placed in the path of the detection laser, resulting in objective powers of less than 10mW. Thus, the position detection laser does not influence the stiffness characteristics of trapped beads during the experiments.

As described previously, within a range of radial displacements from the center of the trap, PSD voltage coordinates correspond to a unique (X,Y) position in the specimen plane. This range of displacements is termed the "linear detection regime." Translating the PSD voltage coordinates to bead position coordinates is done using the position calibration routines described in section 2.2.3. The resulting calibration function used in this work is a fifth order polynomial mapping the PSD voltages (Vx, Vy) to bead positions (Xpos,Ypos). The form of the fifth order polynomial function and a typical set of coefficients are presented in Equations 3.1, 3.2, and Table 3.1, respectively. With the beads used in this work ($1.87\mu m$ diameter polystyrene), the linear detection regime has a typical radius of 540nm.

$$\begin{aligned}
&Xpos[nm] = \\
&\quad A_x(Cx_1 + Cx_2Vx + Cx_3Vy + Cx_4Vx^2 + Cx_5Vy^2 + Cx_6Vx^3 + \\
&\quad Cx_7Vy^3 + Cx_8Vx^4 + Cx_9Vy^4 + Cx_{10}Vx^5 + Cx_{11}Vy^5 + Cx_{12}VxVy + \\
&\quad Cx_{13}Vx^2Vy + Cx_{14}VxVy^2 + Cx_{15}Vx^3Vy + Cx_{16}Vx^2Vy^2 + Cx_{17}VxVy^3 + \\
&\quad Cx_{18}Vx^4Vy + Cx_{19}Vx^3Vy^2 + Cx_{20}Vx^2Vy^3 + Cx_{21}VxVy^4)
\end{aligned} \tag{3.1}$$

$$\begin{aligned}
&Ypos[nm] = \\
&\quad A_y(Cy_1 + Cy_2Vx + Cy_3Vy + Cy_4Vx^2 + Cy_5Vy^2 + Cy_6Vx^3 + \\
&\quad Cy_7Vy^3 + Cy_8Vx^4 + Cy_9Vy^4 + Cy_{10}Vx^5 + Cy_{11}Vy^5 + Cy_{12}VxVy + \\
&\quad Cy_{13}Vx^2Vy + Cy_{14}VxVy^2 + Cy_{15}Vx^3Vy + Cy_{16}Vx^2Vy^2 + Cy_{17}VxVy^3 + \\
&\quad Cy_{18}Vx^4Vy + Cy_{19}Vx^3Vy^2 + Cy_{20}Vx^2Vy^3 + Cy_{21}VxVy^4)
\end{aligned} \tag{3.2}$$

The PSD signal voltages are passed through a low pass filter and amplifier (Krohn-Hite Model 3384 or Standford Research Systems Model SR640) with a typical cut-off frequency setting of 30kHz and input and output gains between 5-30dB. Gains are adjusted such that the signal voltages within the detection region typically fall within the range of $\pm 5V$, giving approximately $10mV/nm$ of displacement. These signals

Xpos		Ypos	
A_x	3132.02	A_y	3031.03
Cx_1	26.001204	Cy_1	26.001099
Cx_2	0.020008	Cy_2	−0.017028
Cx_3	0.025211	Cy_3	0.027547
Cx_4	0.000125	Cy_4	−0.000458
Cx_5	0.000260	Cy_5	−0.000156
Cx_6	−0.000148	Cy_6	0.000168
Cx_7	−0.000201	Cy_7	−0.000240
Cx_8	−0.000015	Cy_8	0.000007
Cx_9	−0.000010	Cy_9	0.000001
Cx_{10}	0.000015	Cy_{10}	−0.000016
Cx_{11}	0.000002	Cy_{11}	0.000007
Cx_{12}	0.000423	Cy_{12}	0.000661
Cx_{13}	0.000027	Cy_{13}	−0.000272
Cx_{14}	−0.000240	Cy_{14}	0.000167
Cx_{15}	0.000012	Cy_{15}	−0.000020
Cx_{16}	−0.000006	Cy_{16}	−0.000017
Cx_{17}	−0.000007	Cy_{17}	−0.000012
Cx_{18}	−0.000011	Cy_{18}	0.000028
Cx_{19}	0.000023	Cy_{19}	−0.000041
Cx_{20}	0.000001	Cy_{20}	0.000026
Cx_{21}	0.000007	Cy_{21}	−0.000013

Table 3.1: Typical fifth-order polynomial calibration coefficients used to map PSD voltages to position in the specimen plane

are collected using a National Instruments data acquisition system (PCI-MIO-16E-1 with BNC-2090 accessory) featuring 12 bit data acquisition over up to 16 channels with a maximum range of $\pm 10V$. This range and digital resolution gives a maximum analog signal detection resolution of 5mV, corresponding to a resolution of the detection system of approximately 1nm of bead displacement. These displacements may be monitored continuously at a maximum sampling rate of 100kHz/channel. Such capability to monitor nm level displacements at such high frequencies is a significant advantage of this system over trap systems that rely on image processing and image correlation techniques from captured images, which are subject to diffraction and frame-rate limitations.

Trap stiffness calibration

The three most common techniques to calibrate optical traps were discussed in Section 2.2.3. In this work, the stokes drag technique was used to determine the trap stiffness. This technique is especially useful to determine larger trap stiffnesses where passive, thermally driven bead displacements approach the detection resolution limit and their measurement is more readily influenced by the presence of electronic noise. As described in section 2.2.3, this technique requires a fluid of known viscosity and a bead of known diameter and height above the surface. The BSA/PBS buffer used in this work has a viscosity equal to that of water (1mPa s) [113, 73, 20]. The bead height above the surface is set by first bringing a trapped bead in contact with the coverslip surface via incremental movements of the piezo stage. Contact with the coverslip surface is indicated by a slight change in the focus of the bead image seen on the CCD camera. This is followed by a relative displacement of the stage of the desired bead height. The estimated uncertainty in the bead height above the coverslip surface due to this procedure is approximately 100nm. Fluid velocities are imparted by relative motion of the piezo stage at velocities ranging from $300\mu m/s - 2000\mu m/s$ and stage displacement ranges $50 - 150\mu m/s$. A typical stokes calibration data set is shown in Figure 3-2. For powers into the microscope objective ranging from 200mW - 700mW (laser output powers 1-3W), the trap stiffnesses measured by this combina-

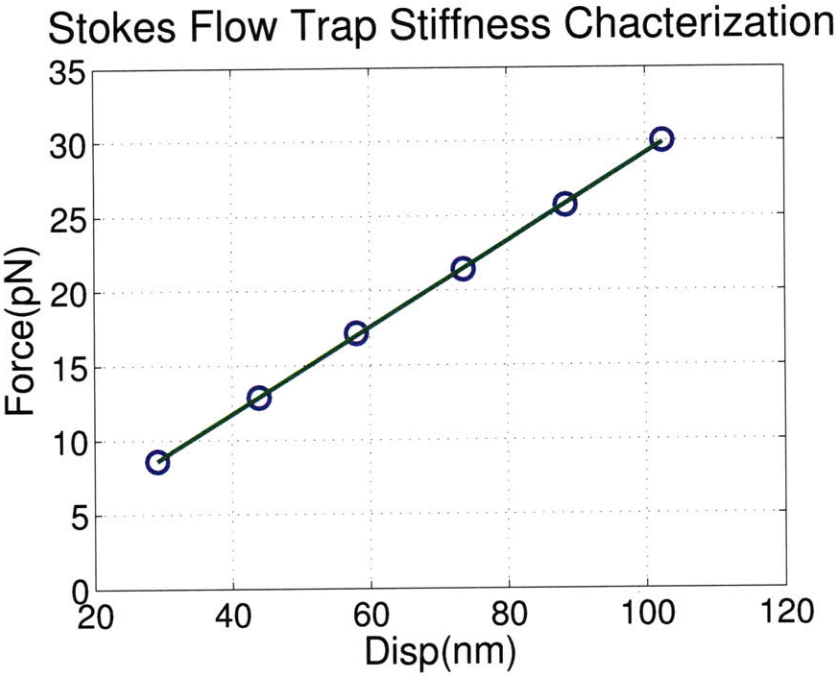

Figure 3-2: Calibration of optical trap using stokes flow technique. (Trap stiffness $\kappa = 0.29pN/nm$.)

tion of techniques range from 0.1 - 0.3pN/nm. These characteristic stiffnesses across the 540nm linear detection region result in maximum forces up to 150pN in these experiments. Higher trap stiffnesses are achievable using different combination of power and bead diameters as well as changes in the optical path, such as including a beam expansion telescope on the trapping branch. However, for the work presented here, these forces are sufficient. The variation in stiffness measurements using the stokes calibration technique, as well as the differences in stiffnesses measured via stokes flow calibration and the variance technique were both between $10-20\%$. This uncertainty in trap stiffness translates to an equal uncertainty in applied force. However, this uncertainty is small when considering the inherent variability in the biological systems explored in this work. Thus, these uncertainties do not significantly affect the results and conclusions presented in subsequent discussion.

Stage position detection

The piezoelectric stage used in this work is controlled using a collection of LabView drivers provided by the manufacturer. A GPIB communication interface (NI-GPIB-USB-HS) is used to send commands to and receive signals from the stage controller. In the case of relatively large deformations (greater than a few microns) and slow displacements (less than 20 $\mu m/s$), this interface suffices for getting concurrent measurements of the bead and stage position during an experiment. In high rate/frequency experiments, the GPIB communication is too slow to provide adequate sampling rates. In order to overcome this limitation, a novel optical lever system was designed using an approach analogous to the deflection detection system used in an atomic force microscope (AFM). In this system, depicted in Figure 3-3, a coverslip mounted to the housing of the piezo stage serves as the cantilever. This cantilever is deflected by a glass slide fixed to the piezo stage surface. A 590nm (red) laser (Thorlabs) is reflected off the coverslip surface and onto a position sensitive detector (PSD) that is mounted at a position that gives approximately 1m of optical path length from the stage. With this path length and the configuration depicted, stage displacements on the order of $1\mu m$ result in approximately $1mm$ displacements of the laser spot. The resulting signal change due to these displacements is used in conjunction with the known displacements from the stage controller to establish a calibration between the change in Stage PSD signal and stage displacement. An example of such a calibration is shown in Figure 3-4. Stage position calibrations are performed either immediately before or immediately following an experiment in which high deformation rates or oscillation frequencies are used (greater than $10\mu m$ or $10Hz$, respectively). Immediately prior to such experiments, the laser spot of the optical lever is centered on the stage PSD using the mirror shown in Figure 3-3. During an experiment, the analog voltage signal of the stage PSD is monitored concurrently with the bead position system described above. This allows for direct monitoring of the stage position at 10-100 times larger sampling rates of the stage position during an experiment (10-100kHz, compared to approximately 1kHz sampling of the stage position using GPIB

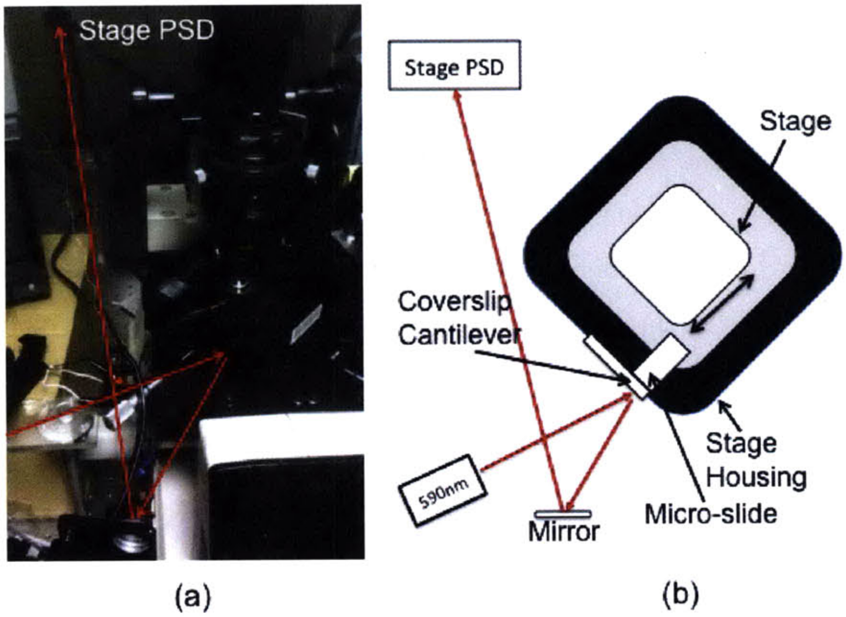

Figure 3-3: (a) Picture and (b) schematic of optical lever system used to measure stage displacements for large displacement rates and high oscillation frequencies (typically greater than $10\mu m/s$ and $10Hz$, respectively).

communication with the stage controller).

Loading configurations and testing procedures

The two loading configurations used in this work, termed Configuration A and B, are displayed in Figure 3-5. In Configuration A the RBC is adhered to the coverslip in a small region and the trapped bead is adhered to the RBC membrane at a diametrically opposed area. In this configuration, non-specific bonding between the RBC and the coverslip is relied upon to achieve an appropriate level of coverslip adhesion. In order to promote the proper level of adhesion, standard pre-cleaned coverslips are used and their surfaces are first incubated with a high BSA concentration buffer for approximately 1 minute (1% wt. BSA/PBS, compared to 0.1% BSA/PBS used in cell and bead solution preparation). Experiments are carried out on cells that are found to be adhered in the proper manner. In order to achieve Configuration B, bead/cell solutions suspended in 0.1% wt. BSA/PBS are used with coverslips that are more thoroughly cleaned using a combination of KOH etching and ethanol rinses

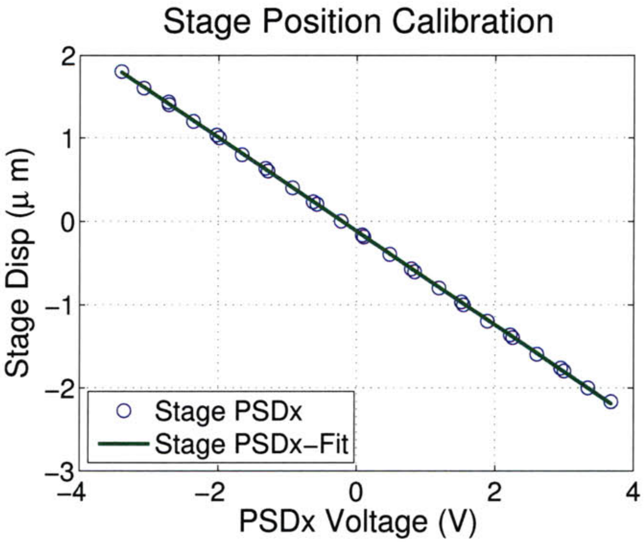

Figure 3-4: Example calibration of optical lever system used for stage position detection, showing approximately $0.5 \mu m/V$.

(see Appendix A for details). No BSA/PBS incubation step is used. This procedure promotes additional adhesion between the RBC membrane and coverslip such that cells are frequently adhered in a perimeter with a characteristic diameter (d_{cc}). This loading configuration was developed as a part of this thesis work due to its capability to achieve a consistent set of contact conditions that remained constant over the course of multiple experiments performed on the same cell, enabling much of the dynamic characterizations discussed below.

During a typical experiment, a trapped bead is set at a height above the coverslip surface between $0.25 - 0.6 \mu m$ and calibrated using the position calibration routines described above. Following calibration, slight adjustments to the height of the bead above the surface (less than 200nm total changes) are made in order to bring the edge of the cell in focus with the bead and ensure the bead may be accurately placed on the perimeter of the RBC. The bead is brought into contact with an RBC using relative motions of the piezo stage. This initial contact typically results in an initial pre-load on the RBC membrane. In both loading configurations, additional load is applied to the cell via relative motion of the piezo stage. Trapped bead displacements are measured during this loading process and the applied load is inferred by multiplying

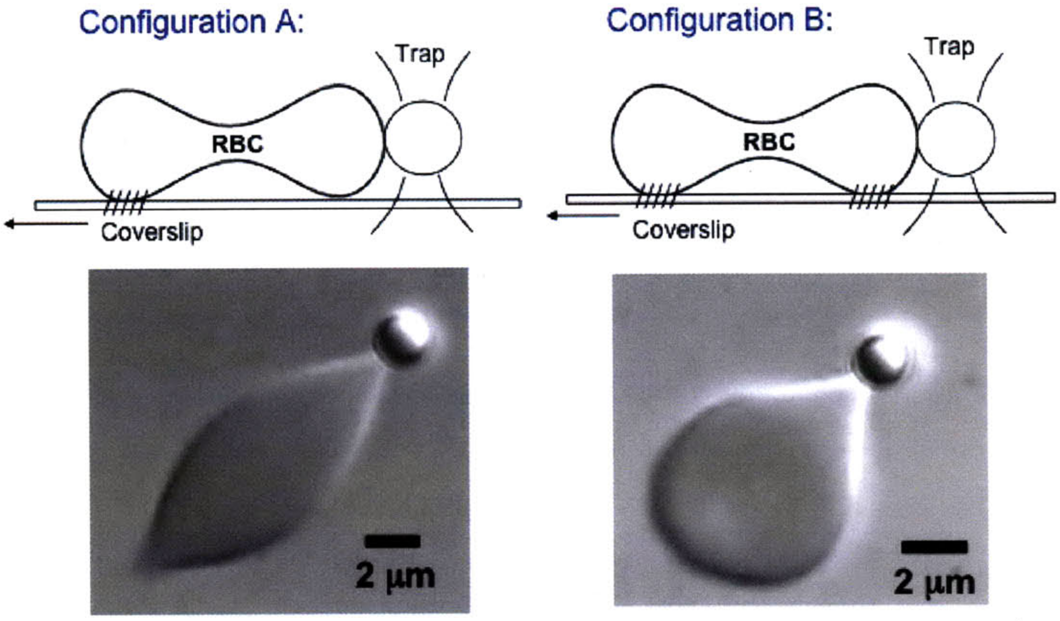

(a) (b)

Figure 3-5: Loading configurations relying on (a) limited coverslip adhesion and (b) circular coverslip adhesion and examples of a healthy cell under 60pN and 30pN load, respectively.

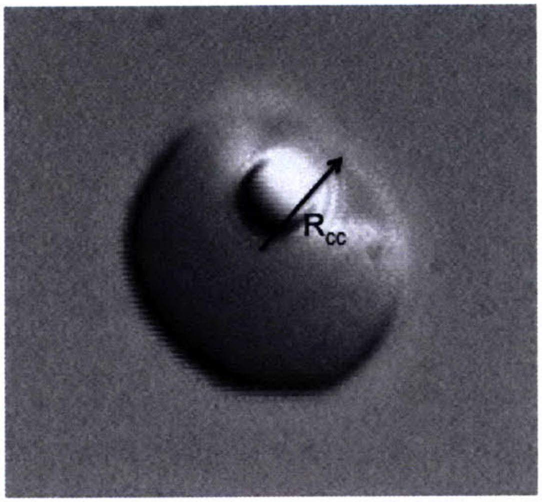

Figure 3-6: Determination of the coverslip contact radius (R_{cc}) via relative motion of a weakly-trapped bead relative to the cell to reveal the perimeter of contact between the cell and the coverslip.

these measured displacements by the previously calibrated trap stiffness. For reasons that will become clear in subsequent discussion, the load-displacement characteristics of this deformation are typically plotted as the axial cell diameter versus applied load, where the axial cell diameter refers to the length of the cell along the loading direction. The axial cell diameter is taken to be the initial cell diameter (measured using images captured on the CCD camera), plus the displacement of the piezo stage (monitored using the stage controller or the optical lever system described above), minus the displacement of the bead during loading. In addition, videos of each experiment are used to measure the major diameter of contact between the cell and the bead. In the case of load configuration B, the diameter of the perimeter of contact with the coverslip is measured by first displacing the bead further from the surface at reduced laser power and moving the stage in the opposite direction from loading. This reveals the contact edge between the cell and the coverslip surface, the radius and diameter of which may be determined using the initial diameter of the cell and the location of the contact edge relative to a diametrically opposed point on the cell. An example of this process and the resulting measurement of the coverslip contact radius is shown in Figure 3-6.

3.2.3 RBC elastic property extraction

Hyperelastic constitutive behavior of the RBC

The loading configurations used in this work and the relatively complex geometry of the RBC impede the use analytical solutions for standard geometries (e.g. cylinders, spheres, discs) in comparable loading configurations to determine the mechanical properties of the RBC membrane from the measured load-displacement characteristics. Previous work done within this thesis author's research group has shown that a combination of dimensional analysis and a parametric finite element study can be used to account for all of the relevant experimental parameters and determine the elastic properties of the RBC membrane from a measured load-displacement response. This was done for loading configuration A and presented in [29]. A contribution of this thesis work is the application of this approach to loading configuration B. What follows is a summary of this approach and its application to both loading configurations.

The combination of the phospholipid bilayer and underlying spectrin network is idealized as an isotropic, incompressible, rubber-elastic material with a reduced-polynomial strain energy potential of the Yeoh form:

$$U = \frac{G_o}{2}(\lambda_1^2 + \lambda_2^2 + \lambda_3^2 - 3) + C_3(\lambda_1^2 + \lambda_2^2 + \lambda_3^2 - 3)^3 \tag{3.3}$$

The material is assumed to be incompressible (i.e. $\lambda_1\lambda_2\lambda_3 = 1$). The initial shear modulus (G_o) is related to the initial membrane shear modulus and initial thickness (μ_o and h_o, respectively) by $G_o = \mu_o h_o$. C_3 is a higher order modulus that accounts for the hardening behavior of the membrane under large stretch levels ($\lambda > 2$). As presented by Dao et. al [29], equation 3.3 may be expressed in terms of the membrane shear moduli as:

$$\Phi = \frac{\mu_o}{2}(\lambda_1^2 + \lambda_2^2 + \lambda_3^2 - 3) + \mu_h(\lambda_1^2 + \lambda_2^2 + \lambda_3^2 - 3)^3 \tag{3.4}$$

Where μ_o and μ_h are the initial and hardening membrane shear moduli, respectively. Recent work has shown that this constitutive response replicates the response given by molecular mechanics-based approaches [29, 58, 5, 6]. However, in much of the classical work on RBC mechanics, the RBC membrane is modeled as a Neo-Hooken material, which is equivalent to Equation 3.3 with $\mu_h = 0$. In addition, these descriptions also impose area conservation (i.e. $\lambda_1\lambda_2 = \lambda_3 = 1$). This constraint is generally thought to be imposed by the phospholipid bilayer, which is highly resistant to changes in area. However, using fluorescent-labeled micropipette aspiration experiments, Discher et. al [32] showed that the spectrin cytoskeleton may deform significantly, relative to the lipid bilayer. These results suggest that, while the bilayer may impose a global area constraint on the membrane, local area conservation of the spectrin network may not be appropriate. Thus, for this work, only local volume conservation is assumed for the membrane. However, as noted by Dao et. al., under the assumption of area conservation, a given uniaxial response would imply an initial membrane shear modulus that is 75% of that without area conservation.

Non-dimensionalized RBC force-displacement response

Using the aforementioned constitutive response, the force-displacement of the RBC membrane during loading configuration A and configuration B may be analyzed using dimensional analysis. This approach was first reported in Dao et. al. [29] for configuration A. Here, that approach is summarized and extended to configuration B.

In the first loading configuration, the axial diameter (D_A) during loading will be a function of the following variables:

$$D_A = f(F, \mu_o, \mu_h, D_o, d_{cb}) \tag{3.5}$$

Where:

F - applied load

μ_o - initial membrane shear modulus

μ_h - membrane hardening modulus

D_o - initial cell diameter

d_{cb} - contact diameter between the trapped bead and the cell

In the second configuration, the contact area with the coverslip must also be taken into account, such that Equation 3.5 becomes:

$$D_A = f(F, \mu_o, \mu_h, D_o, d_{cb}, d_{cc}) \tag{3.6}$$

Where d_{cc} is the diameter of the coverslip contact area.

According to the PI theorem, the following dimensionless groups exist for this set of parameters:

$$\Pi_1 = \frac{D_A}{D_o}, \Pi_2 = \frac{F}{\mu_o D_o}, \Pi_3 = \frac{\mu_h}{\mu_o}, \Pi_4 = \frac{D_o}{d_{cb}}, \Pi_5 = \frac{D_o}{d_{cc}} \tag{3.7}$$

And, equations 3.5 and 3.6 may be written in terms of these dimensionless groups, such that:

$$\frac{D_A}{D_o} = f\left(\frac{F}{\mu_o D_o}, \frac{\mu_h}{\mu_o}, \frac{D_o}{d_{cb}}\right) \tag{3.8}$$

$$\frac{D_A}{D_o} = f\left(\frac{F}{\mu_o D_o}, \frac{\mu_h}{\mu_o}, \frac{D_o}{d_{cb}}, \frac{D_o}{d_{cc}}\right) \tag{3.9}$$

For loading configurations A and B, respectively.

Dao et. al. [29] performed extensive finite element simulations to show that, in configuration A, for a given set of contact conditions and material properties, the dimensionless groups containing the force and axial diameter, Π_1 and Π_2 respectively, may be related by the following functional form:

$$\frac{D_A}{D_o} = 1 + B\left(\frac{F}{\mu_o D_o}\right)^C \tag{3.10}$$

Where B and C are functions of the remaining dimensionless groups (Π_3, Π_3, Π_4).

In this thesis work, a finite element model was implemented using commercial software (ABAQUS) to examine the applicability of this functional form to configuration B. In this finite element model, half symmetry was invoked and the RBC membrane was modeled using shell elements. In light of the negligible effect that bending was found to have on the force-extension behavior in these and previous studies [29, 30], the shell thickness was set to give a typical bending rigidity of $B_o = 2 \cdot 10^{-19} Nm$ in all simulations, unless specified otherwise. The geometry of the RBC is taken to be that described by Fung et. al. [43], where the total cell thickness as a function of the distance from the axis of symmetry (r) may be described by:

$$D(r) = [1 - (r/R_o)^2]^{1/2}[C_o + C_2(r/R_o)^2 + C_4(r/R_o)^4] \tag{3.11}$$

Where, for the average RBC radius of $R_o = 3.91\mu m$, the shape coefficients are: $C_o = 0.81\mu m, C_2 = 7.83\mu m, C_4 = -4.39\mu_m$. An example of the finite element mesh and strain contours during the loading process for a given set of contact conditions and average material properties are shown in Figure 3-7.

For a given set of contact conditions and modulus ratio (i.e. a fixed Π_3, Π_4, Π_5) and varying initial shear modulus, it was found that Equation 3.10 is also applicable to configuration B. This is demonstrated in Figure 3-8, where various force-displacement responses collapse along a single line described by equation 3.10. The values of B and C will be different for variations in Π_3, Π_4 and Π_5. For configuration A, Dao et. al showed that the following functional forms may be used to accurately replicate the force-displacement response seen in the results of hundreds of finite element studies [29]:

$$\begin{aligned}
B &= B_1 + B_2\left(\ln\left(\tfrac{D_o}{d_{cb}} - B_3\right)\right), \\
B_1 &= b_1, \\
B_2 &= b_2 - b_3\left(\ln\left(\tfrac{\mu_h}{\mu_o}\right)\right), \\
B_3 &= b_4 + b_5\left(\ln\left(\tfrac{\mu_h}{\mu_o}\right)\right) + b_6\left(\ln\left(\tfrac{\mu_h}{\mu_o}\right)\right)^2
\end{aligned} \tag{3.12}$$

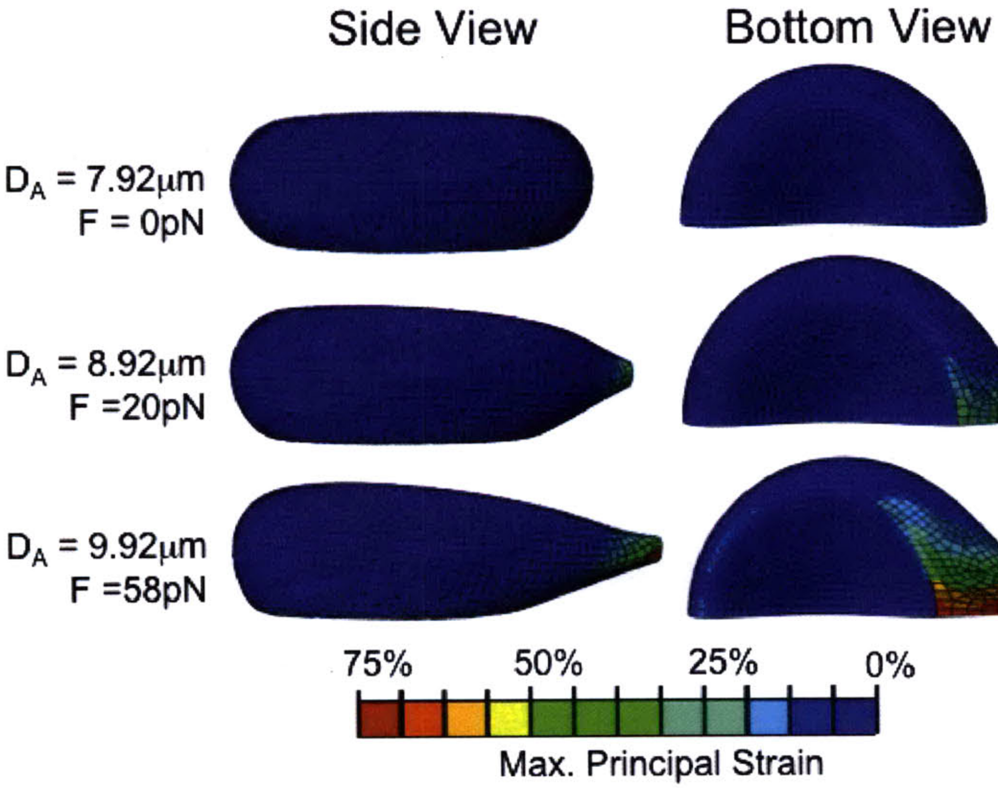

Figure 3-7: Finite element simulations of RBC loaded under load configuration B with $\mu_o = 7.5\mu N/m, \mu_h/\mu_o = 0.05, d_{cc} = 5.78\mu m, d_{cb} = 0.96\mu m$.

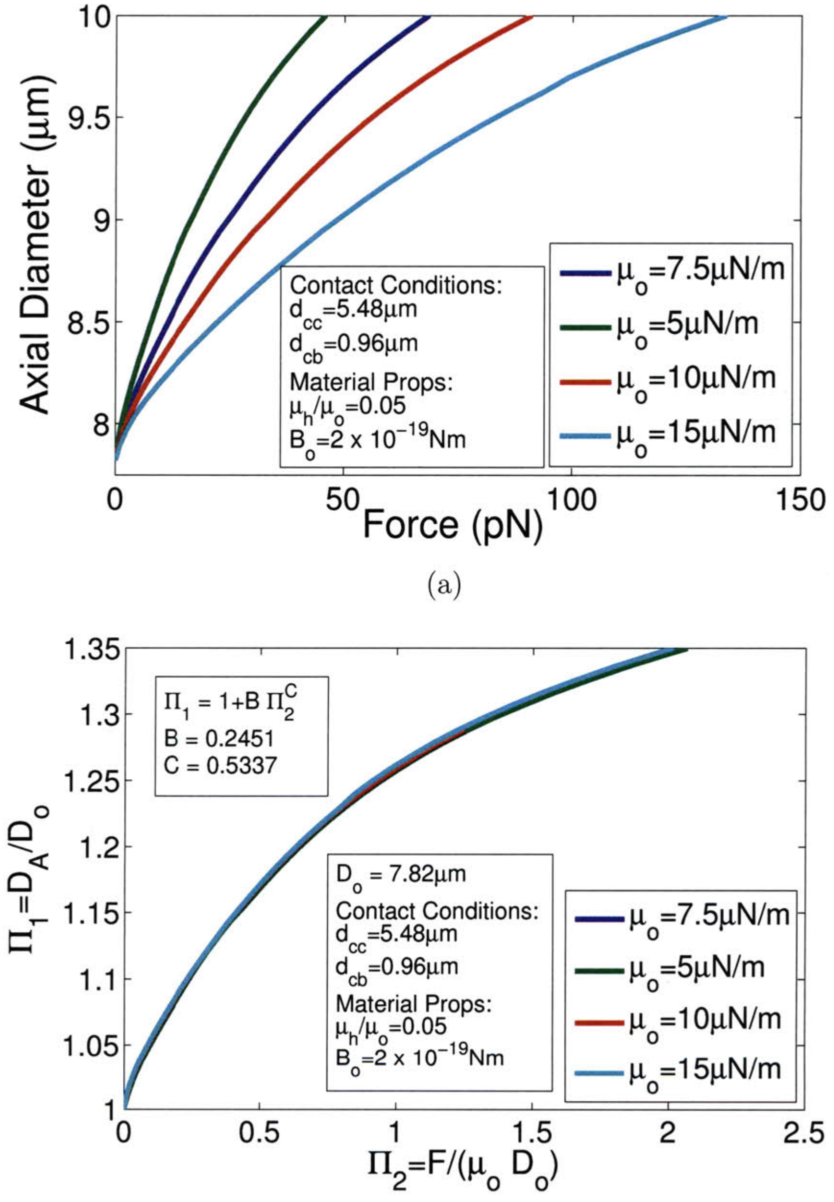

(a)

(b)

Figure 3-8: (a) Effect of initial shear modulus (μ_o) on the axial displacement vs. force response of an RBC for a fixed set of contact conditions and moduli ratio; (b) non-dimensionalized response where all curves in (a) may be described by Equation 3.10 with the displayed values of B and C.

$$\begin{aligned}
&C = C_1 - C_2 \left(\ln \left(\tfrac{D_o}{d_{cb}} - C_3 \right) \right), \\
&C_1 = c_1 + c_2 \left(\ln \left(\tfrac{\mu_h}{\mu_o} \right) \right) + c_3 \left(\ln \left(\tfrac{\mu_h}{\mu_o} \right) \right)^2, \\
&C_2 = c_4, \\
&C_3 = -c_5 - c_6 \left(\ln \left(\tfrac{\mu_h}{\mu_o} \right) \right) - c_7 \left(\ln \left(\tfrac{\mu_h}{\mu_o} \right) \right)^2
\end{aligned} \tag{3.13}$$

Following this same framework, a similar set of non-dimensional equations may be used to describe loading configuration B, where the additional dimensionless group $\Pi_5 = D_o/d_{cc}$ is taken into account:

$$\begin{aligned}
&B = B_1 + B_2 \left(\ln \left(\tfrac{D_o}{d_{cb}} - B_3 \right) \right) + B_4 \left(\ln \left(10 \left(\tfrac{D_o}{d_{cc}} \right) - B_5 \right) \right), \\
&B_1 = b_1, \\
&B_2 = b_2 - b_3 \left(\ln \left(\tfrac{\mu_h}{\mu_o} \right) \right), \\
&B_3 = b_4 + b_5 \left(\ln \left(\tfrac{\mu_h}{\mu_o} \right) \right) + b_6 \left(\ln \left(\tfrac{\mu_h}{\mu_o} \right) \right)^2, \\
&B_4 = b_7 - b_8 \left(\ln \left(\tfrac{\mu_h}{\mu_o} \right) \right), \\
&B_5 = b_9 + b_{10} \left(\ln \left(\tfrac{\mu_h}{\mu_o} \right) \right) + b_{11} \left(\ln \left(\tfrac{\mu_h}{\mu_o} \right) \right)^2
\end{aligned} \tag{3.14}$$

$$\begin{aligned}
&C = C_1 - C_2 \left(\ln \left(\tfrac{D_o}{d_{cb}} - C_3 \right) \right) - C_4 \left(\ln \left(10 \left(\tfrac{D_o}{d_{cb}} \right) - C_5 \right) \right), \\
&C_1 = c_1 + c_2 \left(\ln \left(\tfrac{\mu_h}{\mu_o} \right) \right) + c_3 \left(\ln \left(\tfrac{\mu_h}{\mu_o} \right) \right)^2, \\
&C_2 = c_4, \\
&C_3 = -c_5 - c_6 \left(\ln \left(\tfrac{\mu_h}{\mu_o} \right) \right) - c_7 \left(\ln \left(\tfrac{\mu_h}{\mu_o} \right) \right)^2, \\
&C_4 = c_8, \\
&C_5 = -c_9 - c_{10} \left(\ln \left(\tfrac{\mu_h}{\mu_o} \right) \right) - c_{11} \left(\ln \left(\tfrac{\mu_h}{\mu_o} \right) \right)^2
\end{aligned} \tag{3.15}$$

Where the constants and range of parameter studied for each loading configuration are presented in Tables 3.2 and 3.3, respectively.

Using this system of non-dimensional equations, the initial shear modulus and modulus ratio may be determined from the measured force-displacement response of an optical trapping experiment using an optimization routine such as that described by Dao et. al [29].

Configuration A [29]				Configuration B			
b_1	0.42054	c_1	0.5998124	b_1	0.014655	c_1	219.43
b_2	0.059016	c_2	-0.0574776	b_2	0.020626	c_2	2.9280
b_3	-0.01489195	c_3	-0.00348081	b_3	0.0080519	c_3	0.047723
b_4	3.247842	c_4	0.04985	b_4	3.3536	c_4	0.011784
b_5	0.4191616	c_5	-1.93967	b_5	0.15593	c_5	0.045700
b_6	0.0424185	c_6	-2.090442	b_6	0.0081847	c_6	-0.062250
b_7	N/A	c_7	-0.2258287	b_7	0.084877	c_7	0.079457
b_8	N/A	c_8	N/A	b_8	0.0067689	c_8	25.602
b_9	N/A	c_9	N/A	b_9	10.920	c_9	5218.6
b_{10}	N/A	c_{10}	N/A	b_{10}	0.68419	c_{10}	-561.80
b_{11}	N/A	c_{11}	N/A	b_{11}	0.077350	c_{11}	25.007

Table 3.2: Fitted coefficients for non-dimensional equations.

	Configuration A	Configuration B
$\Pi_1 = D_A/D_o$ (fit range)	$[1, 1.8]$	$[1, 1.25]$
$\Pi_3 = \mu_h/\mu_o$	$[0.011, 0.1]$	$[0.01, 0.1]$
$\Pi_4 = D_o/d_{cb}$	$[3.5, 15.64]]$	$[3.92, 15.64]$
$\Pi_5 = D_o/d_{cc}$	N/A	$[1.30, 1.564]$

Table 3.3: Range of parameters explored in finite element studies to determine non-dimensionalized system of equations describing the load-displacement response of the RBC under loading configurations A and B.

3.3 Results and discussion

3.3.1 Elastic and viscoelastic characterization of healthy RBCs

An example force-displacement response of a healthy RBC under load configuration B and the predicted response using the mechanical properties extracted from the foregoing system of equations is shown in Figure 3-9.

In Figure 3-10, results of elastic characterizations of healthy cells using configuration B are compared to results yielded by configuration A and other techniques. The average initial membrane shear modulus of healthy RBCs ($\mu_o = 4.99 \mu N/m$) measured using loading configuration B are comparable to those from the other techniques and fall within the broader range of perviously reported values discussed in Table 2.1.

As discussed in Section 2.1.2, a classical experimental characterization of the viscoelastic characteristics of the RBC involves measuring the viscoelastic shape recov-

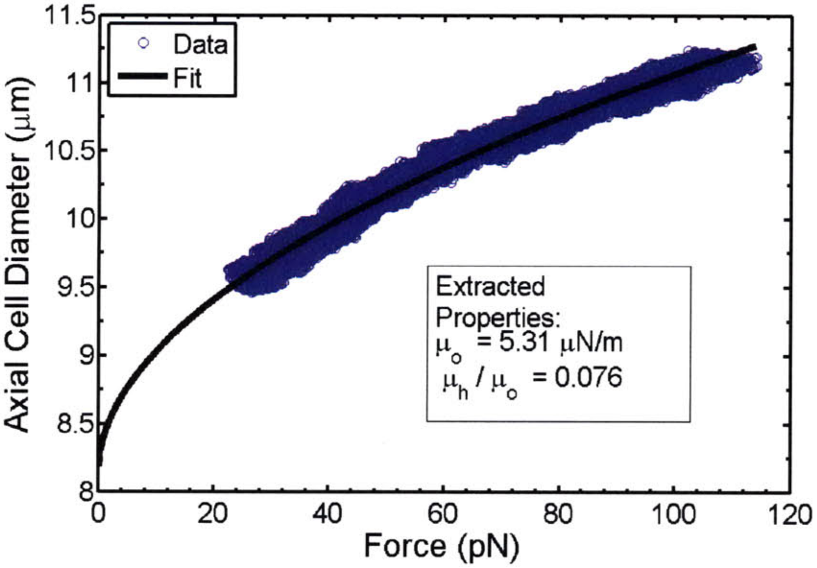

Figure 3-9: Force-displacement response of a healthy RBC and extracted modulus using non-dimensionalized system of equations.

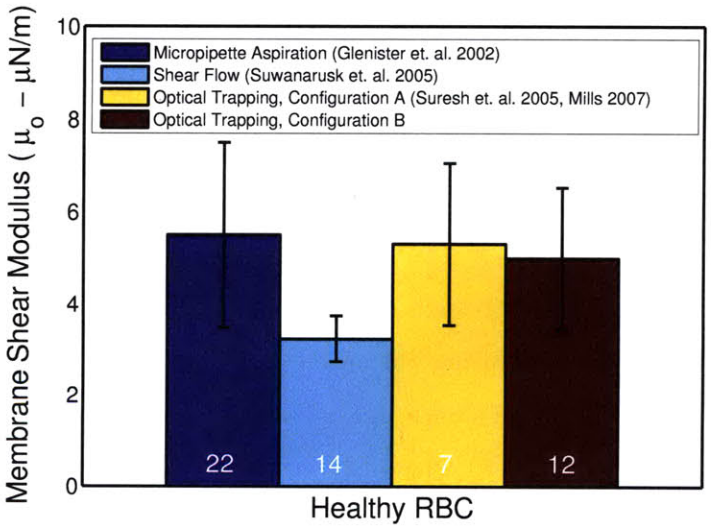

Figure 3-10: Comparison of average healthy RBC membrane shear modulus measured using load configuration B under an imposed displacement rate of $1\mu m/s$ with results of other quasistatic approaches. (Error bars represent standard deviations of N cells, where N is the number of cells measured for each technique and indicated on bargraph.)

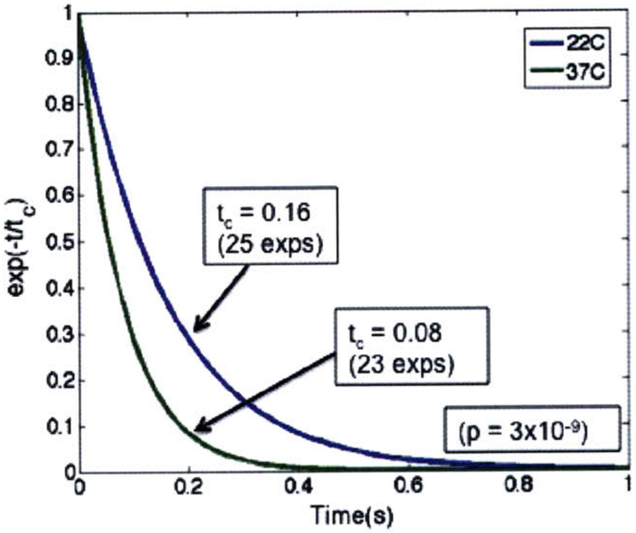

Figure 3-11: Viscoelastic shape recovery tests performed at room and physiologically normal, body temepratures.

ery behavior after extension via diametrically opposed pipettes [39, 49]. Modeling the RBC membrane as a Neo-hookean material with an additional viscosity term in the constitutive law (akin to a standard linear solid, or kelvin, model), a single characteristic time-scale (t_c, where $t_c = \eta/\mu_o$) is used to describe the viscous behavior of the membrane (see Chapter 2). This work determined characteristic time-scales of $t_c = 0.1 - 0.3s$ [39, 49]. Mills first extended this technique to loading via optical trapping under loading configuration A, yielding similar results [68]. In this thesis work, similar experiments were performed at room and physiological temperatures. Results of those experiments are presented in Figure 3-11. It has been shown previously that the membrane shear modulus does not vary significantly over this temperature range. Thus, the measured change in characteristic time-scale corresponds to a reduction in apparent membrane surface viscosity by a factor of two at physiological temperature.

However, such shape recovery experiments are limited in the time-scales over which they can probe the dynamic response of the membrane. They also do not explicitly account for the loading history of the RBC prior to the measured shape recovery. Furthermore, other relevant work of Engelhardt et. al. [35, 36] and Puig-De-Morales-Marinkivic et. al. [86], discussed in Section 2.1.2, suggest that this single time-scale description may not be appropriate for a large range of deformation rates and frequencies. However, these studies are themselves limited in the levels of deformation achievable and the deformation modes being applied (i.e. bending vs. shear extension of the membrane). Such limitations are overcome using the optical trapping system developed in this work where the combination of a high resolution piezo stage and continuous force-displacement measurement capabilities enable two classes of experiments: (1) stress relaxation experiments and (2) frequency-dependent viscous dissipation characterizations.

Stress-relaxation of RBC membranes

The stress relaxation experiments developed in this work consist of three stages: (i) a loading portion at a prescribed displacement rate, (ii) a holding portion where the maximum stage displacement is maintained and (iii) an unloading portion, where the stage is returned to its initial position at a slow displacement rate (typically $1\mu m/s$). Using load configuration B, multiple stress-relaxation experiments were performed over a range of displacement rates ($1-100\mu m/s$) on the same cell. Thus, the explicit effect of this loading rate on the response of the cell may be observed. An example of the load-time history of a healthy RBC loaded using displacement rates ranging from $1-100\mu m/s$ is shown in Figure 3-12. During the displacement of the stage, the cell experience a peak load that is dependent on the applied displacement rate. After this peak load, the cell relaxes to a value that is roughly independent of the applied load rate. This relaxed load level typically achieves a near steady-state value in approximately 4-5 seconds.

The application of high deformation rates will impart a fluid drag force on the trapped bead that may affect the measured force-displacement characteristics. However, under the conservative assumption that the maximum displacement rate of $100\mu m/s$ produces the same fluid flow past the trapped bead (i.e. the bead-fluid system immediately reaches steady-state), Equation 2.8 estimates these forces to be approximately 2-3pN, which is small compared to the forces measured in these experiments. Therefore, the load-time histories presented in Figure 3-12 suggest a

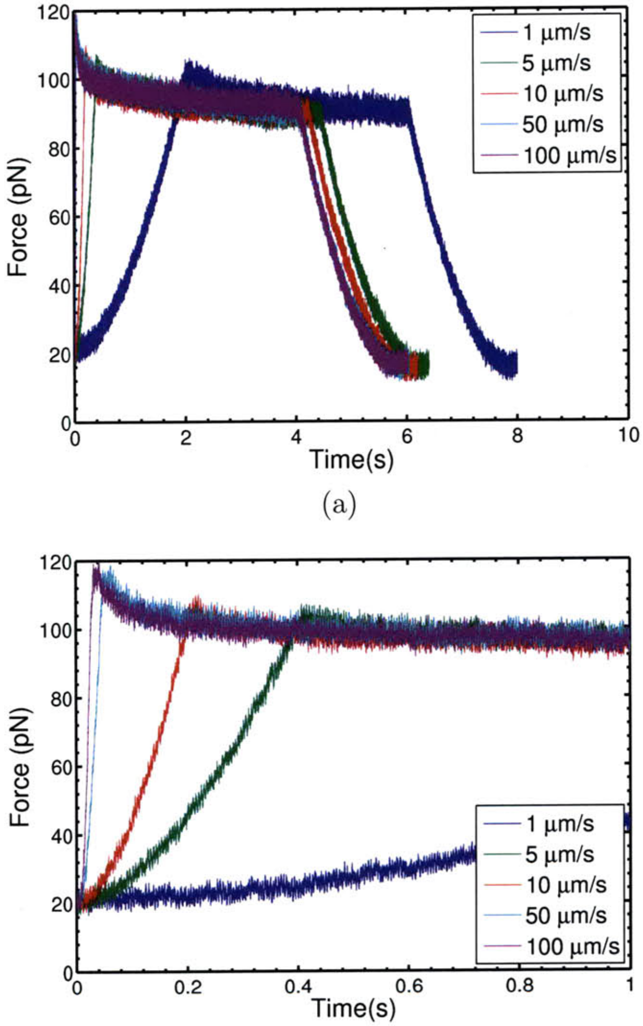

(a)

(b)

Figure 3-12: Example time-history of loading a healthy RBC with approximately $2\mu m$ of displacement imposed under configuration B at deformation rates from $1 - 100\mu m/s$. The stage is held at its maximum displacement for 4sec and returned to its initial position at a rate of $1\mu m/s$. (a) and (b) display different ranges of time for the same experiments performed on the same cell.

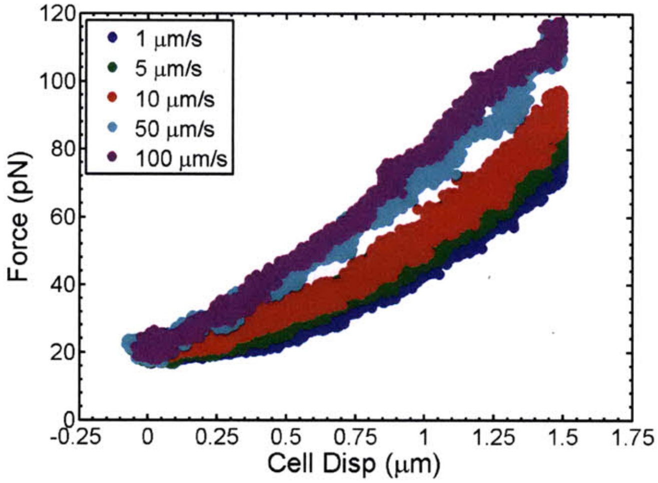

Figure 3-13: Typical force-displacement response of healthy RBC under varying displacement/deformation rates ($1 - 100\mu m$).

stiffening behavior of the RBC membrane when it is loaded under large displacement rates. This stiffening behavior is clearer when looking at the corresponding load-displacement characteristics of the loading portion of the relaxation experiment, as seen in Figure 3-13.

A simple way of interpreting this load displacement response is in terms of an "apparent" initial shear modulus (μ_{app}) using the scheme presented in Section 3.2.3. Such an interpretation is seen in Figure 3-14, where the apparent shear modulus of the RBC membrane increases by nearly a factor of 2 with displacement rates up to $100\mu m/s^1$.

More insight into the appropriate viscoelastic constitutive model of the RBC may be gained by examining the time-dependent relaxation behavior exhibited in Figure 3-12. A detailed development of such a constitutive model is beyond the scope of this thesis work. Instead, this work aims to demonstrate the application of the experimental techniques developed in evaluating constitutive theories previously put forth in the way of aiding the development of future models. One class of constitutive theories employed previously are descriptions that model the RBC membrane as a combination of elastic and dissipative elements, such as the finite viscoelastic, stan-

---

[1] In these and many subsequent results, "p" values represent the results of a Mann-Whitney U test, where the p-values indicated represent the probability that the two compared data-sets are derived from the same population of data.

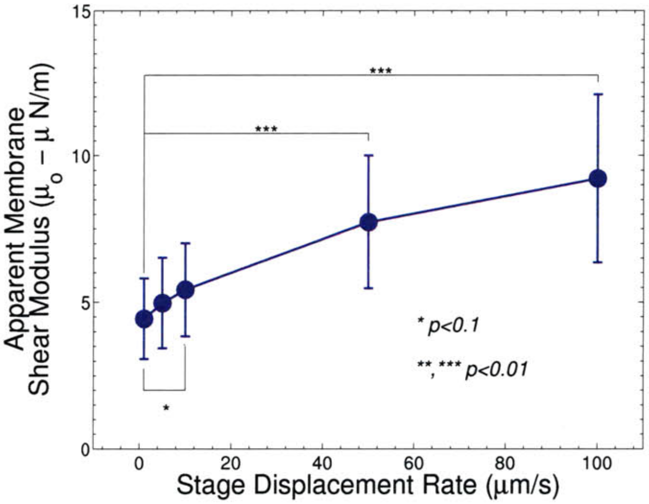

Figure 3-14: Apparent shear modulus as a function of displacement rate. Data points and error bars represent the average and standard deviations of 12 experiments, respectively.

dard linear solid model employed by Hochmuth and Evans (see Chapter 2 and above). In such models, the elastic and dissipative characteristics of the RBC membrane are described by a combination of spring and dashpot elements. Each viscous, or dashpot, element introduces an exponential term (e^{-t/t_c}) with a characteristic time-scale (t_c) into the relaxation behavior of the RBC. Hochmuth and Evans proposed a single time-scale description $(t_c = 0.1 - 0.3)$ where that time-scale is equal to the ratio of membrane viscosity to membrane shear modulus $(t_c = \eta/\mu_o)$ [39, 49]. Engelhardt et. al. proposed a constitutive model of the RBC membrane involving a combination of a short and long dissipative time-scales $(t_{c1} = 1.0s, t_{c2} = 0.1s)$ [35, 36]. Examining the RBC relaxation behavior in this work found a strong correlation between the necessary time-scales required to describe the relaxation behavior and the loading rate of the RBC. As shown in Figure 3-15, under loading rates less than $10\mu m/s$, a single exponential time-scale was sufficient to describe the observed relaxation behavior. Whereas, the relaxation behavior of cells subjected to larger loading rates greater than $10\mu m/s$ were typically best described by a two-term exponential decay, suggesting the presence of two viscous time-scales. This was especially true for cells deformed at the highest deformation rates ($50\mu m/s$ and $100\mu m/s$). However, as shown in 3-16, the exact value of these time-scales varied significantly for different cells tested at the same loading rate, especially in the case of the single time-scale description of cells subjected to slow deformation rates.

While these results do not eliminate the application of standard spring/dashpot models to describe the dissipative nature of the RBC membrane, they do suggest that a single time-scale description of the RBC membrane is insufficient to capture behaviors observed at high deformation rates. The lack of an inherent time-scale in the time-dependent deformations of living cells has been identified in other systems, such as smooth muscle cells [31, 106]. In this and other work, the elastic and dissipative characteristics of the cytoskeleton (typically expressed as the complex storage (G') and loss (G") modulus) are found to follow a power-law dependence on frequency. A similar power-law dependence was first suggested for red blood cells by Puig-De-Morales-Marinkovic et. al. [86]. However, this work, using magnetic twisting cytometry, examined smaller deformation levels than explored here. In this thesis work, the relevance of a power-law description of the dissipative characteristics of the RBC membrane was considered by examining the energy dissipation of the membrane subjected to different loading rates. The energy dissipation of the membrane was determined by integrating the force-displacement loading histories of the membrane, shown for $1, 10, 100\mu m/s$ displacement rates in Figure 3-17.

As shown in Figure 3-18, it was found that this energy dissipation (E_{dis}) ranged from $(20 - 80 \cdot 10^{-18} J)$. In principle, this energy dissipation may arise from either the RBC membrane or the internal fluid. In order to estimate the contribution of the hemoglobin to the overall energy dissipation, one may consider a simple model of the deformations imposed in these experiments as analogous to the shear of two parallel plates with length equal to the initial cell diameter $D_o = 8\mu m$ and width equal to the bead diameter $D_b = 2\mu m$. With a hemoglobin viscosity of $\eta_{Hb} = 6mPas$, the fluid shear stress (τ_{xy}) may be expressed as:

$$\tau_{xy} = \eta_{Hb} \frac{U}{\delta} \tag{3.16}$$

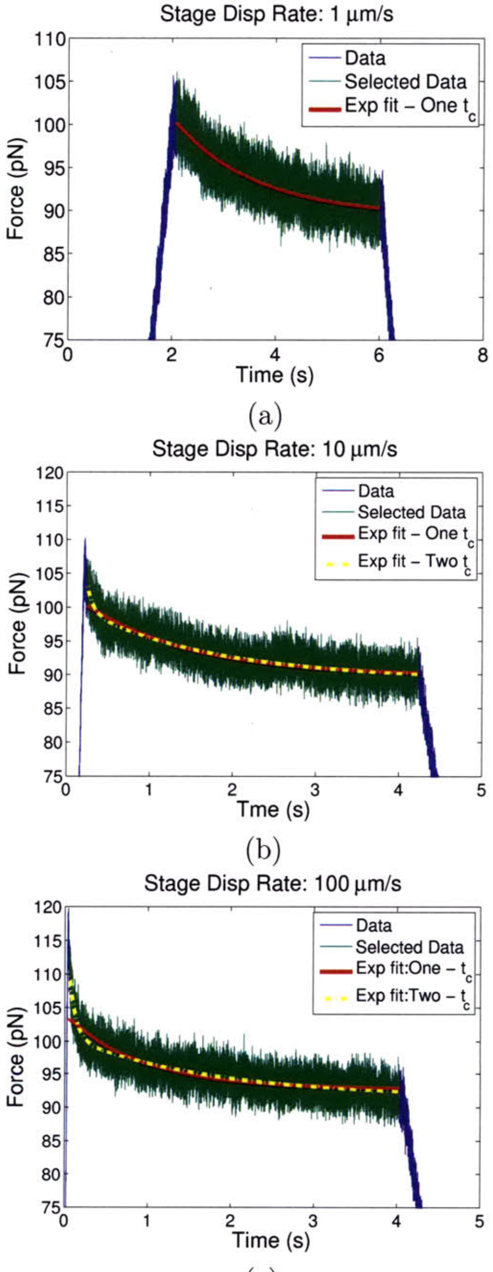

(a)

(b)

(c)

Figure 3-15: Example of exponential fits of relaxation behavior of an RBC following loading via a stage displacement rate of (a)$1\mu m/s$, (b)$10\mu m/s$ and (c)$100\mu m/s$.

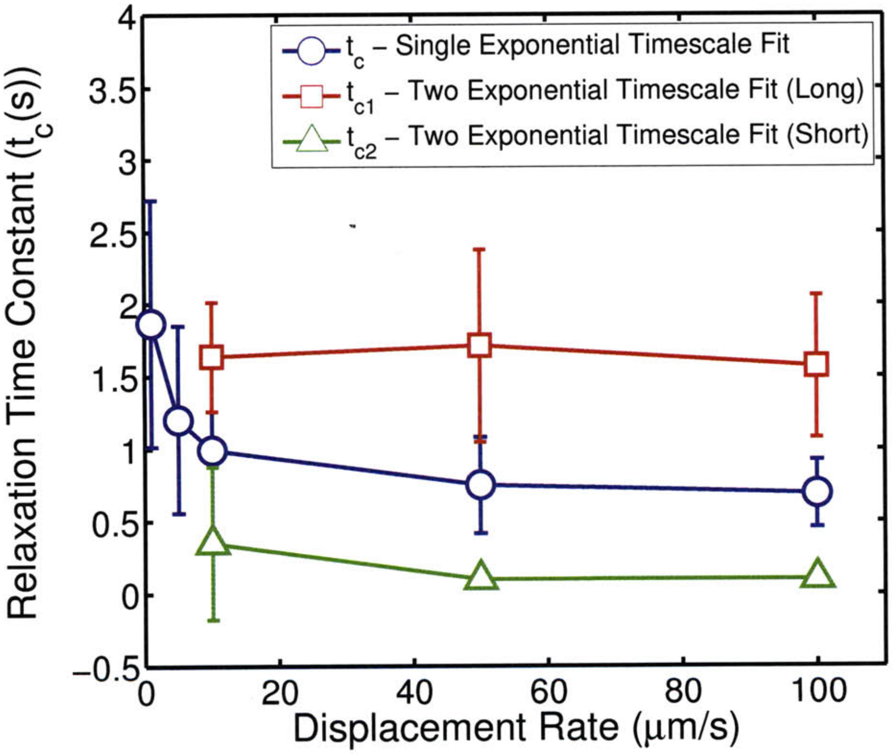

Figure 3-16: Relaxation time constants of two-timescale exponential fits compared to single timescales. Data points and error bars represent an average and standard deviation of 6 cells.

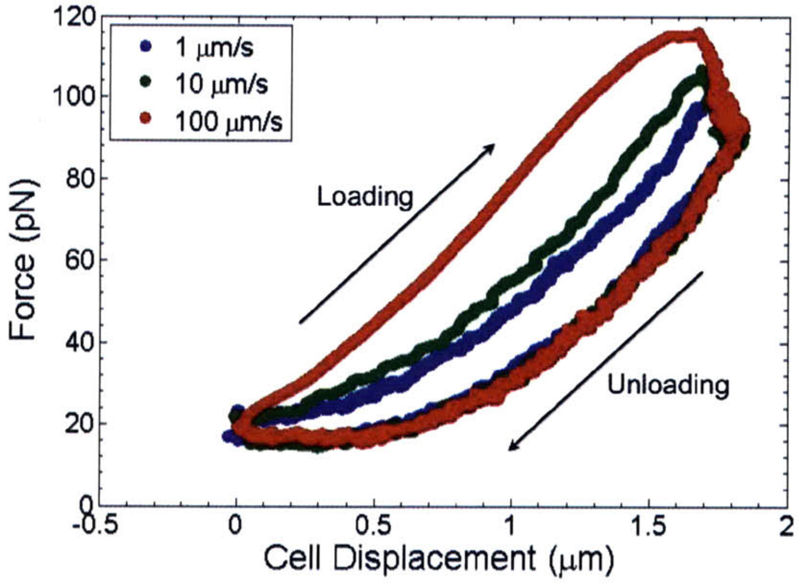

Figure 3-17: Corresponding load-displacement histories of a healthy RBC subjected to loading via stage displacement rates of $1, 10, 100\mu m/s$, hold periods of 4 seconds and unloading rates of $1\mu m/s$.

Where U is the relative velocity of the plates, which is taken as the displacement rate ($U = 1\mu m/s - 100\mu m/s$) and $\delta = 2.6\mu m$ is the maximum thickness of the cell (i.e., the "gap" between the plates). The rate of work, or power, is given by the product of the shear force and displacement velocity:

$$W_{rate} = F_{shear}U = \tau(D_o D_b)U \tag{3.17}$$

Over the time duration of the loading and unloading portion of these experiments, this gives an energy dissipation in the range of $E_{Hb} = (0.06 - 6) \cdot 10^{-18}J$. Thus the hysteresis observed is dominated by energy dissipation in the RBC membrane. The RBC membrane dissipation displays a power-law dependence on loading rate where $E_{dis} \sim d^{\alpha}_{rate}$ and $\alpha = 0.25$, which compares well to the results of Yoon et. al., who found a nearly identical power-law description of the energy dissipation with deformation rate under a smaller range of deformation rates and lower forces (maximums of $20\mu m/s$ and $40pN$, respectively). Thus, these results suggest that constitutive models employing power-law descriptions of viscous dissipation of the

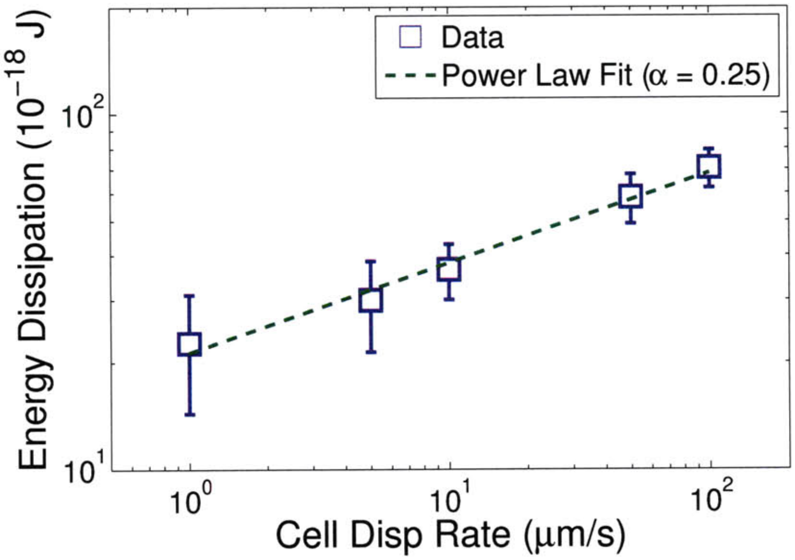

Figure 3-18: Energy dissipation of stress relaxation experiments. Data points and error bars represent average and standard deviations for 6 cells.

RBC membrane may be most appropriate to describe the viscoelastic behavior of the RBC under a wide range of dynamic conditions.

Dissipative Behavior of Healthy RBC Membranes Subjected to Periodic Loading

A second set of dynamic experiments was performed in order to explicitly investigate the frequency-dependent behavior of the RBC membrane when subjected to periodic loading conditions. In these experiments, the cell is subjected to periodic loading of a particular amplitude (A_1) and frequency (f) via time-varying displacements of the stage ($x(t)$) of the form:

$$x(t) = A_1(sin(2\pi f(t + \frac{0.75}{f})) + \frac{1}{2}) \tag{3.18}$$

Note that this motion is not symmetric in compressive or tensile loading about the initial position. Rather, only stage displacements that would typically provide tensile loading are used. Significant compressive loading cannot practically be investigated

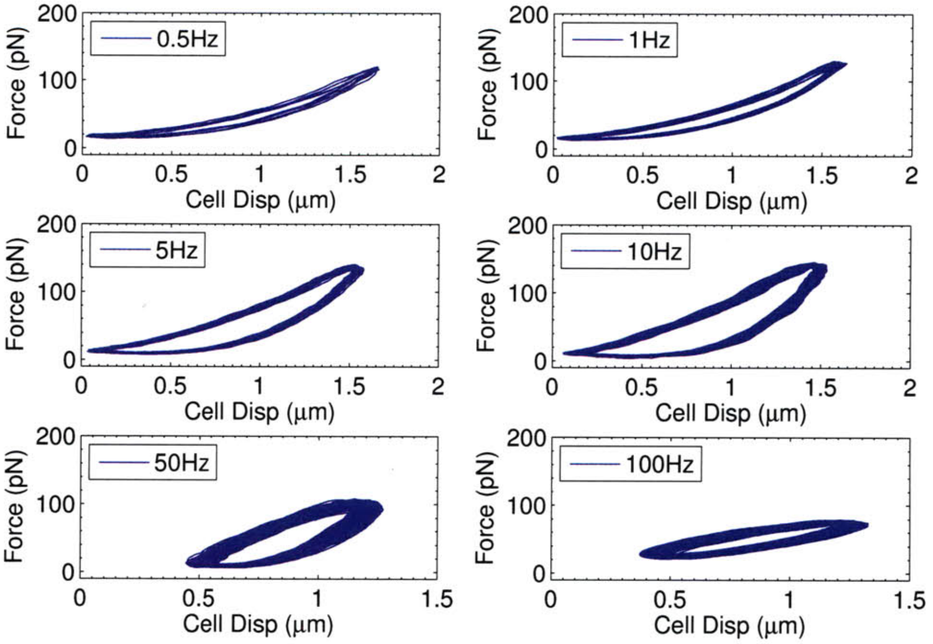

Figure 3-19: Typical load-displacement behavior of a healthy RBC subjected to sinusoidal displacements of varying frequency.

as such loads would result in the bead being significantly displaced upward, out of the focal plane of the trap.

The force-displacement response of the RBC membrane as a function of displacement frequency is shown in Figure 3-19. The non-linear response of the RBC shown in Figure 3-19 and the inherent dependence of this response on the contact conditions preclude the direct application of simple theory to directly determine the frequency-dependent complex moduli of the RBC membrane, such as that presented in for isotropic, viscoelastic medium in [16]. Developing the appropriate frequency-dependent constitutive behavior is beyond the scope of this work. However, as with the discussion of relaxation behavior presented above, it is instructive to consider the energy dissipation in these frequency-dependent measurements in the way of guiding the development of future models.

The average energy dissipation per cycle for 6 measured cells is shown in Figure 3-20. At high frequencies (typically greater than 25Hz), the stage displacement exhibits

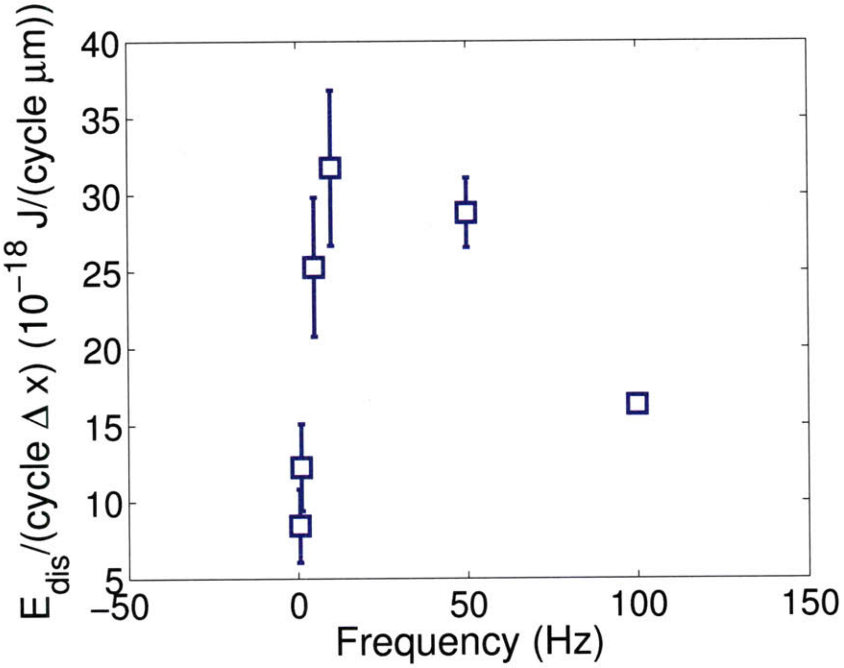

Figure 3-20: Energy dissipation behavior of healthy RBCs subjected to sinusoidal displacements.

errors in matching the exact range of prescribed positions. In an attempt to account for this error over the entire range of frequencies, the energy dissipation is expressed in a per unit change in axial cell diameter (ΔD_o) basis. However, even correcting for this behavior, it is clear from Figure 3-20 that the same power-law dependence with loading rate does not hold over the whole range of frequencies examined here. Instead, examining the energy dissipation on log-scales, shown in Figure 3-21, suggests that the energy dissipation may be related to the loading frequency by two power-law regimes $E_{dis} \sim f^{\alpha}$, where $\alpha = 0.45$ from 0.5-10Hz and $\alpha = -0.82$ from 50-100Hz and a transition between increasing energy dissipation to decreased energy dissipation exists between 10-50Hz.

In order to make an adequate comparison of the stress-relaxation behavior and the periodic loading behavior of the RBC, one must first consider the magnitude of the loading rates employed in the sinusoidal load applications. The average and maximum deformation rates for the given combinations of frequencies and displacement

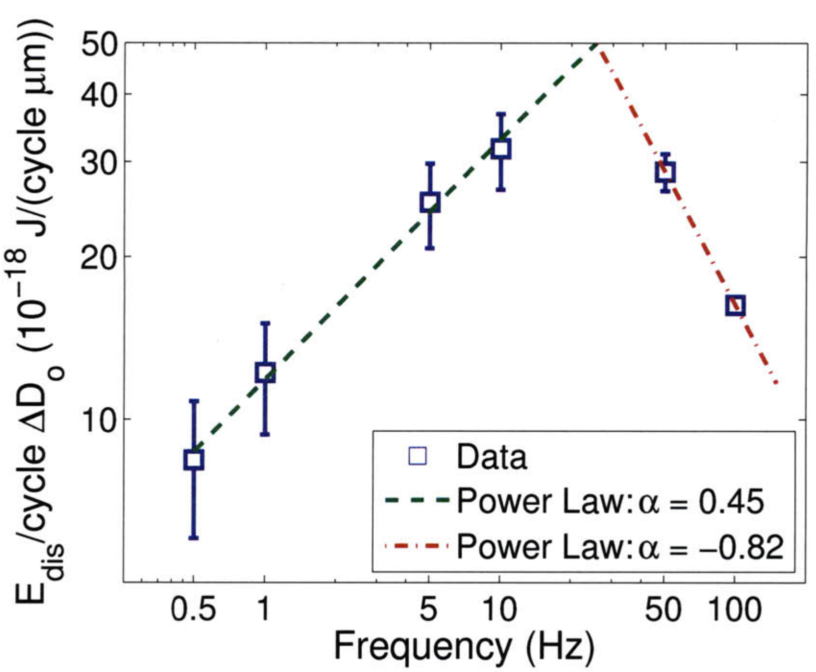

Figure 3-21: Power-law dependence of energy dissipation of healthy RBCs subjected to sinusoidal displacements.

amplitude are outlined in Table 3.4.

Generally speaking, the characteristic loading velocities during sinusoidal load application are comparable to those imparted in the foregoing stress relaxation experiments. Therefore, the apparent discrepancy between the stress relaxation behavior described above and cyclical loading behavior described here might be at least partially explained by a time-dependent reorganization of the spectrin network. Given adequate time, the deformed spectrin network dissipates energy in its reorganization

Amplitude (μm)	Freq. (Hz)	Max. Vel ($\mu m/s$)	Avg. Vel ($\mu m/s$)
1.5	0.5	1.5	2.36
1.5	1.0	3.0	4.71
1.5	5	15	23.56
1.5	10	30	47.124
0.75	50	75	117.81
0.75	100	150	235.62

Table 3.4: Corresponding average and maximum velocities imparted by sinusoidal displacements of given amplitudes and frequencies.

and correlated stress relaxation. Whereas, in the case of periodic loading, the applied is not maintained sufficiently long enough to drive this reorganization, thus reducing the average amount of energy dissipated per cycle. Admittedly, this description is somewhat analogous to mechanical models of viscoelasticity such as those historically described by Hochmouth and Evans and discussed previously. In those models, under high enough loading rates, the dissipative elements (i.e. dashpots) "short out" and result in an apparently elastic response. However, as established in the foregoing results and discussion, if such models are going to be capable of describing the RBC behavior over a wide-range of deformation rates, they require multiple dissipative elements and time-scales. The observed periodic loading behavior may also give evidence of the fluidization of the spectrin network. Fluidization of the RBC spectrin network has been discussed and analyzed in the context of computational models, such as that presented by Li et. al [59]. Under large shear strains and high strain rates (engineering shear strains 0.8-1 and strain rates $\sim 10^5 1/s$), the spectrin network undergoes a solid to fluid transition, resulting in an apparent softening of the stress-strain response. An analagous behavior appears to be present in the force-displacement behavior of Figure 3-19, where, at the largest frequency examined, 100Hz, the energy dissipation is minimal and the force-displacement response is much "softer" than in lower frequencies. This behavior is clearer when examining the force-displacement characteristics at different frequencies on the same axes, as shown in Figure 3-22. Such fluidization has not been observed experimentally in previous experiments. However, the techniques presented here may allow such observations as they enable the application of large shear strains and stresses at frequencies previously unexplored. Future work should be aimed at further exploring this possibility of fluidization, as well as the governing energetics of these deformations. Most notably, temperature-dependence and the possible presence of a metabolic dependence of these behaviors (i.e. ATP-mediated deformation and dissipation behavior) my be explored to further understand these dissipative phenomenon.

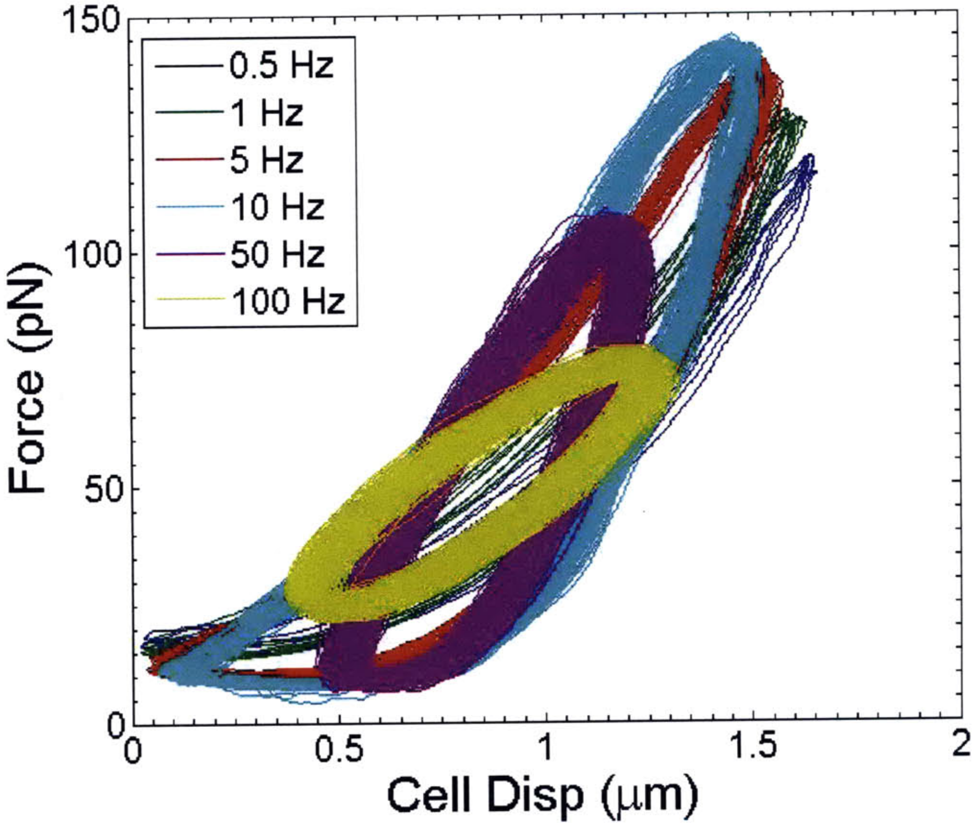

Figure 3-22: Typical load-displacement behavior of a healthy RBC subjected to sinusoidal displacements of varying frequency plotted on the same axes. The change in average slope at 100Hz indicates a softening of the response that may be a result of fluidization of the RBC membrane.

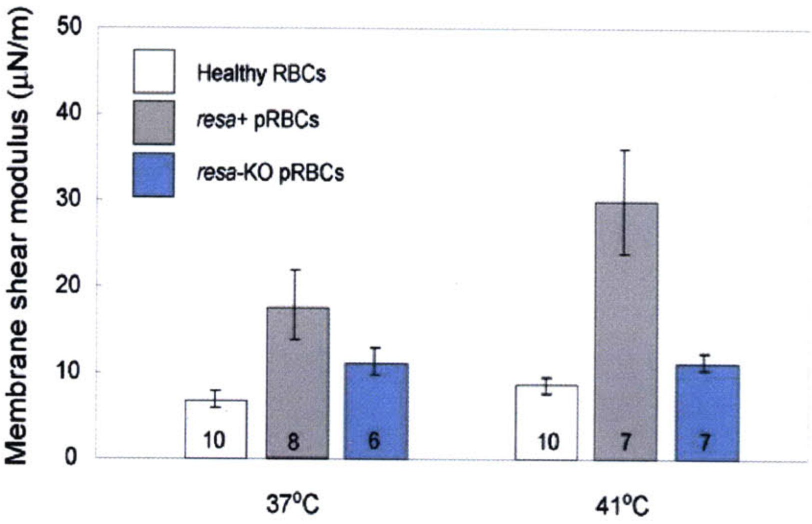

Figure 3-23: Effect of physiological temperature on the membrane shear modulus of uninfected/parasite-free RBCs, RBCs parasitized with the wild-type condition in the production of RESA (resa-WT) and RBCs parasitized with genically modified parsites incapable of producing RESA (resa-KO). Figure adapted with permission from [66, 67].

3.3.2 Characterization of *P.f.* parasitized RBCs

The optical trapping system implemented as part of this thesis work was used by Mills et. al. in the investigation of the role of a particular protein, the ring-infected surface antigen (RESA), in the reduced deformability present in the Ring stage (0-24hrs) of the parasitic cycle. The results of that study is reproduced, with permission, in Figure 3-23 [67]. These results will be further referenced in Chapter 4. Of particular significance in this work is the role of physiological temperatures on the reduced deformability of parasitized Ring stage cells with RESA present. In normal body and, even more significantly, febrile temperatures, the shear modulus of the parastiized RBC is approximately three and six times that of the healthy or uninfected RBC. The implications for such stiffening behavior on the flow behavior of the parasitized vs. healthy RBCs is discussed in Chapter 4. Future work should also aim to quantify the role of RESA on the viscous behavior of the RBC membrane using the techniques described above.

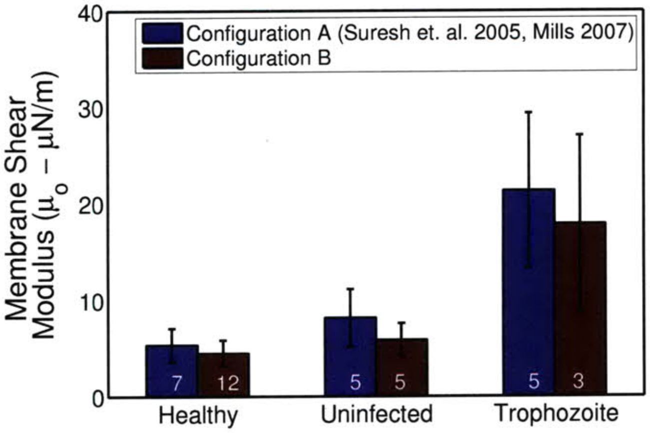

Figure 3-24: Comparison of membrane shear modulus mesurements of late-stage (trophozoite) infected cells measured using Configuration B with measurements made using Configuration A.

One of the particular advantages of the loading configuration developed as part of this thesis work is its potential applicability to investigating cells with enhanced cytoadhesion, such as those seen in the latest stages (Trophozoite and Schizont) of the parasitic cycle of *P.f.* malaria. As shown in Figure 3-24, the loading and analysis scheme presented in this thesis work yields similar results for parasitized cells to those presented by Mills et. al [66, 102]. In principle, this combination of loading configuration and interpretation via a non-dimensionalized FEA study represents a framework by which the mechanical properties of other adherent cells might be explored.

Finally, as prelude to future work on the characterization of parasitized cells, the periodic loading response of trophozoite-stage infected cells was also examined. As shown in Figure 3-25, the infected cells exhibit a slightly larger characteristic energy dissipation under low loading frequencies. However, at larger loading frequencies, the behavior of infected cells is comparable to healthy RBCs. While the data-sets are not large enough to produce a statistically-significant result, they do suggest the possibility of a parasite-mediated viscous response in conjunction with the well-established increase in membrane stiffness. As with healthy RBCs, under sufficient loading frequencies, this viscous dissipation may be reduced by the presence of a time-dependent reorganization response and/or membrane fluidization. As with healthy

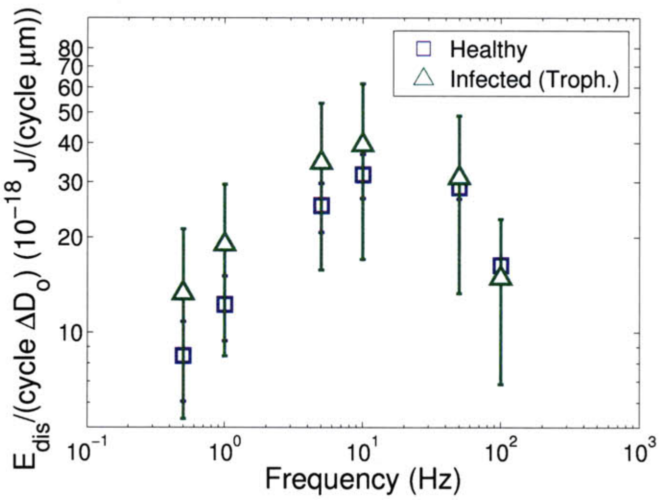

Figure 3-25: Energy dissipation characteristics of healthy vs. infected (trophozoite stage) cells subjected to sinusoidal, periodic loading from $0.5Hz - 100Hz$.

RBCs, the influence of temperature and ATP are two areas that might be of particular interest in further exploring this phenomenon.

3.4 Conclusion

An advanced optical trapping system was developed to investigate the quasistatic (ie purely elastic) and dynamic (ie viscoelastic) response of healthy and diseased human red blood cells. Using a combination of laser-based detection schemes this system has the ability to continuously monitor force and displacement applied to an RBC membrane in order to determine its mechanical properties and dissipative characteristics. The elastic properties of the RBC membrane are inferred from the measured load-displacement characteristics using a system of non-dimensional equations derived from a parametric finite element study. In exploring the dynamic response of RBC membranes, a new loading configuration was developed in which the RBC is firmly adhered to a glass coverslip and loaded via relative motions of a high resolution, closed-loop controlled piezo stage. This loading configuration was used in the development of two techniques to charcterize the large deformation, time and frequency dependent behavior of the RBC membrane. The first technique, time dependent stress-relaxation of the RBC membrane subjected to displacement rates ranging three orders of magnitude ($1 - 100\mu m/s$), revealed that there does not exist a single viscous time-scale capable of describing the dissipative nature of the RBC membrane. Instead, a power-law dependence on energy dissipation was found. These results are in-line with other studies done at smaller loads and deformation rates. However, when subject to periodic, sinusoidal loading of frequencies (0.5-100Hz), such power-law descriptions break-down at high frequencies (greater than 50Hz). These results, which represent the most extensive combination of large deformations and dynamic range applied to the human RBC in an optical-tweezers system, suggest the possible presence of either cytoskeletal reorganization processes or fluidization of the spectrin network at large frequencies and strain levels.

The optical trap system developed here was used by Mills et. al. to establish a strongly temperature-dependent role of the parasitic protein, RESA in the reduced deformability observed in the Ring stage of *P.f.* malaria. Initial results on trophozoite stage parasites using the loading configuration developed in this work suggest the applicability of this configuration to the characterization of late-stage, adherent cells and a potential role of the parasite in increasing the viscous behavior of the parasitized RBC membrane. In addition to further examination of the temperature-dependent, viscous behavior of parasitized RBCs, the ATP-mediated response of healthy and infected RBCs is identified as a near-term avenue for future work in understanding the underlying mechanisms governing the responses measured using these new techniques.

Chapter 4

Flow Dynamics of Healthy and Malaria Infected Human Red Blood Cells in Microfluidic Systems

Much of this chapter was reproduced from [87].

4.1 Introduction

While single-cell, quasistatic assays have helped establish connections between the biophysical characteristics of RBC and disease states [102], they do not adequately capture the reality of various biorheological events associated with the flow of a population of RBCs through the microvasculature. It has also not been feasible thus far to develop *in-vivo* characterization of blood flow in the regions of largest RBC deformation due to the small length scales and geometric complexity of the microvasculature.. To overcome this limitation, *in-vitro* assays of RBC flow through glass tubes [14, 50] and microfabricated fluidic structures made of glass, silicon or polydimethylsiloxane (PDMS) have been developed [3, 48, 97, 99, 107, 17]. These experiments have also been complemented with computations and simulations of RBC biorheology [94, 92, 34, 27, 10, 74, 22, 82].

Despite these advances, there is virtually no experimental quantification to date of flow characteristics (e.g., pressure difference versus cell velocity) of RBCs through constrictions of the smallest relevant length scales (approx. 3 μm in diameter) whereby the dynamics of RBC deformation characteristic of the conditions in the microvasculature can be simulated and visualized. In a few isolated studies where RBC flow has been studied through small channels [97, 99, 98], the dynamics of flow has not been quantified or analyzed so as to facilitate broad conclusions to be extracted or to help facilitate the development of general computational models. Attempts to quantify RBC dynamics to date have not involved realistic *in vivo* temperature conditions [1, 41]. Furthermore, to date no detailed, three-dimensional (3D), quantitative simulations, validated by experiments, of RBC flow through microfluidic systems have been reported. Such simulations are essential to: (a) develop an understanding of the relevant mechanisms and sensitivities of RBC flow behavior (e.g. the effect of RBC membrane viscosity on resistance) that cannot be systematically probed through experiments alone, (b) quantify the dynamics, rheology and interactions of RBCs with the plasma, (c) extract biophysical and rheological properties of RBCs, and (d) develop robust models that can be used for *in vivo* predictions. The insight gained from a systematic combination of simulations and experiments could also be used in the design of novel microfluidic systems and in the interpretation of the role of mechanical and rheological cell properties in disease pathologies.

This chapter presents the results of a combined computational and experimental framework aimed at satisfying the need for quantitative, temperature-dependent characterizations of RBC flow at the smallest relevant length scales. The experimental approach centers on quantifyinng the flow behavior of healthy and parasitized RBCs through microfluidic channels with characteristic length scales down to $3\mu m$. The results of these experiments are used to validate a three-dimensional, computational model of RBC flow using dissipative particle dynamics (DPD). The DPD model formulation was the work of collaborators in this thesis author's research group and thus, the author does not claim its development alone as a contribution of this thesis work. However, as outlined above, this combined experimental/modeling approach represents an important framework by which further insight may be gained regarding the flow of healthy and diseased human RBCs in the microvasculature.

4.2 Materials and Methods

4.2.1 Microfluidic channel fabrication and experimental procedures

PDMS-based microfluidic channels were fabricated using a replica molding process, sometimes termed "soft lithography," that is well reviewed in the literature [108, 111]. The master mold is made from SU8 resist using a two mask, two layer process. The first layer defined the region of primary interest in the flow characterization experiments (described below) and the second layer was used to define large reservoirs for input/output ports and easier interfacing with buffer and cell solutions.

The channel structures and pressure-control system used in this work are illustrated in Figure 4-1. At their narrowest point, channels were 30 μ m long, 2.7 μm high and had widths ranging from 3-6 μm. A sharply converging/diverging structure was used to ensure that it was possible to observe nearly the entire traversal process (channel entrance deformation, channel flow and channel exit behavior/shape recovery) at the imaging magnifications used, typically 20X - 50X. In this way, the use of a single channel structure ensured that the hydrodynamics of the experiment was well-controlled and more easily understood. In addition, this approach reduced the physical domain of the experiment so as to allow for a small modeling domain and decrease the computational time required in the evaluation of our modeling approach.

In the pressure-control system, adapted from [115], a set of dual input and output ports are utilized in order to allow for periodic exchanges of buffer and priming solutions as well as fresh cell solutions. The applied pressure difference was achieved using a combination of pressurized reservoirs and hydrostatic pressure adjustments. The pressure regulators (Proportion Air Inc., McCordsville, IN) utilized a computer-

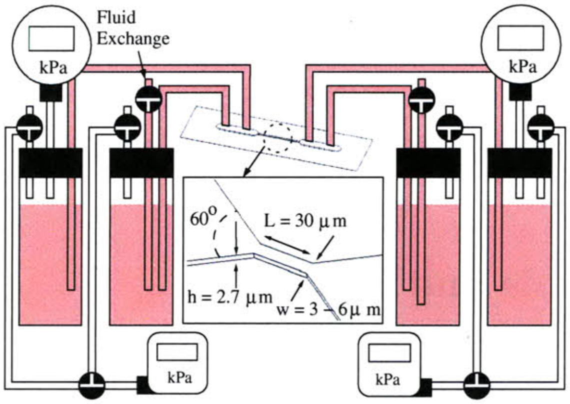

Figure 4-1: Schematic view of pressure-control flow system and channels used in flow experiments. A combination of pneumatic regulators and relative height adjustments are used to set the desired pressure differential.

controlled high-resolution solenoid valve and had a range of 0-207 kPa with an applied pressure resolution of approximately 69 Pa (0.01psi). These regulators exhibited the best response and linearity at pressure levels above 20.7 kPa. Therefore, this was the minimum pressure level applied at the entrance and exit reservoirs. Applied pressure differences were first set by increasing the regulator pressure above this minimum level. Additional hydrostatic pressure adjustments were made by adjusting the relative heights of the pressure columns using a micrometer stage, giving an applied pressure difference resolution of approximately 1 mmH_2O (0.001 psi or 9.8 Pa). A secondary set of pressure gages was used to check the applied pressure difference at the fluid reservoirs in order to ensure there were no significant leaks in the pressure lines leading up to the fluid reservoirs.

Experiments at 37°C and 41°C were carried out using a water bath system in which the channel was bonded into an aluminum dish using a PDMS seal or a parafilm gasket. Pre-heated water was then added to the reservoir to bring the system to the desired temperature. This temperature was maintained by a temperature control system using a flexible heater to radially heat the water bath, a T-type thermocouple temperature probe, and a proportional - integral - derivative (PID) temperature controller (Omega Inc., Stamford, CT). Temperature at the coverslip surface was monitored throughout the experiments using a T-type thermocouple. The use of such a water-bath system ensured that the entire device, including the input and output tubing containing the cells under examination, was maintained at the same temperature. In addition, the high thermal mass of the water-bath system ensured temperature stability for the duration of a typical experiment (1 - 4 h).

During a typical experiment, the channel system was first primed with a 1%wt solution of Pluronic F-108 surfactant (Sigma Inc., St. Louis, MO), suspended in PBS (1X). The enhanced wetting properties of the Pluronic solution allows for easy filling of the channel and purging of air bubbles. After the channel is filled, the Pluronic is allowed to incubate for a minimum of 20 minutes in order to block the PDMS and glass surfaces from further hydrophobic and other non-specific adhesive interactions with the red cell membrane. After this incubation time, the system is flushed with a 1%wt BSA/RPMI buffer solution. The excess buffer is then removed from the entrance reservoir and the cell solution is added and introduced to the channel reservoir area. After an initial flow of cells across the channel is observed (typically by applying a pressure difference of approximately 0.7 kPa (0.1 psi)), the applied pressure difference is set to zero by first equilibrating the applied pressure from the pressure regulators and then stagnating the flow in the channel by trapping a bead in the center of the channel via relative height (i.e. hydrostatic pressure) adjustments. After this process, pressure differences are typically set using the electronically-controlled pressure regulators. However, due to hydrodynamic losses, this applied up-stream and down-stream pressure difference does not correspond to the local pressure difference across the channel. In order to determine this local pressure difference, bead trajectories and velocities are measured using our high speed imaging capabilities and an image processing routine. These measured velocities are used to determine the local pressure difference using a combination of computational fluid dynamics simulations and well-known analytical solutions for flow in rectangular ducts [71]. The details of this procedure are provided below.

Flow experiments were performed on a Zeiss Axiovert 200 inverted microscope (Carl Zeiss Inc. Thornwood, NY) using a halogen source and either a 20X or 40X objective. The microscope objective used for imaging was not a contact objective (e.g., not an oil or water-imersion objective), in order to ensure that the cover slip was sufficiently thermally isolated for experiments at elevated temperatures. Images were recorded on a PCO.1200hs high-speed, CMOS camera, operated at typical frame-rates of 1000-2000 fps (Cooke Corp., Romulus, MI).

4.2.2 Local pressure differential measurement

Across several experimental runs, differences in hydrodynamic pressure losses may arise due to several factors, such as minor leaks, the presence of debris in the channel reservoirs, and cell concentration gradients. Such variability would result in differences in cell traversal/flow behavior under the same nominally applied upstream/downstream pressure differences. Therefore, in order to minimize the effect of these variations as well as minimize the physical domain required in our DPD simulations, a particle tracking scheme was used to experimentally determine the local pressure gradients in the microfluidic channel.

Viscous flow of a Newtonian fluid with viscosity (η) through a channel of rectangular cross-section with width (w), height (h) and length (L) may be described by the well-known pressure-velocity relationship [71]:

$$V(x,y) = \frac{\Delta P}{\eta L}\frac{4h^2}{\pi^3}\sum_{n=1,3,5,\ldots}^{\infty}\frac{1}{n^3}\left(1 - \frac{\cosh(n\pi x/h)}{\cosh(n\pi w/2h)}\right)\sin(n\pi y/h) \tag{4.1}$$

where $-w/2 \leq x \leq w/2$ and $0 \leq y \leq h$. Neutrally-buoyant, rigid particles with a diameter (D_p) that is small compared to the length and width of the channel ($D_p << w$ and $D_p << h$) may be expected to flow along streamlines and give a direct measurement of the fluid velocity at a point corresponding to the center of the particle. Thus, a measured average fluid velocity may be used to infer a pressure difference from an integrated/averaged form of Equation 4.1. However, due to imaging limitations and the small channel dimensions used in this work, we are required to use minimum particle diameters of $1\mu m$, which is comparable to both the channel height and width. In this case, the particle may be expected to travel with a velocity comparable to the average fluid velocity over the projected area of the particle. In addition, the particle may not perfectly track the fluid streamlines due to rotational effects brought upon by the high velocity gradients in the length or width direction. Therefore, in order to establish a relationship between the measured bead trajectories and the local pressure gradient, a combination of numerical averaging and computational fluid dynamics studies (CFD) was used. First, it is important to realize that bead trajectories are limited to the region: $-w/2 + D_p/2 \leq x \leq w/2 - D_p/2$ and $D_p/2 \leq y \leq h - D_p/2$. Over this region, a grid of points with coordinates (x_b, y_b) and separation $(\delta x,\delta y)$ may be selected for which the velocity of the beads at those points may be approximated by the average fluid velocity of the circular region of radius $R_p = D_p/2$ around that point. These bead velocities may be averaged over the bead flow region to establish a relationship between the average bead velocity and the local pressure difference. This relationship is plotted for the channels and temperatures used in our experiments in Figure 4-2. In calculating these relationships, the fluid is assumed to have the same temperature-dependent viscous properties as water [113, 73, 20]. This relationship was compared to the results of a series of CFD simulations of a flow of 1 μm particles in a 2.7 μm high x 4 μm wide channel. These CFD results indicated that for flow off the centerline of the channel, rotational effects are present and beads do not exactly travel along the fluid streamlines. However, as shown in Figure 4-3, these effects have only a small effect on the bead's average velocity in the microfluidic channel compared to that calculated using the local average of 4.1. Therefore, the relationships presented in Figure 4-2 are believed to be adequate for inferring the local pressure gradient for a measured average bead velocity.

In our experiments, the minimum depth of field of our imaging system was estimated to be 2.8 μm using the analysis presented in [64]. Thus, bead images are believed to be taken along the entire channel height. These bead trajectories were tracked and subsequently analyzed using an image segmentation and tracking routine written in Matlab. Average velocity measurements were checked by manually tracking a subset of beads from every data-set. The average bead velocity is then translated to a local pressure differential using the relationships presented in Figure 4-2.

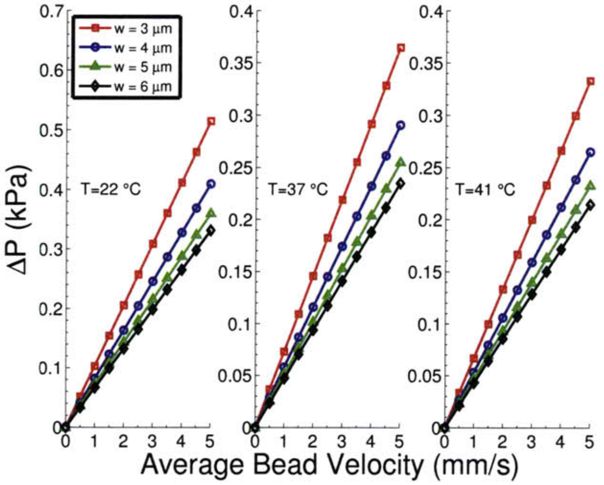

Figure 4-2: Relationship between average velocities of $1\mu m$ diameter beads and local pressure difference at room, body and febrile temperatures (22°C, 37°C and 41°C, respectively) for 2.7 μm high, 30 μm long channels of varying width.

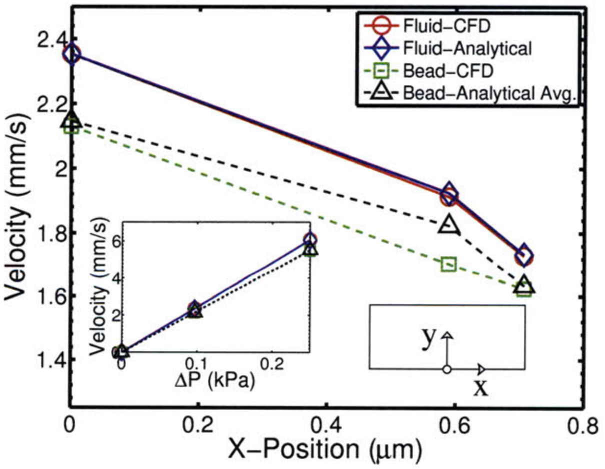

Figure 4-3: Comparison of analytical solutions and CFD results for fluid and bead velocities at various positions along the width of the channel. (Inset: Pressure-velocity relationship for beads and fluid along channel center-line)

4.2.3 Buffer and cell solution preparation

Whole blood from healthy donors was obtained from an outside supplier (Research Blood Components, Brighton, MA). Blood was collected in plastic tubing with an ACD preservative added during collection. Upon reception, blood was stored at 4°C. All experiments were performed within 12 hours of acquiring blood samples.

The primary buffer used in all cell solution preparations and experiments was RPMI 1640 with 1 %wt of Bovine Serum Albumin (BSA) (pH=7.4). 100 μL of whole blood is suspended in 1 mL of this buffer and centrifuged three times at 1000rpm. After the final centrifugation, red cells are suspended in 10 mL of BSA/RPMI buffer, resulting in a final hematocrit of approximately 0.4-0.5%. Finally, immediately prior to introduction into the microfluidic channels, 20-30 μL (5%wt) of 1 μm polystyrene beads (Polysciences Inc., Warrington, PA) were added to the cell solution. If necessary, fresh cell/bead solutions were periodically introduced over the course of a flow experiment. For all cell solutions, no more than 2 hrs. elapsed from the time of its final centrifugation to the time of its flow characterization.

Experiments on *P.f.* parasitized cells were done using the same cell concentrations and the same final buffer suspensions as healthy cells. Parasite cultures were maintained by a collaborator within this thesis author's research group (Dr. M. Diez-Silva). The details of the culture protocol as well as the genetic modification routines are found in [67].

4.2.4 Dissipative particle dynamics (DPD) modeling

We use high-speed imaging to measure and quantify the temperature-dependent flow characteristics (pressure versus velocity relationships) and shape transitions of RBCs as they traverse microfluidic channels of varying characteristic diameters. These results are compared to simulated flow behavior using Dissipative Particle Dynamics (DPD). DPD is a mesoscopic approach whereby both fluid and solid elements of a fluid-solid media are discretized as a collection of points. The interaction between points and amongst different domains are governed by a collection of pairwise interaction potentials and a combination of conservative and dissipative forces [52]. The DPD model formulation and execution presented in thesis is the work of a collaborator in the thesis author's research group (Dr. Igor Pivkin). Details on this particular formulation are provided in [80, 79, 78, 87].

However, it is important to note that an important feature of our modeling approach compared to other mesocopic approaches is that the interaction parameters governing the elastic behavior of the RBC membrane are derived from the properties of the individual components of the RBC cytoskeleton. Therefore, the model is capable of capturing the elastic behavior of the RBC without the need for additional fitting parameters. The viscous parameters are defined using additional independent experimental measurements. As a result, the RBC model accurately matches the behavior measured in three different experiments at both room and physiological temperatures: (1) the force-displacement response as measured with optical tweezers [79], (2) the magnitude of resting membrane thermal fluctuations [75], and (3) the characteristic time scale of membrane relaxation following stretching, such as that presented in Figure 3-11 and [39, 68]. The membrane and fluid parameters determined from this diverse combination of experiments are applied for all subsequent modeling conditions and are complemented with the results of a single data point from our RBC flow experiments in order to translate non-dimensional simulation results to physical units.

4.3 Results and Discussion

4.3.1 Flow characterization of healthy RBCs

Figure 4-4 presents shape profiles of the RBC as it traverses channels that are 2.7 μm high, 30 μm long and 3 to 6 μm wide, geometries typical of some of the large deformation conditions in the microvasculature. Figure 4-4(a) presents a qualitative comparison of experiment with our DPD model for RBC traversal across a 4 μm wide channel. Three time scales can be identified: (Frames 1-2) the time required for the

the cell to go from its undeformed state to being completely deformed in the channel, (Frames 2-3) the time it takes the cell to traverse the channel length, and (Frames 3-4) the time for complete egress from the channel. Here the cell undergoes a severe shape transition from its normal biconcave shape to an ellipsoidal shape with a longitudinal axis up to 200% of the average, undeformed diameter. Figure 4-4(b) illustrates how the longitudinal axis of the cell, measured at the center of the channel, changes with different channel widths. Experimental and simulated longitudinal axes typically differ no more than 10-15%. During such large deformation, the RBC membrane surface area and volume are assumed to be constant in our DPD model. However, the model allows for local area changes during passage through the channel. The contours presented in Figure 4-4(c) show the evolution of such local gradients in area expansion. These results indicate that, for the smallest length scales, the leading edge of the cell deforms significantly as the cell enters the constriction and deforms further as the cell traverses the channel. As expected, little area expansion is seen during flow through the 2.7 μm high x 6 μm wide channel. The local stretch of the underlying spectrin network scales with the square root of local area expansion. Therefore, this information may be used to estimate the maximum stretch of the spectrin network at any point during this traversal process. This result is shown in Figure 4-4(d) for the channel widths used in the experiments. At the smallest width channels, the maximum stretch increases to $\lambda \geq 1.6$.

In Figure 4-4(e) we compare these shape characteristics to the results of other meso-scale modeling approaches, such as the multiparticle collision dynamics (MPC) models presented by McWhirter et. al. [63]. Here, the deviation of the RBC shape from that of a sphere is quantified by its average asphericity $< \alpha >$, where $< \alpha >= 0$ for a sphere and $< \alpha >= 0.15$ for an undeformed discocyte. In larger vessels, the asphericity approaches 0.05 as the cell assumes its well-known parachute-like shape [63]. Our DPD scheme, when used to model flow in larger vessels, indicates a similar trend as shown in Figure 4-4(e). However, in the narrowly constricted channels, the average asphericity increases significantly greater than previously known. Thus, our computational model is capable of capturing a range of shape deviations in large and

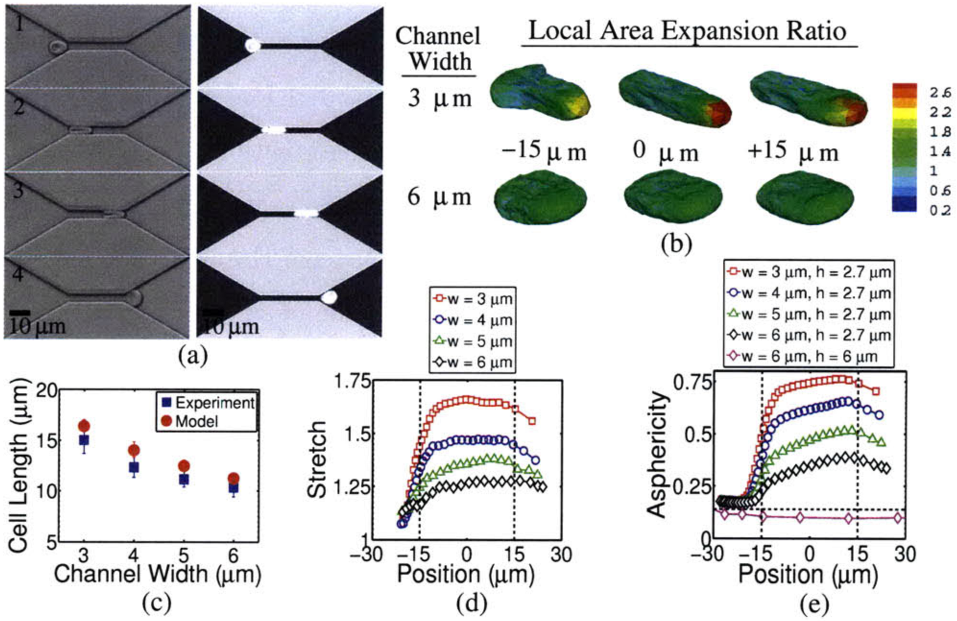

Figure 4-4: Shape characteristics of RBC traversal across microfluidic channels: (a) Experimental (left) and simulated (right) images of erythrocyte traversal across a 4 μm wide, 30 μm long, 2.7 μm high channel at 22°C and an applied pressure difference of $0.085 kPa$.; (b) local area expansion contours for an RBC traversing a 3 μm and 6 μm wide (h = 2.7 μm) channel under ΔP = 0.085 kPa; (c) measured and simulated cell lengths at the center of the microfluidic channel for varying channel widths; (d) estimated maximum stretch ratios of RBC spectrin network; and (e) asphericity index as the cell passes through different channel widths under $\Delta P = 0.085$ kPa. In (d) all channel heights are 2.7 μm. In (e), channel height and width dimensions are indicated. Vertical dashed lines in (d) and (e) indicate locations of channel entrance and exit. Horizontal dashed line in (e) indicates the stress-free, resting asphericity of a normal RBC ($\alpha = 0.15$).

small vessels, which correlate well with experimental measurements for the smallest length scales.

Figure 4-5(a) presents pressure–velocity relationships for RBC flow across channels of different cross-sectional dimensions. Average cell velocity measurements are taken between the point just prior to the channel entrance (the first frame in Figure 4-4(a)) and the point at which the cell exits the channel (the final frame in Figure 4-4). As such, the time scale examined in these studies is a combination of entrance times, traversal and exit times. These individual time scales are plotted Figure 4-5(b).

The DPD model adequately captures the scaling of flow velocity with average pressure difference for 4–6 μm wide channels. The significant overlap in the experimental data for 5–6 μm wide channels can be attributed largely to variations in cell size and small variations in channel geometry introduced during their microfabrication. The relative effects of these variations are the subject of a sensitivity study we present in Figure 4-6; the variations are illustrated here as error bars on DPD simulation results for select cases. For the smallest channel width of 3 μm, the experimentally measured velocities are as much as half that predicted by the model. This may be attributed to several factors, including non-specific adhesive interactions between the cell membrane and the channel wall due to increased contact. Furthermore, this 3 μm x 2.7 μm (8.1 μm^2) cross-section approaches the theoretical 2.8 μm diameter (6.16 μm^2) limit for RBC transit of axisymetric pores [19]. Therefore, very small variations in channel height (due, for example, to channel swelling/shrinking due to small variations in temperature and humidity) can have significant effects. Thus, this geometry may be taken as a practical limit of the current modeling scheme for the chosen level of discretization (500 "coarse-grained" nodes, see [79]). In addition, while the total traversal time scales are in close agreement, the data presented in Figure 4-5(b) indicates that the DPD model typically over-predicts the relative amount of time the cell requires to enter the channel constriction. This can be attributed in part to the use of periodic inlet/outlet boundary conditions, which do not allow for an accurate characterization of the fluid momentum. This is clear when examining the sensitivity of the simulated time scales to the size of the modeling domain. Doubling the domain

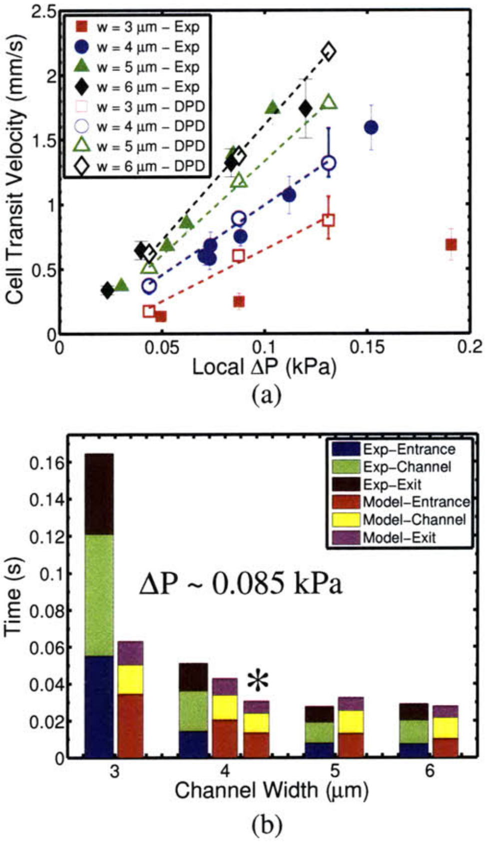

Figure 4-5: Quantitive flow behaviors of RBC traversal of microfluidic channels. (a) Comparison of DPD simulation results (open markers) with experimentally measured mean velocities (filled markers) of RBC traversal as a function of measured local pressure differences for 3, 4, 5 and $6\mu m$ channel widths (height = 2.7 μm, length = 30 μm). Error bars on experimental data points represent an average ± one standard deviation of a minimum of 18 cells. Error bars on modeling data points indicate minimum and maximum variations resulting from a case study exploring the sensitivity of the RBC traversal to channel geometry and cell volume, shown in Figure 4-6. (b) Experimentally measured and modeled total transit time broken into entrance, channel and exit components for RBC traversal across varying channel widths under $\Delta P = 0.085$ kPa. (*) Modeling results with 2X domain size to examine the role of fluid inertia and periodic boundary conditions.

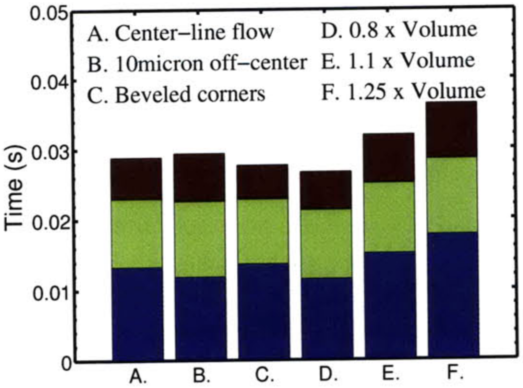

Figure 4-6: Case studies using the DPD model to evaluate the sensitivity of RBC flow in a 4 μm wide x 2.7 μm high channel subjected to a pressure difference of 0.14 kPa with respect to geometric variations in flow direction (B: Off-centerline flow), channel geometry (C: Non-rectangular, beveled corner cross section with the same cross-sectional area), and cell volume (D,E,F: 0.8, 1.1, and 1.25 times the standard cell volume of 100 μm^3, respectively).

size (results noted in Figure 4-5(b)), effectively increases the momentum of the fluid and cell as the cell enters the channel, and results in a decrease in characteristic *entrance* time, but has little effect on the transit and exit time. It is also possible that there is a physical basis for this discrepancy between relative contributions of the cell entrance time. For example, at such high rates of deformation (up to 200% overall stretch in approximately 0.2 seconds), the RBC might undergo an active reorganization of its spectrin network. Any such molecular reorganization is not accounted for in our model, but could be introduced.

Some additional features of the experimental results and modeling predictions should be highlighted. First, the velocities in Figure 4-5(a) compare well to experimental measurements made across 5 μm and 6 μm axisymmetric pores by Frank and Hochmuth [41] as well as aggregate measurements made by Sutton et. al [103] in a microfluidic device where control of flow pressure was less robust than in the present case. Also, as in these and other *in-vitro* experiments, the flow resistance in our experiments are significantly smaller than those measured *in-vivo* at smaller characteristic diameters, which would typically result in significantly larger flow resistance [112, 83]. This is most likely due to the lack of a glycocalyx layer in these *in-vitro* experiments, which has been hypothesized to increase the flow resistance of the microcirculation *in vivo* by as much as ten times that of *in-vitro* experiments of comparable length scales [112, 83, 93].

Our experimental and modeling results are also compared to the predictions [92] from an axisymmetric analysis of RBC passage through micropores. Here pressure differences of 0.1 kPa across 10 μm long pores with diameters ranging from 3.6 μm to 6 μm result in average traversal velocities from approximately 0.2 - 2 mm/s. These velocities are of the same approximate magnitude as those presented here. However, when the analysis in [92] of 5 μm and 6 μm tube traversals are compared to the experimental results of Frank and Hochmuth, it consistently over-predicts the traversal velocities by up to a factor of four. This may be due to increased dissipation of the membrane and fluid due to slight asymmetries of the cell and tube that are not captured using an axisymmetric continuum assumption. However, the use of a fully three-dimensional, discrete approach is capable of capturing such asymmetries and giving more robust predictions of RBC flow dynamics at such small length scales.

The effect of temperature on the flow dynamics of the RBC is shown in Figure 4-7(a). Here, we examine the ratio of the local pressure gradient and average cell velocity ($\Delta P/V$) versus temperature for two different channel geometries. We also present the pressure–velocity ratio for a fluid with the properties of the surrounding media as a function of temperature for each of the respective channel geometries. For a given channel geometry, $\Delta P/V$ scales with the effective viscosity of the medium (external fluid, cell membrane and internal fluid) and the membrane stiffness. Over this temperature range (22°C-41°C), quasi-static experiments reveal essentially no effect of temperature on the stiffness of healthy RBCs [109, 67]. Here, the observed temperature dependence is ascribed to changes in viscosity in that decreased flow resistance (i.e. increased average cell velocities) results from increasing temperature due to a decrease in the effective viscosity of the medium (the combination of external fluid, internal fluid and membrane). As discussed in Chapter 3, under a standard linear solid model, optical trapping measurements have shown that the RBC membrane viscosity at 37°C is 50% of its value at room temperature. Similarly, the viscosities

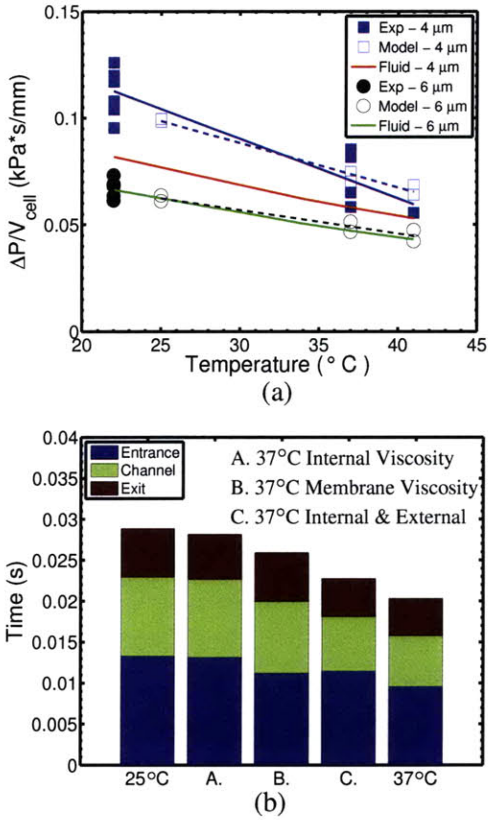

Figure 4-7: Temperature dependent RBC flow behaviors. (a) Comparison of DPD simulation results with experimentally measured effects of temperature on ratio of local pressure difference and mean velocity of erythrocyte traversal in a 4 μm and 6 μm wide (h = 2.7 μm, L = 30 μm) microfluidic channel. Data points represent an average of a minimum of 18 cells. (all $p < 0.05$ in experimental data) (b) Independent effects of external fluid viscosity, membrane viscosity and internal fluid viscosity on the modeled flow characteristics of RBCs in 4 μm channels subjected to a pressure difference of 0.14 kPa.

of the suspending media and internal cytosol decrease by 22% and 27%, respectively. However, the relative influences of the internal fluid, external fluid and membrane appear to be different for flow across 4 μm and 6 μm channels. In the case of RBC flow across 6 μm wide channels, the effective viscosity is nearly equivalent to the surrounding fluid viscosity. However, RBCs flowing across 4 μm wide channels exhibit a markedly larger apparent viscosity, ranging from approximately twice that of the external fluid at room temperature down to 1.3 times at febrile temperatures. Thus, there appears to be a threshold cross section below which, the RBC rheology begins to play a significant role in its dynamic flow behavior. The membrane viscosity is at least 10 times the internal and external components. Therefore, one might expect its influence on the flow behavior of the RBC across such small cross-sections to be relatively larger than the internal and external viscosities [39]. Figure 4-7(b) presents the results of a series of simulations used to determine the relative contributions of the RBC membrane viscosity and its internal and external fluid viscosities for flow across a 4 μm wide channel. It can be seen that, for a 4 μm wide channel, the external fluid and membrane viscosities play an equally significant role in determining the transit behavior of the RBC.

4.3.2 Flow characterization of parasitized RBCs

As discussed in Chapter 2, it has been established that the presence of the parasitic protein RESA is largely responsible for reduced deformability in *P.f.* parasitized RBCs in the Ring stage of parasitic maturation. This reduced deformability is most severe at physiologically normal and febrile temperatures. In order to investigate the effect of such a stiffening behavior in the context of microvascular flow, microfluidic experiments were performed using $4\mu m$ wide channels at room temperature, $37°C$, and $41°C$. In the extreme case, cells were occasionally observed to occlude the channel for long periods of time. However, it is generally believed that these cells are late-Ring or early-Trophozoite stage infected cells. A comparison of the flow behavior of uninfected RBCs and that of the RESA wild-type (WT) and RESA knock-out (KO) infected RBCs is shown in Figure 4-8. This data suggests that all parasitized

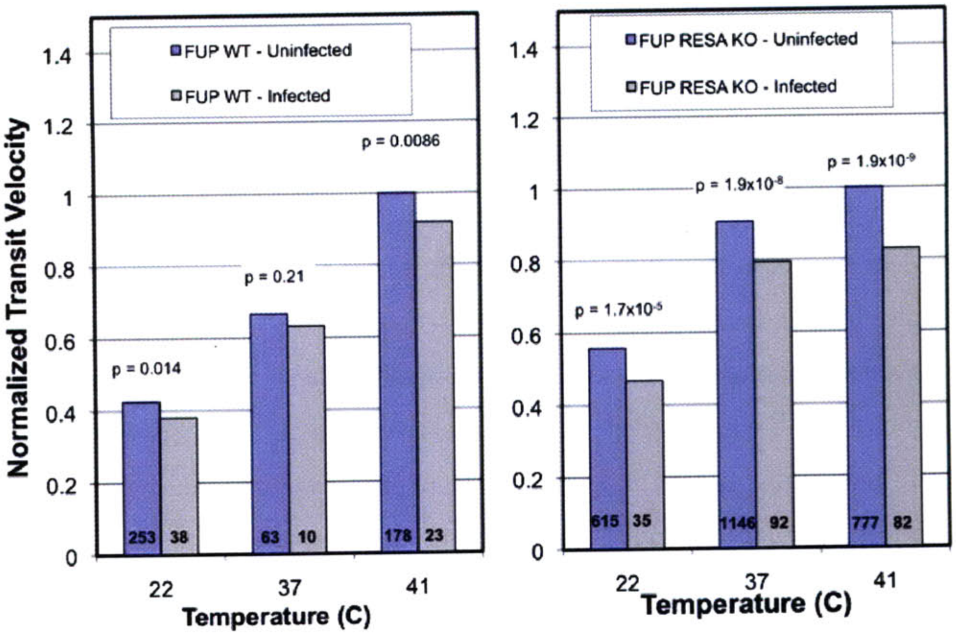

Figure 4-8: Flow behaviors of (a) wild-type (WT) and (b) RESA knock-out (KO) *P.f.* parasitized RBCs in 4 μm wide channels under a pressure difference of approximately $\Delta P = 0.1kPa$. In order to highlight the differences between healthy and infected cells and the variation with temperature, each data set is normalized by the flow velocity of uninfected cells at 41 $^{\circ}C$.

cells, regardless of the presence of RESA, exhibit inhibited flow (i.e. reduced transit velocities) across the channel. There does not appear to be a significant effect of the presence of RESA. As shown in Figure 4-8, the absence of RESA results in parasitized cells whose elastic properties are comparable to healthy cells. Thus, the inhibited flow behavior presented in Figure 4-8 is likely the result of increased dissipation of either the cell membrane or the internal environment. DPD simulations presented in Figure 4-7 suggest that the internal fluid viscosity plays a less-significant role than the membrane viscosity. Therefore, the observed flow inhibition may be a result of increased membrane viscosity due to other parasitic proteins binding to the spectrin network.

As a final note, the work of Bow, when combined with these results, provides additional insight into the role of RESA in microvascular flow [13]. In this work, a microfluidic device with periodic constrictions is used to examine the flow behavior of healthy, uninfected and parasitized cells. The flow velocities in this work are nearly an order of magnitude lower than those measured in this thesis work (0.1mm/s compared to approximately 1mm/s here). Under these conditions, a statistically significant difference between RESA-WT and RESA-KO populations is seen relative to uninfected and healthy cells. This result suggests that the role of RESA is rate-dependent where, at low shear rates, RESA serves to increase over all viscous flow resistance but, under higher shear rates, the effect of RESA is reduced. This would be akin to a plateau in membrane viscosity or a possible shear-thinning behavior, perhaps analogous to the frequency-dependent dissipative behavior discussed in Chapter 3. In order to more fully understand this behavior, future work should be aimed at using the optical trapping techniques presented in Chapter 3 to more explicitly examine the changes in apparent viscosity of parasitized RBCs.

4.4 Conclusion

In this work, we have presented an integrated experimental–computational framework for the quantitative analysis of the flow dynamics of human RBCs in a microfluidic system mimicking smallest dimensions in the microvasculature. In this framework, we develop a 3D computational model using Dissipative Particle Dynamics that accurately reproduces the behavior observed in three different, independent sets of experiments: force-displacement measurements using optical tweezers, membrane relaxation measurements, and membrane thermal fluctuation measurements. The use of this model to simulate the flow behavior of RBCs in microvascular structures is validated using the most quantitative experimental measurements to date of the flow characteristics of individual RBCs in an *in-vitro* system at physiologically relevant temperatures. The model also provides accurate simulations of the RBC shape transitions. In addition, the model is capable of identifying areas of high, non-uniform levels of stretch in the spectrin network during RBC passage through small channels. This information might be used to establish a criterion for hemolysis, which is an important consideration for the design of *in-vitro* diagnostic and blood separation systems as well as heart valves and stents [95].

Experimental investigation of the temperature-dependent flow characteristics (e.g. velocity vs. pressure, and pressure–velocity ratio vs. temperature) indicates that there exists a cross-sectional area threshold above which, the passage of individual RBCs is largely dictated by the properties of the external fluid. However, below this area threshold, the effective viscosity of the RBC and surrounding media is approximately doubled. At physiologically relevant temperatures (37°C and 41°C), this effective viscosity increase is about 30%. This result suggests a strong temperature-dependence of RBC dynamics that is not captured in traditional quasistatic membrane property measurements of healthy RBCs. This temperature-dependence is further investigated to evaluate the role of individual system components (external fluid, internal fluid and RBC membrane) in influencing flow dynamics. Results reveal that the RBC membrane viscosity begins to play an equal or dominant role over the effective RBC flow behavior compared to that of the external fluid below a threshold channel cross-sectional area.

Finally, using the microfluidic system developed, the flow of ring-stage parasitized RBCs were compared to that of uninfected RBCs. It was found that, although parasitized RBCs do exhibit reduced flow velocities, the parasitic protein RESA does not have a significant role on inhibited flow behavior. When taken into consideration with other studies, this result is hypothesized to be due to a rate-dependent effect of RESA on the effective viscosity of the parasitized RBC that is not examined in this study. Future work should be aimed at more explicitly connecting the time and frequency domains examined here or in future studies using a similar approach with the characterizations and constitutive models resulting from the optical trapping techniques described in Chapter 3.

Chapter 5

Summary of Results and Thesis Contributions

The major results and contributions of this thesis work are outlined below:

- An advanced optical trapping system was implemented and used in the characterization of the mechanical properties of healthy and *Plasmodium falciparum* parasitized human Red Blood Cells at room and physiological temperatures. Work done with this system by Mills et. al. revealed a strong temperature-dependent role of the parasitic protein RESA in the reduced deformability of Ring-stage parasitized cells.

- A new loading configuration was developed in order to test the mechanical response of healthy and parasitized RBCs. This development was accompanied by an extensive parametric finite element analysis study in which the range of relevant experimental parameters were explored to determine the force-displacement response of RBCs under the new loading configuration. These results were combined with dimensional analysis to determine a system of non-dimensional equations that may be used to extract the membrane shear moduli of RBCs from experimental measurements of force, displacement and contact conditions. This new loading configuration yielded similar results for the membrane shear modulus of healthy and late stage (trophozoite) parasitized RBCs as other studies, indicating that it may be applied both to healthy RBCs and cell systems exhibiting increased cytoadhesion.

- This new loading configuration was also used in the development of new experiments aimed at characterizing the dynamic response of RBCs. Essential to these experiments was the concurrent development of a novel system to track the position of the piezoelectric stage that serves as the load actuator in these experiments. This system allows for concurrent measurements of force and displacement over a broad range of displacement rates and and sinusoidal frequencies (up to $100\mu m/s$ and $100Hz$, respectively). This combination of dynamic range and force levels exceed any previous investigation of RBC membrane mechanics using optical trapping.

- Stress relaxation experiments on healthy RBCs using this dynamic optical trapping system reveal an "apparent" stiffness increase by a factor of 2 when loading rates increase from $1\mu m/s - 100\mu m/s$. Examining the subsequent relaxation behavior under this range of loading rates reveals that there does not exist a single characteristic viscous time-scale that can be used to describe the relaxation behavior of the RBC. Instead, analysis of the energy dissipation of stress-relaxation cycles suggests that a power law dependence on strain rate may be the most appropriate description of the RBC membrane.

- Periodic loading of the RBC membrane under sinusoidal forcing functions reveal that the power-law description of the viscous membrane characteristics suggested by stress relaxation experiments and by other investigators may not be applicable to the largest loading frequencies (50Hz or greater). Instead, decreasing viscous dissipation is seen at these frequencies, suggesting either a unique time-dependent relaxation spectrum (i.e. a combination of viscous timescales not yet examined) or the potential "fluidization" of the RBC membrane at high frequencies of oscillation.

- A microfluidic system was designed and implemented to characterize the flow behavior of healthy and parasitized RBCs. This system resolves the shortcomings of several previous *in-vitro* experiments in its ability to simultaneously measure pressure differentials and flow velocities at the smallest relevant length-scales (down to $3\mu m$ in characteristic diameter) and physiologically-relevant temperatures.

- A combination of optical trapping measurements and results from this microfluidic system were used in the validation of a three-dimensional computational model based on Dissipative Particle Dynamics. Such a combined experimental-computational framework has not been previously reported for developing mesocsopic approaches to modeling microvascular blood flow.

- The experimental flow characterizations reveal a cross sectional area threshold of approximately $2.7\mu m$ x $4\mu m$ that, below which, the properties of the RBC membrane begin to dominate the flow behavior of the RBC. Flow measurements taken at physiological temperatures reveal that this dependence is due to temperature-dependent viscous effects of the RBC membrane, internal fluid or external fluid environments. DPD simulations suggest that the external fluid and the RBC membrane viscosities are more influential than the internal cytosol/hemoglobin solution.

- Ring-stage parasitized cells uniformly exhibit inhibited flow behavior relative to uninfected cells. However, the role of RESA on this behavior is minimal within the pressure-velocity regime explored here (typical $\Delta P = 0.1kPa$ and $V = 1mm/s$). Parallel work by others, done at an order of magnitude smaller characteristic flow velocities, suggest that the role of RESA in microvascluar-like flow may be rate-dependent and more relevant at smaller pressure-velocity regimes than explored here.

Appendix A

KOH Etch coverslip protocol

(taken, with permission, from [77])

This protocol outlines a method to etch coverslips using KOH.

Reagents:

- Potassium Hydroxide (KOH)
- Ethanol (100%)
- ddH2O (Millipore, Dedon Lab)

Equipment:

- Corning Coverslips, 24 x 60 mm, 1? thickness (Cat No. 12-553-6, Fisher Scientific)
- Teflon racks (custom made)

Procedure:

- Dissolve 100g of KOH in 300 ml of 100% ethanol in a 1 L beaker. Stir with a stir bar until KOH is completely dissolved or for 30 minutes.
- Place coverslips in Teflon racks. Usually we do 6-8 racks per procedure.
- Fill another 1 L beacker with at least 300 ml of 100% ethanol and two additional beakers with at least 300 ml of ddH2O.

- Degas all four beakers (two at a time) in the bath sonicator for 5 min. After degassing, place one of the ddH2O beakers and the KOH beaker in the bath sonicator.
- Submerge one coverslip rack in the KOH solution and sonicate for 5 min.
- Wash coverslips by dipping the rack up and down or spinning it in the ethanol beaker.
- Wash coverslips by dipping the rack up and down or spinning it in the ddH2O beaker.
- Submerge the rack of coverslips in the ddH2O beaker in the sonicator and sonicate for 5 min.
- Spritz coverslips with ddH2O bottle. Do each coverslip side at least twice.
- Spritz coverslips with ethanol bottle. Do each coverslip side at least twice.
- Repeat steps 4-9 for other racks. Note that the ddH2O and KOH beakers in the sonicator can contain coverslip racks during sonication at the same time.
- Dry rack in oven for at least 15 min at 100C. Store coverslips in racks inside sealed containers at room temperature. They last about a week.

Bibliography

[1] M. Abkarian, M. Faivre, and H. A. Stone. High-speed microfluidic differential manometer for cellular-scale hydrodynamics. *Proc Natl Acad Sci USA*, 103:538–542, 2006.

[2] B. Alberts, A. Johnson, J. Lewis, M. Raff, K. Roberts, and P. Walter. *Molecular Biology of the Cell.* 2002.

[3] M. Antia, T. Herricks, and P. K. Rathod. Microfluidic modeling of cell-cell interactions in malaria pathogenesis. *PLoS Path*, 3:939–948, 2007.

[4] D. Appleyard. *Engineering Optical Traps for New Environments and Applications in the Measurement of Biological Adhesives and Motors.* PhD thesis, Massachusetts Institute of Technology, 2008.

[5] M. Arslan and M. C. Boyce. Constitutive modeling of the finite deformation behavior of membranes possessing a triangulated network microstructure. *J Appl Mech-T Asme*, 73:536–543, 2006.

[6] M. Arslan, M. C. Boyce, H. J. Qi, and C. Ortiz. Constitutive modeling of the stress-stretch behavior of two-dimensional triangulated macromolecular networks containing folded domains. *J Appl Mech-T Asme*, 75:011020, 2008.

[7] A. Ashkin. Acceleration and trapping of particles by radiation pressure. *Phys Rev Lett*, 24:156–9, 1970.

[8] A. Ashkin. History of optical trapping and manipulation of small-neutral particle, atoms, and molecules. *Ieee J Sel Top Quant*, 6:841–856, 2000.

[9] A. Ashkin, J. Dziedzic, J. Bjorkholm, and S. Chu. Observation of a single-beam gradient force optical trap for dielectric particles. *Opt Lett*, 11:288–290, 1986.

[10] P. Bagchi, P. C. Johnson, and A. S. Popel. Computational fluid dynamic simulation of aggregation of deformable cells in a shear flow. *J Biomech Eng Trans ASME*, 127:1070–1080, 2005.

[11] R. M. Berne and Levy. *Physiology.* Mosby, St. Louis, 2004.

[12] S. Block, D. Blair, and H. Berg. Compliance of bacterial flagella measured with optical tweezers. *Nature*, 338:514–518, 1989.

[13] H. Bow. *Microfluidic devices for analysis of red blood cell mechanical properties.* Doctorate, Massachusetts Institute of Technology, 2010.

[14] D. Braasch. Red cell deformability and capillary blood flow. *Physiol Rev*, 51:679–701, 1971.

[15] R. Brau. *Exploring the Mechanome with Optical Tweezers and Single Molecule Fluorescence.* PhD thesis, Massachusetts Institute of Technology, 2007.

[16] R. Brau, J. Ferrer, H. Lee, C. Castro, B. Tam, P. Tarsa, P. Matsudaira, M. Boyce, R. Kamm, and M. Lang. Passive and active microrheology with optical tweezers. *J Opt A: Pure Appl Opt*, 9:S103–S112, 2007.

[17] J. P. Brody, Y. Q. Han, R. H. Austin, and M. Bitensky. Deformation and flow of red-blood-cells in a synthetic lattice - evidence for an active cytoskeleton. *Biophys J*, 68:2224–2232, 1995.

[18] P. A. Buffet, G. Milon, V. Brousse, J. M. Correas, B. Dousset, A. Couvelard, R. Kianmanesh, O. Farges, A. Sauvanet, F. Paye, M. N. Ungeheuer, C. Ottone, H. Khun, L. Fiette, G. Guigon, M. Huerre, O. Mercereau-Puijalon, and P. H. David. Ex vivo perfusion of human spleens maintains clearing and processing functions. *Blood*, 107:3745–3752, 2006.

[19] P. B. Canham and A. C. Burton. Distribution of size and shape in populations of normal human red cells. *Circul Res*, 22:405–422, 1968.

[20] A. Chatterjee. Intrinsic viscosity measurements of bovine serum albumin at different temperatures. *Nature*, 205:386, 1965.

[21] S. Chien. Red cell deformability and its relevance to blood flow. *Annu Rev Physiol*, 49:177–192, 1987.

[22] B. Chung, S. Kim, P. C. Johnson, and A. S. Popel. *Comput Methods Biomech Biomed Eng*, 12:385–397, 2009.

[23] B. M. Cooke, F. K. Glenister, N. Mohandas, and R. L. Coppel. Assignment of functional roles to parasite proteins in malaria-infected red blood cells by competitive flow-based adhesion assay. *Br J Haematol*, 117:203–11, 2002.

[24] B. M. Cooke, N. Mohandas, and R. L. Coppel. The malaria-infected red blood cell: structural and functional changes. *Adv Parasitol*, 50:1–86, 2001.

[25] B. M. Cooke, N. Mohandas, and R. L. Coppel. Malaria and the red blood cell membrane. *Semin Hematol*, 41:173–88, 2004.

[26] H. A. Cranston, C. W. Boylan, G. L. Carroll, S. P. Sutera, J. R. Williamson, I. Y. Gluzman, and D. J. Krogstad. Plasmodium falciparum maturation abolishes physiologic red cell deformability. *Science*, 223:400–3, 1984.

[27] E. R. Damiano. The effect of the endothelial-cell glycocalyx on the motion of red blood cells through capillaries. *Microvasc Res*, 55:77–91, 1998.

[28] M. Dao. Mechanics of the human red blood cell deformed by optical tweezers. *Journal of the Mechanics and Physics of Solids*, 51:2259–2280, 2003.

[29] M. Dao, J. Li, and S. Suresh. Molecularly based analysis of deformation of spectrin network and human erythrocyte. *Mat Sci Eng C-Bio S*, 26:1232–1244, 2006.

[30] M. Dao, C. Lim, and S. Suresh. Mechanics of the human red blood cell deformed by optical tweezers [journal of the mechanics and physics of solids, 51 (2003) 2259-2280]. *Journal of the Mechanics and Physics of Solids*, 53:493–494, 2005.

[31] L. Deng, X. Trepat, J. P. Butler, E. Millet, K. G. Morgan, D. A. Weitz, and J. J. Fredberg. Fast and slow dynamics of the cytoskeleton. *Nat Mater*, 5:636–640, 2006.

[32] D. E. Discher, N. Mohandas, and E. A. Evans. Molecular maps of red cell deformation: hidden elasticity and in situ connectivity. *Science*, 266:1032–5, 1994.

[33] G. K. Driessen, T. M. Fischer, C. W. Haest, W. Inhoffen, and H. Schmid-Schönbein. Flow behaviour of rigid red blood cells in the microcirculation. *Int J Microcirc Clin Exp*, 3:197–210, 1984.

[34] C. D. Eggleton and A. S. Popel. Large deformation of red blood cell ghosts in a simple shear flow. *Phys Fluids*, 10:1834, 1998.

[35] H. Engelhardt, H. Gaub, and E. Sackmann. Viscoelastic properties of erythrocyte membranes in high-frequency electric fields. *Nature*, 307:378–80, 1984.

[36] H. Engelhardt and E. Sackmann. On the measurement of shear elastic moduli and viscosities of erythrocyte plasma membranes by transient deformation in high frequency electric fields. *Biophys J*, 54:495–508, 1988.

[37] E. A. Evans. A new material concept for the red cell membrane. *Biophys J*, 13:926–40, 1973.

[38] E. A. Evans. Bending elastic modulus of red blood cell membrane derived from buckling instability in micropipet aspiration tests. *Biophys J*, 43:27–30, 1983.

[39] E. A. Evans and R. M. Hochmuth. Membrane viscoelasticity. *Biophys J*, 16:1–11, 1976.

[40] E. A. Evans and R. Kalak. *Mechanics and Thermodynamics of Biomembranes*. CRC Press, Boca Raton, FL, 1980.

[41] R. S. Frank and R. M. Hochmuth. The influence of red cell mechanical properties on flow through single capillary-sized pores. *J Biomech Eng Trans ASME*, 110:155–160, 1988.

[42] T. Fujita and M. Kashimura. Scanning electron microscope studies of human spleen. *Immunol Res*, 2:375–384, 1983.

[43] Y. C. Fung. *Biomechanics: Mechanical Properties of Living Tissues.* Springer-Verlag, New York, 1993.

[44] Y. C. Fung. *Biomechanics: Circulation.* Springer, 1996.

[45] F. K. Glenister, R. L. Coppel, A. F. Cowman, N. Mohandas, and B. M. Cooke. Contribution of parasite proteins to altered mechanical properties of malaria-infected red blood cells. *Blood*, 99:1060–3, 2002.

[46] S. Handayani, D. T. Chiu, E. Tjitra, J. S. Kuo, D. Lampah, E. Kenangalem, L. Renia, G. Snounou, R. N. Price, N. M. Anstey, and B. Russell. High deformability of plasmodium vivax-infected red blood cells under microfluidic conditions. *J Infect Dis*, 199:445–50, 2009.

[47] S. Hénon, G. Lenormand, A. Richert, and F. Gallet. A new determination of the shear modulus of the human erythrocyte membrane using optical tweezers. *Biophys J*, 76:1145–1151, 2008.

[48] J. M. Higgins, D. T. Eddington, S. N. Bhatia, and L. Mahadevan. Sickle cell vasoocclusion and rescue in a microfluidic device. *Proc Natl Acad Sci USA*, 104:20496–20500, 2007.

[49] R. Hochmuth, P. Worthy, and E. Evans. Red-cell extensional recovery and the determination of membrane viscosity. *Biophys J*, 26:101–114, 1979.

[50] R. M. Hochmuth, R. N. Marple, and S. P. Sutera. Capillary blood flow. i. erythrocyte deformation in glass capillaries. *Microvasc Res*, 2:409–419, 1970.

[51] R. M. Hochmuth and R. E. Waugh. Erythrocyte membrane elasticity and viscosity. *Annu Rev Physiol*, 49:209–19, 1987.

[52] P. J. Hoogerbrugge and J. M. V. A. Koelman. Simulating microscopic hydrodynamic phenomena with dissipative particle dynamics. *Europhys Lett*, 19:155–160, 1992.

[53] J. H. Jeong, Y. Sugii, M. Minamiyama, and K. Okamoto. Measurement of rbc deformation and velocity in capillaries in vivo. *Microvasc Res*, 71:212–7, 2006.

[54] G. J. Johnson, D. W. Allen, T. P. Flynn, B. Finkel, and J. G. White. Decreased survival in vivo of diamide-incubated dog erythrocytes. a model of oxidant-induced hemolysis. *J Clin Invest*, 66:955–61, 1980.

[55] R. D. Kamm. Cellular fluid mechanics. *Annu Rev Fluid Mech*, 34:211–232, 2002.

[56] M. A. Klausner, L. J. Hirsch, P. F. Leblond, J. K. Chamberlain, M. R. Klemperer, and G. B. Segel. Contrasting splenic mechanisms in the blood clearance of red blood cells and colloidal particles. *Blood*, 46:965–76, 1975.

[57] M. Lang, C. Asbury, J. Shaevitz, and S. Block. An automated two-dimensional optical force clamp for single molecule studies. *Biophys J*, 83:491–501, 2002.

[58] J. Li, M. Dao, C. T. Lim, and S. Suresh. Spectrin-level modeling of the cytoskeleton and optical tweezers stretching of the erythrocyte. *Biophys J*, 88:3707–3719, 2005.

[59] J. Li, G. Lykotrafitis, M. Dao, and S. Suresh. Cytoskeletal dynamics of human erythrocyte. *Proc Natl Acad Sci USA*, 104:4937–42, 2007.

[60] M. J. Lighthill. Pressure-forcing of tightly fitting pellets along fluid-filled elastic tubes. *Journal of Fluid Mechanics*, 34:113–143, 1968.

[61] Lodish, Berk, P. Matsudaira, Kaiser, Scott, Zipursky, and Darnell. *Molecular Cell Biology*. 2003.

[62] M. Marinkovic, M. Diez-Silva, I. Pantic, J. J. Fredberg, S. Suresh, and J. P. Butler. Febrile temperature leads to significant stiffening of plasmodium falciparum parasitized erythrocytes. *Am J Physiol, Cell Physiol*, 296:C59–64, 2009.

[63] J. L. McWhirter, H. Noguchi, and G. Gompper. Flow-induced clustering and alignment of vesicles and red blood cells in microcapillaries. *Proc Natl Acad Sci USA*, 106:6039–6043, 2009.

[64] C. D. Meinhart, S. T. Wereley, and M. H. B. Gray. Volume illumination for two-dimensional particle image velocimetry. *Meas Sci Technol*, 11:809–814, 2000.

[65] L. H. Miller, D. I. Baruch, K. Marsh, and O. K. Doumbo. The pathogenic basis of malaria. *Nature*, 415:673–9, 2002.

[66] J. P. Mills. *Deformability of Plasmodium falciparum parasitized red blood cells*. PhD thesis, Massachusetts Institute of Technology, 2007.

[67] J. P. Mills, M. Diez-Silva, D. J. Quinn, M. Dao, M. Lang, K. S. Tan, C. T. Lim, G. Milon, P. H. David, O. Mercereau-Puijalon, S. Bonnefoy, and S. Suresh. Effect of plasmodial resa protein on deformability of human red blood cells harboring plasmodium falciparum. *Proc Natl Acad Sci USA*, 104:9213–9217, 2007.

[68] J. P. Mills, L. Qie, M. Dao, C. T. Lim, and S. Suresh. Nonlinear elastic and viscoelastic deformation of the human red blood cell with optical tweezers. *MCB*, 1:169–180, 2004.

[69] N. Mohandas, M. R. Clark, M. S. Jacobs, and S. B. Shohet. Analysis of factors regulating erythrocyte deformability. *J Clin Invest*, 66:563–573, 1980.

[70] N. Mohandas and E. Evans. Mechanical properties of the red cell membrane in relation to molecular structure and genetic defects. *Annu Rev Biophys Biomol Struct*, 23:787–818, 1994.

[71] N. Mortensen, F. Okkels, and H. Bruus. Reexamination of hagen-poiseuille flow: Shape dependence of the hydraulic resistance in microchannels. *Phys Rev E*, 71:57301–57304, 2005.

[72] K. Neuman and S. Block. Optical trapping. *Rev Sci Instrum*, 75:2787, 2004.

[73] H. Neurath, G. R. Cooper, and J. O. Erickson. The shape of protein molecules ii. viscosity and diffusion studies of native proteins. *J Biol Chem*, 138:411–436, 1941.

[74] H. Noguchi. Shape transitions of fluid vesicles and red blood cells in capillary flows. *Proc Natl Acad Sci USA*, 102:14159–14164, 2005.

[75] Y. Park, M. Diez-Silva, G. Popescu, G. Lykotrafitis, W. Choi, M. S. Feld, and S. Suresh. Refractive index maps and membrane dynamics of human red blood cells parasitized by plasmodium falciparum. *Proc Natl Acad Sci USA*, 105:13730–13735, 2008.

[76] M. Paulitschke and G. B. Nash. Membrane rigidity of red blood cells parasitized by different strains of plasmodium falciparum. *J Lab Clin Med*, 122:581–9, 1993.

[77] B. Pelz. *Single Molecule Biophysics of Actin Filament and Actin Binding Protein Machinery.* PhD thesis, University of Stuttgart, 2008.

[78] I. V. Pivkin and G. E. Karniadakis. A new method to impose no-slip boundary conditions in dissipative particle dynamics. *J Comput Phys*, 207:114–128, 2005.

[79] I. V. Pivkin and G. E. Karniadakis. Accurate coarse-grained modeling of red blood cells. *Phys Rev Lett*, 101:118105, 2008.

[80] I. V. Pivkin, P. D. Richardson, and G. Karniadakis. Blood flow velocity effects and role of activation delay time on growth and form of platelet thrombi. *Proc Natl Acad Sci USA*, 103:17164–17169, 2006.

[81] A. Popel and P. Johnson. Microcirculation and hemorheology. *Annu Rev Fluid Mech*, 37:43–69, 2005.

[82] C. Pozrikidis. Numerical simulation of blood flow through microvascular capillary networks. *Bull Math Biol*, 71:1520–1541, 2009.

[83] A. Pries. Microvascular blood viscosity in vivo and the endothelial surface layer. *Am J Physiol Heart Circ Physiol*, 289:H2657–H2664, 2005.

[84] A. R. Pries, T. W. Secomb, and P. Gaehtgens. Biophysical aspects of blood flow in the microvasculature. *Cardiovasc Res*, 32:654–67, 1996.

[85] A. R. Pries, T. W. Secomb, P. Gaehtgens, and J. F. Gross. Blood flow in microvascular networks. experiments and simulation. *Circ Res*, 67:826–34, 1990.

[86] M. Puig-De-Morales-Marinkovic, K. Turner, J. Butler, J. Fredberg, and S. Suresh. Viscoelasticity of the human red blood cell. *AJP: Cell Physiology*, 293:C597–C605, 2007.

[87] D. J. Quinn, I. Pivkin, S. Wong, K. Chiam, M. Dao, G. Karniadakis, and S. Suresh. Flow dynamics of human red blood cells in microfluidic systems. *In Preparation*, 2010.

[88] R. P. Rand and A. C. Burton. Mechanical properties of the red cell membrane. i. membrane stiffness and intracellular pressure. *Biophys J*, 4:115–35, 1964.

[89] G. Roosen and C. Imbert. Optical levitation by means of 2 horizontal laser-beams - theoretical and experimental-study. *Phys Lett A*, 59:6–8, 1976.

[90] G. W. Schmid-Schönbein. Biomechanics of microcirculatory blood perfusion. *Annu Rev Biomed Eng*, 1:73–102, 1999.

[91] T. W. Secomb and R. Hsu. Red blood cell mechanics and functional capillary density. *Int J Microcirc Clin Exp*, 15:250–254, 1995.

[92] T. W. Secomb and R. Hsu. Analysis of red blood cell motion through cylindrical micropores: effects of cell properties. *Biophys J*, 71:1095–1101, 1996.

[93] T. W. Secomb, R. Hsu, and A. R. Pries. Motion of red blood cells in a capillary with an endothelial surface layer: effect of flow velocity. *Am J Physiol Heart Circ Physiol*, 281:H629–H636, 2001.

[94] T. W. Secomb, R. Skalak, N. Ozkaya, and J. F. Gross. Flow of axisymmetric red blood cells in narrow capillaries. *J Fluid Mech*, 163:405–423, 1986.

[95] Y. Shapira, M. Vaturi, and A. Sagie. Hemolysis associated with prosthetic heart valves: a review. *Cardiol Rev*, 17:121–124, 2009.

[96] M. Sheetz. *Laser tweezers in cell biology*, volume 55 of *Methods in Cell Biology*. San Diego, 1998.

[97] J. P. Shelby, J. White, K. Ganesan, P. K. Rathod, and D. T. Chiu. A microfluidic model for single-cell capillary obstruction by plasmodium falciparum-infected erythrocytes. *Proc Natl Acad Sci USA*, 100:14618–14622, 2003.

[98] S. Shevkoplyas. Prototype of an in vitro model of the microcirculation. *Microvasc Res*, 65:132–136, 2003.

[99] S. Shevkoplyas, T. Yoshida, S. Gifford, and M. Bitensky. Direct measurement of the impact of impaired erythrocyte deformability on microvascular network perfusion in a microfluidic device. *Lab Chip*, 6:914–920, 2006.

[100] R. Skalak, N. Ozkaya, and T. C. Skalak. Biofluid mechanics. *Annual Reviews in Fluid Mechanics*, 1989.

[101] J. Sleep, D. Wilson, R. Simmons, and W. Gratzer. Elasticity of the red cell membrane and its relation to hemolytic disorders: an optical tweezers study. *Biophys J*, 77:3085–95, 1999.

[102] S. Suresh, J. Spatz, J. Mills, A. Micoulet, M. Dao, C. Lim, M. Beil, and T. Seufferlein. Connections between single-cell biomechanics and human disease states: gastrointestinal cancer and malaria. *Acta Biomater*, 1:15–30, 2005.

[103] N. Sutton, M. C. Tracey, I. D. Johnston, R. S. Greenaway, and M. W. Rampling. A novel instrument for studying the flow behaviour of erythrocytes through microchannels simulating human blood capillaries. *Microvasc Res*, 53:272–281, 1997.

[104] R. Suwanarusk, B. M. Cooke, A. M. Dondorp, K. Silamut, J. Sattabongkot, N. J. White, and R. Udomsangpetch. The deformability of red blood cells parasitized by plasmodium falciparum and p. vivax. *J Infect Dis*, 189:190–4, 2004.

[105] K. Svoboda and S. M. Block. Biological applications of optical forces. *Annu Rev Biophys Biomol Struct*, 23:247–85, 1994.

[106] X. Trepat, L. Deng, S. S. An, D. Navajas, D. J. Tschumperlin, W. T. Gerthoffer, J. P. Butler, and J. J. Fredberg. Universal physical responses to stretch in the living cell. *Nature*, 447:592, 2007.

[107] K. Tsukada. Direct measurement of erythrocyte deformability in diabetes mellitus with a transparent microchannel capillary model and high-speed video camera system. *Microvasc Res*, 61:231–239, 2001.

[108] J. Voldman, M. L. Gray, and M. A. Schmidt. Microfabrication in biology and medicine. *Annu Rev Biomed Eng*, 1:401–425, 1999.

[109] R. Waugh and E. A. Evans. Thermoelasticity of red blood cell membrane. *Biophys J*, 26:115–131, 1979.

[110] D. J. Weatherall, L. H. Miller, D. I. Baruch, K. Marsh, O. K. Doumbo, C. Casals-Pascual, and D. J. Roberts. Malaria and the red cell. *Hematology Am Soc Hematol Educ Program*, pages 35–57, 2002.

[111] D. Weibel, W. Diluzio, and G. Whitesides. Microfabrication meets microbiology. *Nat Rev Microbiol*, 5:209–218, 2007.

[112] S. Weinbaum, J. M. Tarbell, and E. R. Damiano. The structure and function of the endothelial glycocalyx layer. *Annu Rev Biomed Eng*, 9:121–167, 2007.

[113] R. Wetzel, M. Becker, J. Behlke, H. Billwitz, S. Böhm, B. Ebert, H. Hamann, J. Krumbiegel, and G. Lassmann. Temperature behaviour of human serum albumin. *Eur J Biochem*, 104:469–478, 1980.

[114] Y. Yao, A. Rabodzey, and C. F. Dewey. Glycocalyx modulates the motility and proliferative response of vascular endothelium to fluid shear stress. *Am J Physiol Heart Circ Physiol*, 293:H1023–30, 2007.

[115] B. Yap and R. Kamm. Mechanical deformation of neutrophils into narrow channels induces pseudopod projection and changes in biomechanical properties. *J Appl Physiol*, 98:1930–1939, 2005.